New approaches to the realization and identification of Majorana qubits in solid state quantum devices

Inaugural-Dissertation

zur

Erlangung des Doktorgrades

der Mathematisch-Naturwissenschaftlichen Fakultät

der Universität zu Köln

vorgelegt von

Jan Manousakis

aus Köln

Köln 2020

Berichterstatter:

Prof. Dr. Alexander Altland

Prof. Dr. Simon Trebst

Tag der letzten mündlichen Prüfung: 29.05.2020

Abbreviations

The following abbreviations will be used throughout this dissertation:

TI:	Topological insulator
TSC:	Topological superconductor
SC:	Superconductor
MBS:	Majorana bound state
MZM:	Majorana zero-mode
PHS:	Particle hole symmetry
ABS:	Andreev bound state
FCS:	Full counting statistics
BdG:	Bogoliubov-de Gennes
BCS:	Bardeen-Cooper-Schrieffer
1D:	one-dimensional
ZBCP:	zero-bias conductance peak
SM:	Semiconductor

Abstract

Majorana bound states in topological superconductors exhibit exotic non-Abelian braiding statistics and hold promise for particularly robust qubits with natural built-in mechanisms against decoherence. The theme of this dissertation is the theory of novel approaches to realization and identification of such Majorana qubits.

Towards the realization of Majorana qubits, we present architectures based on topological insulator nanoribbons, e.g. made of $\mathrm{Bi_2Se_3}$, and proximitized by an s-wave superconductor. Piercing of proximitized nanoribbons with an axial uniform magnetic flux of suitably adjusted strength has been previously predicted to give rise to one-dimensional topological superconductors with robust Majorana bound states. We propose qubit designs that incorporate two such topological superconductors connected by a constricted topological nanoribbon segment. This constriction is non-proximitized and its lesser cross section results in a local gap opening. We present theoretical results showing the possibility to conveniently tune the coupling of a pair of Majorana states localized across the constriction via gating. Moreover, we discuss proof-of-principle experiments for initialization, manipulation, and readout of the floating version of the device, which is dominated by charging effects. We compare the platform to other Majorana qubit proposals and give an outlook on applications such as the Majorana surface code.

The experimental identification of Majorana bound states represents one of the outstanding goals of contemporary condensed matter physics. Towards identification, we present the theory of novel transport spectroscopic approaches geared to qubits in the Coulomb blockade regime. In particular, we propose a scheme in which three normal-conducting leads are weakly coupled to three different Majorana bound states of the qubit. The protocol relies on the simultaneous continuous weak measurement of two noncommuting, nonlocal Pauli operators of the Majorana qubit and results in a phenomenon of surprisingly strong current cross-correlations. This is the prime signature containing information that enables to identify the nonlocal Pauli algebra, which is intimately related to the celebrated non-Abelian braiding statistics. The latter is a property notoriously hard to demonstrate and of large attractiveness from the fundamental as well as applied perspective. The conditions under which the pronounced current cross-correlations are observable depend on the device configuration, a fact that leads to several experimentally verifiable predictions that allow to test the authenticity of the Majorana qubit. Beyond that, we put forward two further detection methods in this thesis. First, a shot noise scheme which is viable for a single floating topological Majorana wire. Second, a protocol relying on projective current measurements. Beyond the usefulness of these protocols, we identify the aforementioned protocol of monitoring a nonlocal Pauli algebra as the scheme accessing the most information related to the constitutive nature of Majorana bound states.

Zusammenfassung

Gebundene Majorana-Zustände in topologischen Supraleitern weisen exotische nicht-abelsche Statistik auf und versprechen besonders robuste Qubit-Realisierungen mit Schutzmechanismen gegen Dekohärenz. Das Thema der vorliegenden Dissertation ist die Theorie neuer Methoden zur Realisierung und Identifizierung solcher Majorana-Qubits.

Im Hinblick auf die Realisierung von Majorana-Qubits stellen wir Designarchitekturen vor, die auf topologischen Isolator-Nanodrähten beruhen. Letztere können etwa aus dem Material Bi_2Se_3 bestehen. Vorangegangene Arbeiten haben derartige Nanodrähte in Proximität zu s-Wellen-Supraleitern untersucht und vorhergesagt, dass ein gleichmäßiger axialer magnetischer Fluss von der Stärke eines halben Flussquantums einen eindimensionalen topologischen Supraleiter mit gebundenen Majorana-Zuständen entstehen lässt. In unseren Qubit-Designentwürfen werden zwei solche topologische Supraleiter durch einen verengten Abschnitt aus topologischem Nanodraht verbunden. Der geringe Querschnitt dieser Verengung führt lokal zu einer Energielücke. Wir präsentieren theoretische Resultate, die die Möglichkeit einer bequem manipulierbaren Kopplung der Majorana-Zustände demonstrieren. Des Weiteren diskutieren wir Proof of Principle Experimente zur Initialisierung, Manipulation und Auslesung unserer Qubit-Platform unter Bedingungen der Coulomb-Blockade. Wir vergleichen die Plattform mit anderen Ansätzen der Majorana-Qubit Realisierung und geben einen Ausblick auf weitergehende Anwendungen wie etwa den Majorana-Oberflächencode.

Die experimentelle Identifizierung von Majorana-Zuständen gehört zu den herausragenden Zielen der gegenwärtigen Festkörperphysik. Zu diesem Zweck stellen wir neuartige transportspektroskopische Methoden vor, die auf Majorana-Qubits unter Bedingungen der Coulomb-Blockade ausgelegt sind. Es ist Teil der Methode, dass drei normalleitende Elektroden schwach an drei verschiedene Majorana-Zustände des Qubits gekoppelt werden. Das Protokoll stützt sich auf die simultane kontinuierliche schwache Messung zweier nicht-kommutierender, nicht-lokaler Pauli-Operatoren des Majorana-Qubits und führt zu einem Phänomen überraschend starker Strom-Kreuzkorrelationen. Diese experimentell messbare Größe enthält Informationen, die es ermöglichen, die nicht-lokale Pauli-Algebra zu identifizieren, welche eng mit der nichtabelschen Statistik verwandt ist. Die nichtabelsche Statistik ist eine Eigenschaft, die berüchtigt dafür ist, dass sie schwer nachzuweisen ist, und sowohl aus fundamentaler als auch aus angewandter Perspektive eine große Attraktivität besitzt. Die Bedingungen, unter denen die ausgeprägten Kreuzkorrelationen vorherrschen, hängen von der Gerätekonfiguration ab; eine Tatsache, die zu mehreren experimentell nachprüfbaren Vorhersagen führt. Diese Vorhersagen erlauben es, die Authentizität des Majorana-Qubits zu testen. Darüber hinaus schlagen wir in dieser Arbeit zwei weitere Methoden vor, um Majorana-Zustände zu detektieren. Erstens Schrotrausch-Messungen an einem nicht geerdeten, topologischen Majoranadraht und zweitens ein Protokoll, das sich auf projektive Strommessungen stützt. Über die Nützlichkeit dieser beiden Protokolle hinaus macht das oben beschriebene Monitoring einer nicht-lokalen Pauli-Algebra mehr Information über die Natur der Majorana-Zustände zugänglich.

Contents

Chapter 1

Introduction

In 1928, Paul Dirac published the relativistic quantum wave equation [1], which in his honor is known as the Dirac equation and constitutes one of the pillars of our modern scientific world view. This fundamental contribution enabled a unified view of quantum mechanics and the special theory of relativity, laid the groundwork of quantum field theory, and inspired Dirac himself to make an important prediction about nature − the existence of antimatter. Ettore Majorana made a landmark contribution in 1937 proving the existence of a representation of the Dirac equation with a purely real wave function, $\Psi = \Psi^*$, thus, postulating a neutral fermionic excitation [2]. Ever since, the notion of a neutral fermion being its own antiparticle became reputable from the vantage point of established theoretical physics. Whether nature chooses implementation of this scenario in the form of an elementary particle is still experimentally undecided with the neutrino being the most prominent suspect [3].

Interestingly, the time-dependent quantum fields $\Psi(\boldsymbol{r}, t)$ describing Bogoliubov quasiparticles in superconductors within the framework of the well established Bardeen-Cooper-Schrieffer (BCS) theory share the mathematical properties of the neutral fermions studied by Majorana [3]. This becomes less surprising when we recall that these quasiparticles constitute superpositions of electrons and electron holes, which play a role analogous to that of matter and antimatter particles in the discussion above. This thesis is centered around the closely related concept of the Majorana zero-mode (MZM) [4], which is the cause for great activity and interest in the field of condensed matter physics. The particle hole symmetry (PHS) of the superconductor is described by an anti-unitary operator P which satisfies $\mathit{\Phi}_{-E}(\boldsymbol{r}) = P\mathit{\Phi}_E(\boldsymbol{r})$ when we express the quasiparticle as $\Psi(\boldsymbol{r},t) = e^{-iEt}\mathit{\Phi}_E(\boldsymbol{r})$. Hence, the PHS dictates that the spectrum exhibits symmetry around zero energy. A MZM $\mathit{\Phi}_0(\boldsymbol{r}) = P\mathit{\Phi}_0(\boldsymbol{r})$ in the presence of a finite energy gap Δ and remote from other MZMs is therefore protected by symmetry: it cannot move away from zero energy. This protection is very robust and a consequence of non-trivial topology of the bulk of the special host systems, which are known as topological superconductors (TSCs) [5]. A paradigmatic example of TSCs is the Kitaev model [6]. The second quantized operator creating a MZM localized at the domain walls or vortices of TCSs is identical to the operator annihilating it, i.e. $\gamma^\dagger = \gamma$. Disappointingly, topological insulators are rarely occurring in nature [4], but inventive ideas to engineer them by forming heterostructures have been put forward. This approach was initialized by an innovative proposal of Fu and Kane [7]. The latter led to prominent proposals involving proximitized semiconducting nanowires with spin-orbit coupling [8, 9] making the above mentioned Kitaev model experimentally accessible. We emphasize that, in contrast to the neutral fermions studied by Majorana in 1937, MZMs in TSCs come into existence as an emergent phenomenon caused by the constituent electrons of the material. The most noteworthy difference, however, is that MZMs bound to defects adhere to a special kind of statistics known by the scholars of theoretical physics as non-Abelian anyonic. The exchange of identical non-Abelian anyons is radically different from that of identical fermions or bosons – it can result in a different quantum state at the same energy which may pave the way to topological quantum computation [10]. Hence, such exotic properties are not only intriguing from the point of view of fundamental physics, but also because of the prospect of technological advances in quantum information processing hardware.

1.1 This thesis and its structure

The theme of this dissertation is the theory of novel approaches to realize and detect Majorana qubits, which have been envisioned and deemed attractive due to their topological protection as the building blocks of quantum information processing implementations. This is founded on the hope that at low energies Majorana qubits may provide for natural built-in mechanisms against detrimental decoherence and decay [10, 11, 12]. Towards realization of such systems, we propose device designs of Majorana qubits relying on previously proposed MBS platforms based on topological insulator (TI) nanowires proximitized by an s-wave superconductor (SC) in the presence of a longitudinally aligned magnetic field [13, 14]. Towards detection, we note that platforms that are predicted to contain unpaired MBSs are studied in several laboratories around the world, including but not limited to superconductor–semiconductor heterostructures in Copenhagen and Delft [15]. This in itself is a testament to the intense efforts in the condensed matter community in recent years. Although a wealth of accumulated measured data consistent with MBS predictions exists, the unambiguous demonstration of topological MBSs has proven to be difficult as we will discuss in more detail in Section 2.4. The three main aspects which have to be investigated to demonstrate MBSs are broadly speaking the following: (a) verification of non-Abelian braiding properties, (b) corroboration that two MBSs constitute a vastly nonlocal Dirac fermion, and (c) demonstration of localized Majorana bound states in TSCs. Property (a) is the ultimate goal but also the most demanding. In this thesis, we provide theoretical blueprints for a next generation of experiments to detect the Majorana qubit which can as well be understood as detecting the sought-after unpaired MBS itself. First, we are guided by the requirement that the protocols should substantiate aspects (a) and (b) by going beyond local probes. Second, reliance on presently available hardware is important for experiments that can be implemented realistically in the short term to avoid stalling of progress in the field. We make the argument that a good balance of information gain and experimental feasibility is found in transport spectroscopy where we propose protocols that lie within the scope of present day experimental physics. The protocols aim at the core property of the Majorana qubit, its nonlocal Pauli algebra, by accessing information closely related to the celebrated non-Abelian braiding statistics.

The thesis is organized in six chapters:

- Chapter 2: In this chapter, we review several aspects of the physics of MBSs in solid state quantum devices aiming to make this thesis self-contained. We briefly explain the broader context of topological matter and discuss the quest for MBSs in 1D condensed matter systems. We go on to discuss Majorana box qubits and their associated nonlocal Pauli algebra as well as the celebrated non-Abelian braiding statistics. Finally, we discuss the state of the presently accumulated evidence for MBSs as well as existing proposals for a next generation of experiments.

- Chapter 3: In this chapter, we propose new architectures for the realization of Majorana qubits based on platforms of topological insulator (TI) nanowires in proximity to s-wave superconductors (SCs). We show quantitatively that the coupling of the robust MBSs in these architectures is conveniently manipulable. We then go on to discuss proof-of-principle experiments and applications for the proposed platforms. Moreover, we analyze design advantages and drawbacks in comparison to other approaches to Majorana qubit realization.

- Chapter 4: This chapter is central to the thesis and details novel detection protocols for MBSs. The protocols are based on simultaneous weak measurement of the nonlocal Pauli operators of the Majorana qubit. We discuss in great detail a predicted strong effect of current cross-correlations, which allows the identification of genuine Majorana qubits. The protocols yield information similar to that of a full braiding protocol.
- Chapter 5: In this chapter, we discuss two further new variants of MBS detection protocols. The discussion at the end of the chapter reveals that the aforementioned protocol presented in Chapter 4 accesses the most information related to the fundamental nature of MBSs.
- Chapter 6: In the last chapter, we provide an overall conclusion and outlook.

Chapter 2

Majorana bound states in solid state quantum devices

2.1 Topological Majorana nanowires

The field of topological insulators (TIs) and topological superconductors (TSCs) is one of the most vibrant and active fields in contemporary condensed matter physics [16, 17]. In this section, we put 1D Majorana wires in the context of topological matter, discuss an important model of 1D p-wave superconductivity and subsequently discuss its implementation. For further reading, we note that numerous informative review articles are available [3, 4, 5, 18, 19, 20].

2.1.1 Majorana wires in the framework of topological matter

Topological Majorana wires are quasi one-dimensional superconducting representatives of a celebrated form of matter known as symmetry-protected topological matter, which provides a theoretically unified view on topological insulators (TIs) and topological superconductors (TSCs) [21]. Conceptually, topological matter is founded on the topological classification of noninteracting gapped fermionic Hamiltonians based on their symmetry. According to a fundamental result of Altland and Zirnbauer, there are generically precisely ten symmetry classes that the system can belong to [22]. This result is also known as the "tenfold way" for disordered fermions. In the presence of a gap, these free fermion systems are topologically classified in the "periodic table for topological insulators and superconductors" [23]. An excerpt of this table is shown in Table 2.1. For given spatial dimension and symmetry class, the table predicts whether a topological material with bulk invariant either of $\mathbb{Z}$ or $\mathbb{Z}_2$ type is possible or not. Every TI or TSC generically features gapless surface states that are robust against perturbations which are not gap closing.

AZ Class	**TRS**	**PHS**	**1D**	**2D**	**3D**
BDI	$+1$	$+1$	$\mathbb{Z}$	0	0
D	-	$+1$	$\mathbb{Z}_2$	$\mathbb{Z}$	0
DIII	-1	$+1$	$\mathbb{Z}_2$	$\mathbb{Z}_2$	$\mathbb{Z}$

Table 2.1: Excerpt of the "periodic table for topological insulators and superconductors" [21, 23] showing TSCs in up to three dimensions with PHS squaring to the identity. The entry "0" for a given Altland-Zirnbauer (AZ) symmetry class and dimension implies that every ground state is a member of the same phase, which is topologically trivial.

Based on the discussion so far, one might wonder how superconductivity fits into a scheme of noninteracting fermions. After all, superconductivity is rooted in attractive phonon mediated quantum interactions of electrons near the Fermi surface. This can be understood by recalling that within a standard mean field approximation a SC is described as a noninteracting system of fermionic Bogoliubov quasiparticles which is gapped due to the superconducting order parameter [5]. The BCS mean field Hamiltonian (up to a constant) is given by [24]

$$H_{BCS} = \sum_{\sigma,\boldsymbol{k}} \xi_{\boldsymbol{k}} c^\dagger_{\boldsymbol{k}\sigma} c_{\boldsymbol{k}\sigma} + \sum_{\boldsymbol{k}} \left[\Delta_{\boldsymbol{k}} c^\dagger_{\boldsymbol{k}\uparrow} c^\dagger_{-\boldsymbol{k}\downarrow} + \Delta^*_{\boldsymbol{k}} c_{-\boldsymbol{k}\downarrow} c_{\boldsymbol{k}\uparrow} \right], \tag{2.1}$$

where $\Delta_{\boldsymbol{k}}$ is the superconducting order parameter and $c_{\boldsymbol{k}\sigma}$ creates an electron with spin σ, momentum $\boldsymbol{k}$ and dispersion $\xi_{\boldsymbol{k}} = \frac{\hbar^2 \boldsymbol{k}^2}{2m} - \mu$. Introducing the spinor $\Psi^\dagger_{\boldsymbol{k}} = (c^\dagger_{\boldsymbol{k}\uparrow}, c^\dagger_{\boldsymbol{k}\downarrow}, c_{-\boldsymbol{k}\uparrow}, c_{-\boldsymbol{k}\downarrow})$, we can write the Hamiltonian in the first quantized form up to a constant as

$$H_{BCS} = \frac{1}{2} \sum_{\boldsymbol{k}} \Psi^\dagger_{\boldsymbol{k}} \mathcal{H}_{BdG}(\boldsymbol{k}) \Psi_{\boldsymbol{k}}, \tag{2.2}$$

which is well known as the Bogoliubov-de Gennes (BdG) Hamiltonian [24]. The antiunitary particle hole symmetry $\mathcal{P} = U_P K$, with U_P a unitary operator and K the complex conjugation operation, is a generic feature of superconducting BdG Hamiltonians [5],

$$U_P \mathcal{H}^*_{BdG}(\boldsymbol{k}) U_P^{-1} = -\mathcal{H}_{BdG}(-\boldsymbol{k}). \tag{2.3}$$

In the absence of time-reversal symmetry and for $\mathcal{P}^2 = 1$, a SC is placed in the Altland-Zirnbauer symmetry class D. In spatial dimension $d = 1$ there exists a $\mathbb{Z}_2$ topological invariant (see Table 2.1) also referred to as the "Majorana number" $\mathcal{M} = \pm 1$ [6]. The principle of bulk-boundary correspondence states that nontrivial bulk topology, $\mathcal{M} = -1$, manifests itself holographically in protected states on the surface. The "surface" of a finite wire is defined by the two end points, and the protected surface states are the Majorana bound states γ_α which this thesis is focused on. Creation and annihilation are achieved with the same operator $\gamma_\alpha^\dagger = \gamma_\alpha$, the Majorana operators obey the Clifford algebra [20]

$$\gamma_\alpha \gamma_{\alpha'} + \gamma_{\alpha'} \gamma_\alpha = 2\delta_{\alpha\alpha'}. \tag{2.4}$$

Furthermore, γ_α squares to the identity, i.e. $\gamma_\alpha^2 = 1$.

2.1.2 Kitaev's p-wave superconducting lattice model

Kitaev's paradigmatic chain model [6] is discussed in great detail in many excellent reviews, e.g. Refs. [3, 4, 19, 20]. Hence, we discuss it here only briefly. The one-dimensional lattice contains N sites and a spinless fermion is created on the site i by the operator $c_i^\dagger$. The Hamiltonian of the 1D SC reads

$$H = \sum_{i=1}^{N-1} \left[-\mu c_i^\dagger c_i - t \left(c_i^\dagger c_{i+1} + c_{i+1}^\dagger c_i \right) + \Delta \left(c_i^\dagger c_{i+1}^\dagger + c_{i+1} c_i \right) \right], \tag{2.5}$$

and includes an onsite chemical potential μ as well as a nearest neighbor hopping term with amplitude t. The pairing is of p-wave type coupling nearest neighbors with amplitude Δ. Furthermore, we assume that a global phase rotation has been performed to achieve $\Delta \in \mathbb{R}$. How can we see that this model is indeed an example of a 1D topological superconductor? To this end, it is instructive to consider the special point

$t = \Delta$ and $\mu = 0$ in parameter space, where the Hamiltonian takes on the form

$$\begin{aligned} H(t=\Delta, \mu=0) &= \sum_{i=1}^{N-1} \left[-\Delta \left(c_i^\dagger c_{i+1} + c_{i+1}^\dagger c_i \right) + \Delta \left(c_i^\dagger c_{i+1}^\dagger + c_{i+1} c_i \right) \right] \\ &= \sum_{i=1}^{N-1} \Delta \left(c_i^\dagger + c_i \right) \left(c_{i+1}^\dagger - c_{i+1} \right). \end{aligned} \tag{2.6}$$

We take note that two Majorana operators represent the Hermitian and anti-Hermitian part of a conventional Dirac fermion c_i since we may define them as $\gamma_i = c_i^\dagger + c_i$ and $\tilde{\gamma}_i = i(c_i^\dagger - c_i)$. The Hamiltonian then takes on the form

$$H(t=\Delta, \mu=0) = -i\Delta \sum_{i=1}^{N-1} \gamma_i \tilde{\gamma}_{i+1}. \tag{2.7}$$

This means that two of the Majorana operators represent zero-modes, i.e. $[H, \tilde{\gamma}_1] = [H, \gamma_N] = 0$, that are PHS protected and locked in at zero energy. Thus, the Majoranas $\tilde{\gamma}_1$ and γ_N are unpaired and can be arbitrarily far apart depending on the wire length. We can define a highly nonlocal Dirac fermion created by

$$f^\dagger = \frac{1}{2}(\tilde{\gamma}_1 - i\gamma_N) \tag{2.8}$$

which can be occupied at vanishing energy cost. The ground state of topologically trivial SCs is unique and accommodates all electrons in the form of Cooper pairs. The presence of the fermion (2.8) changes this picture: consider that $|0\rangle$ with $f\,|0\rangle = 0$ is a ground state. Then, we have a two-fold degenerate ground state because $|1\rangle \equiv f^\dagger\,|0\rangle$ is another ground state with different fermion parity. The Majorana number for the simple model can then be derived [6] to be

$$\mathcal{M} = \operatorname{sign}\left(\mu^2 - 4t^2\right). \tag{2.9}$$

A nontrivial TSC configuration (μ, t, Δ) in parameter space is characterized by a finite gap and $\mathcal{M} = -1$. All nontrivial TSC configurations, of which the special point $(t = \Delta, \mu = 0)$ is merely an example, can be smoothly deformed into each other without closing the gap (as long as PHS is preserved). For general parameters in the topological phase, a MBS γ_1 localized at one wire end satisfies $[H, \gamma_1] \sim \exp(-L/\xi)$, with ξ the parameter dependent size of the MBS and L the length of the wire [4]. It follows that

γ_1 becomes an exact zero-mode in the limit $L \to \infty$ of an infinite wire. The associated topological phase is signified by weak pairing. In order to reach a topologically trivial configuration by smooth deformation of the Hamiltonian, then requires necessarily to close and reopen the gap and to undergo a topological phase transition.

2.1.3 Physical realization of 1D p-wave SC

The lesson learned in the previous subsection can be summarized as follows: in order to realize the Kitaev chain model an effectively spinless SC with p-wave pairing is required. Unfortunately, intrinsic p-wave SCs are exceedingly scarce in nature [4]. However, Fu and Kane came up with the idea to synthetically engineer TSCs by putting TIs and s-wave SCs in proximity [7]. This important contribution led to many further proposals, two of which are particularly important in this thesis. One of them proposes to proximitize TI nanowires to give rise to 1D TSCs [13, 14], which we will review and apply to realize qubits in Chapter 3.

Another particularly promising approach involves spin-orbit coupled semiconductor (SM) nanowires [8, 9], which we are going to discuss in the remainder of this subsection. In the presence of a strong magnetic field, such systems can be tuned to a regime where only one longitudinal band is important and the system is effectively spinless. In proximity to an s-wave superconductor, the spin polarized electrons are endowed with a pairing term allowing them to be driven into the topological phase. The experimental activity based on these proposals led to the probably most advanced Majorana platform [15]. The noteworthiness of this approach stems for the fact that it provides a way to accomplish a Majorana wire in realistic systems with the help of well studied components such as semiconductors and s-wave SCs. The Hamiltonian describing such systems is given by [4, 15]

$$\begin{aligned} H &= H_{\mathrm{SM}} + H_{\mathrm{SC}}, && (2.10) \\ H_{\mathrm{SM}} &= \sum_{\sigma,\sigma'} \int_0^L dx \psi_\sigma^\dagger(x) \left(-\frac{\hbar^2}{2m}\partial_x^2 - \mu + i\hbar\alpha_R \sigma_2 \partial_x + \mathit{\Gamma}\sigma_1 \right)_{\sigma\sigma'} \psi_{\sigma'}(x), && (2.11) \\ H_{\mathrm{SC}} &= \int_0^L dx \left(\Delta \psi_\uparrow(x) \psi_\downarrow(x) + \mathrm{H.c.} \right). && (2.12) \end{aligned}$$

Here $\mathit{\Gamma} = g\mu_B B$ is the external magnetic field with g the effective Landé g-factor, B the applied magnetic field and μ_B the Bohr magneton. Furthermore, μ is the chemical potential, m the effective mass and α_R the Rashba spin-orbit coupling constant. The field operator $\psi_\sigma^\dagger(x)$ creates an electron at position x with spin σ. We assume that the magnetic field and the spin-orbit field are oriented orthogonally to each other. In that case, the energy eigenvalues for momentum k and $\Delta = 0$ are given by [4]

$$E_k = \frac{\hbar^2 k^2}{2m} - \mu \pm \sqrt{\Gamma^2 + \alpha_R^2 k^2} \tag{2.13}$$

as shown in Fig. 2.1. If the chemical potential μ is located within the gap opened by Γ, the fermions are effectively spin-polarized. Proximity coupling of a s-wave SC to the SM endows the effectively spinless fermions with Cooper pairing. For Zeemann field $\mathit{\Gamma} > \Gamma_c$ with

$$\Gamma_c = \sqrt{|\Delta|^2 + \mu^2}, \tag{2.14}$$

the Refs. [8, 9] have ingeniously predicted that the system is in a topological superconducting phase. The experimental implementation of this approach will be discussed in more detail in Section 2.4.

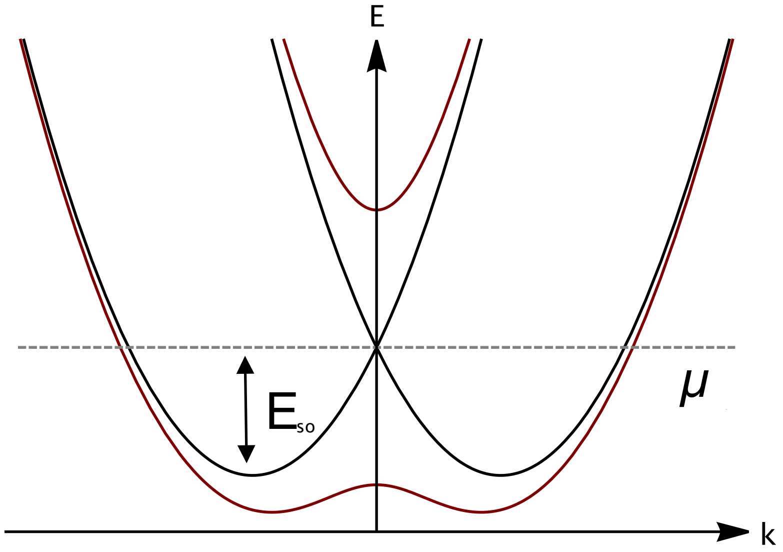

Figure 2.1: Schematic form of the energy spectrum as a function of momentum k of a SM wire in the presence (black) and absence (red) of a TRS-breaking Zeemann field, respectively. The spin-orbit-coupling is characterized by the energy scale $E_{so} = \frac{m}{2}\alpha_R^2$ [4, 15]. For suitable chemical potential values μ, the system displays effective spinlessness.

2.2 Topological Majorana qubits

The Majorana qubit in the most elementary incarnation can be conceptualized as a topological superconductor of mesoscopic size hosting four MBSs $\gamma_0, \ldots, \gamma_3$ [25, 26]. Two MBSs are not sufficient for a useful qubit since the quantum information would be stored in the parity of a single fermionic mode and could be read out by the Coulomb interaction, which is long ranged. Two nonlocal fermionic modes on the other hand enable to perform parity-protected quantum computation.

Now, we would like to think about the mesoscopic SC island or “box” as being not grounded – a situation that we will also refer to as “floating”. The N island electrons affect each other by means of the Coulomb interaction giving rise to an energy $H_C = E_C N^2$. The effective interaction strength is set by the charging energy $E_C = 2e^2/C$ with C the linear capacitance of the device regions in good electrical contact with each other. A capacitively coupled gate can regulate the electrostatic potential locally on the island. This modifies the ground state energy according to $H_C = E_C N^2 + eNV$ [27]. Up to a constant and with $\hat{N}$ the electron number operator we obtain the Hamiltonian

$$H_C = E_C(\hat{N} - n_g)^2, \tag{2.15}$$

with the dimensionless back-gate parameter $n_g = eV/2E_C$ controlling the energetically ideal island charge. This charging Hamiltonain has been used in the context of topological systems e.g. in Refs. [25, 26, 28, 29]. We point out that due to the MBSs an odd number of electrons can also be accommodated. Under Coulomb valley conditions, or more generally far away from the charge degeneracy point $n_g = 1/2$, the fermion parity is fixed [25],

$$\gamma_0\gamma_1\gamma_2\gamma_3 = \pm 1. \tag{2.16}$$

The charging physics provides a mechanism alleviating the harm caused by quasiparticle poisoning events from outside the island in the regime of low energy [29, 30], because it assigns an energy cost to these detrimental processes. The QP poisoning time has been studied in the SM devices and was found to be of order $\gtrsim 1\mu$s [31]. According to Eq. (2.16), the degeneracy of the ground state is broken down from four-fold to two-fold, which we identify with our Hilbert space. The topologically protected Majorana qubit operating in this Hilbert space is characterized by a nonlocal Pauli algebra [25]

$$\sigma_1 = i\gamma_1\gamma_0, \quad \sigma_2 = i\gamma_2\gamma_0, \quad \sigma_3 = i\gamma_2\gamma_1. \tag{2.17}$$

These Pauli operators are "fractionalized" into Majorana bilinear operators.

A practical implementation scheme is based on two one-dimensional (1D) proximitized nanowires which are driven in the topological phase by an applied magnetic field with MBSs at their terminations [11, 12]. Parallely aligned, the wires are joined with the help of a conventional s-wave superconducting bridge, see Fig. 2.2. Here, we assume the charging energy of each wire to be small compared to the Josephson coupling so that the composite object forms a single island with a single charging energy typically of the order of 1meV [15].

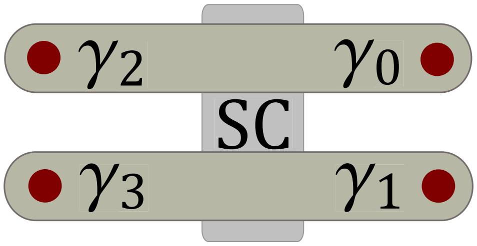

Figure 2.2: The "Majorana box qubit" or "tetron" [11, 12] is made from two one-dimensional, proximitized nanowires (gray-green) hosting MBSs γ_α at their ends. The linear dimension of the two wires is assumed to vastly exceed the superconducting coherence length ξ so that the MBSs effectively represent zero-modes. A trivial s-wave SC (gray) connects the wires to form a superconducting "Cooper pair box" that is effectively characterized by a single charging energy E_C.

The geometry displayed in Fig. 2.2 has been referred to in the literature as "tetron" [12] or "Majorana box qubit" [11]. Closely related and also important in the context of this thesis is the "hexon" [12] structure with six MBSs, which is analogously constructed from three parallel 1D TSCs forming a single island.

In Chapter 3 of this thesis we describe another Majorana box qubit construction based on topological insulator nanowires which are coated with a superconductor.

2.2.1 Majorana qubit interferometric readout

The step of readout and initialization of quantum information encoded in the Majorana qubit is indispensable for its functionality. Extracting the occupation from a pair of completely decoupled MZMs is not possible [6]. Therefore, one requires a tunable coupling term that can be strongly suppressed to protect the information and turned on during the readout phase enabling an observable to couple to it. There are multiple different approaches to reading out Majorana qubits, e.g. involving the inductive coupling to a flux qubit [30, 32]. Another approach requires to couple the Majorana qubit capacitively to quantum dots [11, 12].

Now, we review another approach founded on Majorana interferometry, where the observable is the electrical conductance, see Ref. [11]. The approach relies on a striking nonlocal transport phenomenon, which forms the basis for the weak measurement protocols that we will discuss in Chapter 4. The Majorana qubit is strongly Coulomb blockaded, and tunable tunneling barriers connect two electrodes with two different spatially separated MBSs. The strong charging effects hinder the electrons from tunneling onto the SC island. However, quantum charge fluctuations permit cotunneling through the island [33]. At energy scales small compared to E_C and the superconducting gap Δ, the box qubit device is equivalent to two fermionic levels with support at the four ends of the two TSC wires. The nonlocal transport through the box from lead α to lead α' due to Coulomb charging is described by the Hamiltonain [29, 30]

$$H = t_1(i\gamma_\alpha \gamma_{\alpha'})c^\dagger_{\alpha,k} c_{\alpha',k'} + \text{H.c.}, \tag{2.18}$$

with the fermionic creation operators $c^\dagger_{\alpha,k}$ for lead α and momentum k. The phase and absolute value of the transmission amplitude t_1 is independent of the tunneling distance – a fact that Fu has labeled as "teleportation" of electrons [29]. We will refer to the transport as phase coherent and note that there is experimental evidence consistent with such a long distance phenomenon [34]. The foundation of various interferometric schemes is the observation that a flip of the parity $i\gamma^i_\alpha \gamma^j_{\alpha'}$ causes a π phase shift in the transmission amplitude. This mechanism allows to obtain a parity dependent conductance (current) by devising a second path for the electrons to tunnel through, see Fig. 2.3. This interference path serves as a reference and may be realized using a low density SM or a second Majorana island with fixed parity [11]. The interferometric purpose of the link dictates that its length should be short enough to enable phase coherent

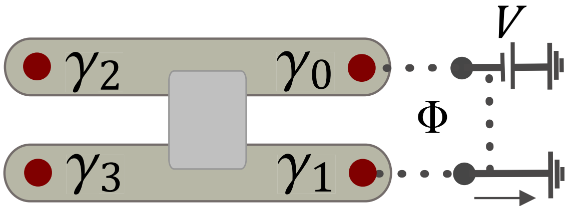

Figure 2.3: Electron interferometric scheme for Majorana qubit [11, 12, 30] readout of the occupancy of the nonlocal Dirac fermion $(\gamma_0 + i\gamma_1)/2$ by measuring the tunneling conductance $G = dI/dV$. The first path goes through the Coulomb blockaded Majorana qubit, while the second path is a tunneling link, e.g. realized by a low-density semiconductor with a sufficient phase-coherence length (vertical dashed line). Furthermore, there is an external magnetic flux Φ present which is enclosed by the two paths.

electron transport. When we further assume that there is a magnetic flux Φ piercing in between the two paths, the conductance depends on the parity according to [11, 30]

$$G(\Phi) = g_0 + i\gamma_0\gamma_1 g(\Phi), \tag{2.19}$$

with $g(\Phi) = g(\Phi + h/e)$, i.e. exhibiting Aharonov-Bohm oscillations. We emphasize that without the interference path, the conductance is not parity dependent. The conductance measurement hence amounts to a projective readout of the parity $i\gamma_0\gamma_1$.

2.3 The non-Abelian nature of Majorana zero-modes

We will now discuss the physical meaning of the non-Abelian properties of MZMs [10], highlighting the connection to the nonlocal Pauli algebra of a Majorana qubit, which will be of crucial importance in Chapter 4.

2.3.1 Non-Abelian braiding statistics

It was first shown by Ivanov in 2001 that MZMs bound to vortices in 2D p-wave Superconductors behave as non-Abelian anyons when the vortices are exchanged [35]. It has been put forward that 1D TSCs can in principle be used in branched Y- or T-geometries by manipulating the MBS carrying domain walls [36, 37]. To understand the term anyon, we recall that in three dimensions, quantum particles are either bosons or fermions. In two dimensions, a quantum particle can be neither a fermion nor a boson but a third option called anyon [10]. Under the exchange of identical particles α and β, the wavefunction can pick up a general phase factor, i.e. $|\ldots,\psi_\alpha,\ldots,\psi_\beta,\ldots\rangle = \exp(i\theta)\,|\ldots,\psi_\beta,\ldots,\psi_\alpha,\ldots\rangle$. For real statistical angle $\theta \notin \{0,\pi\}$, such particles are called Abelian anyons [10]. If the many body ground state has multiple degeneracies, the exchange of identical particles can even cause a change of the quantum state, a scenario which is known as non-Abelian statistics. This term is motivated by the fact that the phase factor $\exp(i\theta)$ is replaced by a unitary operator $T_{\alpha\beta}$ in the space spanned by the degenerate ground states [10],

$$|\ldots,\psi_\alpha,\ldots,\psi_\beta,\ldots\rangle = T_{\alpha\beta}\,|\ldots,\psi_\beta,\ldots,\psi_\alpha,\ldots\rangle\,. \tag{2.20}$$

In general, unitary operators are noncommutative, implying that the final quantum state can depend on the order in which the indistinguishable particles have been exchanged. MZMs bound to defects represent a special type of non-Abelian anyon known as Ising anyon and we now discuss how braiding implements a unitary evolution in the degenerate ground state manifold. Drawing on our discussion of Majorana based qubits, we again consider four MZMs $\gamma_0,\ldots,\gamma_3$ and we may think of the associated Hilbert space as our computational space. For a start, we determine the form of the unitary operator corresponding to the adiabatic exchange of two of the Majoranas in counter-clockwise direction following the heuristic discussion given in Ref. [38]. Denoting this transformation $\gamma_0 \to \tilde{\gamma}_0 = T_{01}^\dagger \gamma_0 T_{01}$ and $\gamma_1 \to \tilde{\gamma}_1 = T_{01}^\dagger \gamma_1 T_{01}$, we conclude $\tilde{\gamma}_1 = \lambda_0 \gamma_0$ and $\tilde{\gamma}_0 = \lambda_1 \gamma_1$ from the fact that the Majoranas are simply swapped. The new operators $\tilde{\gamma}_\alpha$ are evidently required to obey $\tilde{\gamma}_\alpha^\dagger = \tilde{\gamma}_\alpha$ and $\tilde{\gamma}_\alpha^2 = 1$, which implies $\lambda_\alpha = \pm 1$. Since the adiabatic exchange cannot result in a change of the parity $\mathcal{P} = i\gamma_0\gamma_1$, we know that $i\gamma_0\gamma_1 = i\tilde{\gamma}_0\tilde{\gamma}_1$. This implies two possible choices for the sign:

$$\gamma_0 \to \pm\gamma_1, \tag{2.21}$$

$$\gamma_1 \to \mp\gamma_0. \tag{2.22}$$

This is a gauge freedom and we choose to work with the lower sign choice in the following. It is straightforward to check that the unitary transformation of counter-clockwise exchange of the defects α and β is given by [36]

$$T_{\alpha\beta} = e^{\frac{i\pi}{4}} \exp\left(\frac{\pi}{4}\gamma_\alpha\gamma_\beta\right) = \frac{e^{\frac{i\pi}{4}}}{\sqrt{2}} \left(1 + \gamma_\alpha\gamma_\beta\right). \tag{2.23}$$

The second equation can be shown using the properties of the Majorana operators. The collection of all braiding operations forms a group − the so called braid group [10]. One can identify the Pauli operators $\sigma_1 = i\gamma_1\gamma_0$, $\sigma_2 = i\gamma_2\gamma_0$ and $\sigma_3 = i\gamma_2\gamma_1$ (see Ref. [25] and Subsection 2.2) as the generators of the braid group, because according to Eq. (2.23) we may write

$$T_{10} = e^{\frac{i\pi}{4}} \exp\left(-\frac{\pi}{4}\sigma_1\right), \; T_{20} = e^{\frac{i\pi}{4}} \exp\left(-i\frac{\pi}{4}\sigma_2\right), \; T_{21} = e^{\frac{i\pi}{4}} \exp\left(-i\frac{\pi}{4}\sigma_3\right). \tag{2.24}$$

This reveals a deep connection between the nonlocal Pauli operators and the braiding statistics. In Fig. 2.4, we see an example of the graphical representation of the exchange operation T_{12}. Using the Clifford algebra relations, it is straightforward to prove that $T_{\alpha\beta} = \sqrt{i\gamma_\alpha\gamma_\beta}$ [36]. Thus, by exchanging the Ising anyons twice, which is equivalent to one Ising anyon encircling the other, we obtain the Pauli operators:

$$T_{10}^2 = \sigma_1, \qquad T_{20}^2 = \sigma_2, \qquad T_{21}^2 = \sigma_3. \tag{2.25}$$

An exchange of e.g. 1 and 2 transforms a state Ψ, defined in the ground state manifold, according to $\Psi \to \exp\left(i\frac{\pi}{4}\sigma_2\right)\Psi$, while the encircling operation implements $\Psi \to \sigma_2\Psi$ [18]. As an example, we may consider the state $\Psi = |0_{01}, 1_{23}\rangle$ with n_{ij} the occupancy

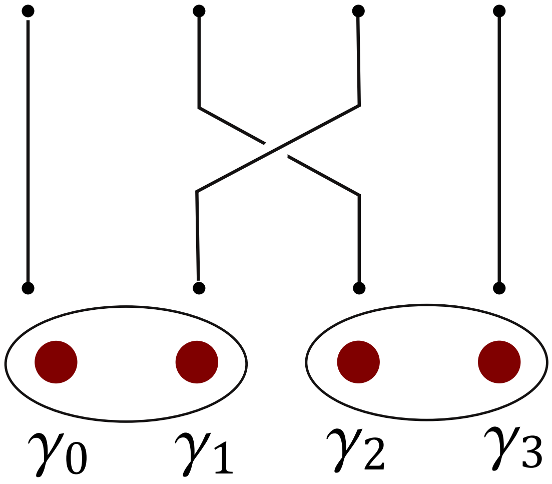

Figure 2.4: Geometrical representation of the elementary braiding operation of adiabatic and counter-clockwise exchange of the defects which bind the MZMs γ_1 and γ_2. The horizontal and vertical axes denote the spatial and temporal direction respectively. Braidings are equivalent if they can be smoothly deformed into each other without moving the start and endpoints (black dots) or crossing the strands [38].

of the fermion number operator $\hat{n}_{ij} \equiv \frac{1}{2}(1 + i\gamma_i\gamma_j)$. The exchange of MBSs belonging to different fermions creates a maximally entangled Bell state in the given basis [3], e.g.

$$T_{12}\left|0_{01}, 1_{23}\right\rangle = \frac{e^{\frac{i\pi}{4}}}{\sqrt{2}}\left[\left|0_{01}, 1_{23}\right\rangle + \left|1_{01}, 0_{23}\right\rangle\right], \tag{2.26}$$

whereas the qubit state (with fixed odd fermion parity) is flipped: $T_{12}^2\left|0_{01}, 1_{23}\right\rangle = \left|1_{01}, 0_{23}\right\rangle$. The exchange of Majoranas constituting the same fermion on the other hand results in a parity dependent phase factor being multiplied to the state.

2.3.2 Non-Abelian fusion rules

Braiding implies a time evolution in the degenerate ground state space due to the motion of indistinguishable anyons. To understand Majorana fusion rules, consider two Majorana zero-modes γ_1 and γ_2, bound e.g. to vortices of 2D TSCs or the terminations of 1D TSCs wires, which due to large separation have exponentially suppressed overlap. When the spatial distance between the associated MZMs carrying defects gets reduced, a hybridization term gradually appears. The degenerate ground state splits and the fusion may or may not give rise to an unpaired fermion. The case of a fermion corresponds to an excited state commonly denoted ψ, while the case of no fermion corresponds to the ground stated denoted 1. Hence, one writes [10, 36]

$$\gamma_1 \times \gamma_2 \rightarrow 1 + \psi. \tag{2.27}$$

One can view this as the projective measurement of the fermionic particle state that forms when the two MBSs are brought together, which can be empty or occupied at the cost of a finite energy. The two options illustrated in Eq. (2.27) are also known as fusion channels. Detection of the fusion rule (2.27), amounts to establishing the non-Abelian nature of MZMs, because the fusion of Abelian particles always exhibits just a single fusion channel [10]. In Chapter 3, we briefly mention a fusion rule detection scheme based on charge sensing [39] applied to Majorana qubit architectures in proximitized topological insulator nanowires.

2.3.3 Topological quantum computation

The idea to build topological quantum computers based on non-Abelian anyons generated great excitement in the quantum information community [10, 40], partially explaining the interest in MBSs. $2N + 2$ mutually far separated MZMs form a degenerate ground state manifold of dimension 2^N corresponding to N qubits if we restrict ourselves to a well defined charge parity. However, drawing on the Majorana box qubit discussion in subsection 2.2, we rather would like to think of $4N$ MZMs encoding N qubits with N constraints on the parities $\gamma_1\gamma_2\gamma_3\gamma_4$, $\gamma_5\gamma_6\gamma_7\gamma_8$,... which is known as "sparse" encoding [41].

A quantum computation is defined as a sequence of unitary operations called quantum gates. A set of gates is esteemed to be "universal" if an arbitrary computation can be performed. The unitary operations performed by braiding of Ising anyons, like e.g. $T_{01} = e^{i\frac{\pi}{4}(1+\sigma_1)}$ (see Eq. (2.24)), do not meet this requirement. In fact they are elements of the Clifford group. Remarkably only a single gate, e.g. the so called T-gate

$$\mathrm{T} = \begin{pmatrix} 1 & 0 \\ 0 & e^{\frac{i\pi}{4}} \end{pmatrix} \tag{2.28}$$

is missing to make it universal [41]. The latter would however be unprotected unlike the braiding unitary operations which are completely specified by the topology of the braid. Thus, by employing MBSs an element of the Clifford group can in principle be applied exactly to all decimal places while the T-gate can only be approximated. The finite excitation pairing gap Δ causes further limitations [42]. The timescale on which the braiding is performed is important. It has to be slower than $\hbar/\Delta_0$ because otherwise quasiparticles could be excited. On the other hand, the coherence time of the Majorana qubit clearly represents an upper limit on operation times.

2.4 Experimental identification of Majorana bound states

MBSs are neutral and spinless objects that do not couple to electric and magnetic fields. Due to electron non-conservation of the $U(1) \to \mathbb{Z}_2$ broken superconducting state, electrons provide a way to couple to the MBSs by using tunneling spectroscopy [40]. Probing the density of states of one end of a topological wire locally by means of conductance spectroscopy is therefore the most straightforward approach to obtain MBS signatures. To understand this point, first recall what happens for a trivial SC: the application of a voltage between a normal contact and the superconducting part leads to Andreev processes [27]. In such processes, the electron incoming from the normal metal is reflected as a hole from the tunnel barrier, while the current in the superconductor is carried by Cooper pairs. For a topological SC wire, in contrast, there is a resonant Andreev process at zero bias voltage when the energy of incoming electrons matches that of the Majorana zero-mode at the interface. In the zero temperature limit, the MBS gives rise to perfect Andreev reflection resulting in a robust zero-bias conductance peak (ZBCP) with a quantized maximum height of $G = 2e^2/h$ [43]. By investigating SM nanowires with proximity induced superconductivity, a 2012 Delft experiment provided the first experimental ZBCP evidence consistent with Majorana bound states [44]. In these experiments, a NbTiN superconductor was used to proximitize an InSb nanowire and the device as a whole was grounded. A recent success was that the height of the ZBCPs was confirmed to be $2e^2/h$ quantized [45, 46].

Naively, one might expect that a genuine topological superconducting wire reveals itself through the robustness and persistence of the quantized ZBCP signature for sufficiently strong magnetic field. In a similar spirit, the early experiments where partially celebrated as MBS verification implying that proximitized nanowires have been driven into the topologically superconducting regime. However, in this context, the results of further research implied that different alternative scenarios could also explain the same signatures. In light of these results that we will summarize now, the ZBCP is a necessary but not yet conclusive observation of MZMs.

First, disorder has been shown to be a possible origin of quantized zero-bias conductance peaks with unit spectral weight and robust to magnetic fields [47, 48]. This highlights the need to achieve fabrication of cleaner materials and devices and concerted endeavors already led to substantial progress in this regard [15].

Second, topologically trivial Andreev bound states (ABS) have been shown to be able to cause the same phenomenology as genuine (single) MBSs when they are detected on the basis of zero-bias conductance peaks [49, 50]. Andreev bound states are fermionic in nature implying that their creation operator $c = (\gamma_1 + i\gamma_2)/2$ can be split into a pair of Majorana operators $\gamma_1^\dagger = \gamma_1$, $\gamma_2^\dagger = \gamma_2$. The corresponding MBS component wave functions may actually have only a small overlap due to spatial displacement [50]. In the same reference it is shown that these so-called "partially separated Andreev bound states" (denoted ps-ABS in the same Ref.) are generic for low-energy spin-orbit coupled SM-SC heterostructures in the presence of a suitably oriented magnetic field [50]. These generic midgap ABSs in nanowires originate in inhomogeneities of the chemical potential or individual impurities behaving as quantum dots. Also the combination of spin-orbit coupling and Zeeman splitting permits Andreev bound states to reside close to the band center for finite values of the Zeemann field [51]. These ps-MBSs mimic topological unpaired MBSs so accurately that it has been pointed out that they may be useful for quantum computation because their non-Abelian braiding properties may be accessible [52]. We also point out that for the experimentalist it is not possible to know the value of the critical magnetic field independently, making it difficult to decide whether a measured ZBCP is seen on the topological or trivial side of the topological phase transition [51].

In summary, it is fair to say that the advances so far consist to a large extent of local probes and are consistent with the predictions for MBSs made by theory. But a false-positive interpretation is not yet ruled out. Nevertheless, the existing experimental observations represent crucial steps bringing us closer to topological quantum computation. Non-observation of a zero-bias peak in experiments would have falsified the Majorana wire hypothesis already some time ago. We also mention that there are many further experiments that have been performed which we have not mentioned here. E.g. another noteworthy breakthrough was achieved on Coulomb blockaded islands in 2016 at the University of Copenhagen [53]: the first systematic measurement of the finite-size exponential suppression of the ground-state degeneracy associated with overlapping Majorana bound states.

2.4.1 Next generation of experiments beyond local probes

As briefly stated in the introduction, the main aspects that must be investigated in order to demonstrate Majorana physics are broadly speaking the following: (a) verification of non-Abelian braiding properties, (b) corroboration that two MBS constitute a vastly nonlocal Dirac fermion, and (c) demonstration of unpaired Majorana bound states localized in TSCs. As discussed above, there is mostly a consensus in the condensed matter community that signatures of local probes such as ZBCP measurements (belonging to category (c)) are not able to unambiguously identify genuine MBSs. It thus seems clear that a next generation of experiments is needed to clarify the situation. There are various theoretical proposals available on how to achieve this goal [54]:

- For SC islands with more than two MBSs, a non-perturbative topological Kondo effect as discussed in Refs. [25, 26, 28, 55] is present. This could provide a smoking gun signature, also in light of related low-energy transport proposals for two-box setups [56]. The characteristic nonlocal transport features are expected at low temperatures $T < T_K$ and are predicted to disappear when a far-away lead is decoupled. However, reaching this regime is very challenging in experiments since the Kondo temperature T_K is predicted to be extremely low.

- In trijunctions formed from three TSCs, a single MZM is expected at the junction. Ref. [57] has shown that this state causes giant shot noise peaks when choosing commensurate voltages, like for instance $V_1 = -V/2$, $V_2 = 0$, $V_3 = +V/2$, on the TSC terminals. This effect disappears in the absence of such a protected zero-energy state.

- Another proposal made in Ref. [58] is to use interferometry by embedding a Coulomb-blockaded Majorana wire into a ring and then probe Aharanov-Bohm h/e-periodic conductance oscillations with the magnetic flux piercing the ring, see also Ref. [59]. For Andreev states, interference is argued to be suppressed, while for genuine MBSs one expects h/e oscillations, see also Refs. [29]. A related proposal is to study the Josephson current phase relation across a Majorana box with two MBSs [60]. For ABSs, the authors of this reference predict a phase shift when the gate parameter is shifted according to $n_g \to n_g + 1$, which in fact is absent for authentic MBSs.

- The detailed time dependence of the transient current after switching on the tunnel couplings in the standard ZBCP setting has been proposed as a signature allowing to distinguish genuine MBSs and ABSs in Ref. [61]. The fact that short-time transients can be affected by various other effects could make implementation of this proposal challenging in practice.

- Measuring the zero bias peaks at both ends of a TSC wire by studying the end-to-end correlations could provide a signature for authentic MBSs because one expects the ZBCPs to appear at both ends simultaneously [51]. In practice, this suggestion might be difficult to implement because it requires different gate settings at both ends of the wire. Furthermore, it is challenging to probe the same fermionic zero-mode.

- Thermoelectric noise due to the interplay of electric fields and temperature gradients has been proposed in Ref. [62] as a means to distinguish genuine MBSs and ABSs.

- Microwave spectroscopy of a Majorana wire could in principle also prove useful for distinguishing genuine MBSs and ABSs as discussed in Ref. [63]. The system requires spectroscopic measurement in the microwave regime and is thus more complicated to implement than a DC setup.

In light of the challenging nature of most of these experiments, the need to move on to a next generation of experiments on Majorana devices that go beyond local probes and are as simple as possible is quite substantial. This serves as an important motivation for this thesis. We believe that the simplicity can be found in transport spectroscopy − concretely, by measurements of currents and shot noise as will be discussed in Chapters 4 and 5.

Chapter 3

Majorana qubits in proximitized TI nanoribbon device architectures

This chapter contains a detailed study of the realization of Majorana based qubits built in platforms of TI nanoribbons in proximity to s-wave SCs [13, 14]. The chapter is structured as follows: Section 3.1 reviews TI nanoribbons and the emergence of MBSs in proximity to an s-wave SC. In Sections 3.2 and 3.3, we model and analyze the novel Majorana box qubit device setups which allow for gate tunable hybridization of MBSs and proof-of-principle experiments to test the devices. Finally, in Section 3.4, we give an outlook on long-term applications of the proposed qubit devices. Our research presented in this chapter has previously been published in Ref. [64].

3.1 TI nanoribbons and the emergence of MBSs in proximity to an s-wave SC

3.1.1 TI nanoribbons and surface Dirac theory

Let us start by introducing TI nanowires with a focus on their transport properties and reviewing the well established description in terms of Dirac surface models, which we will work with subsequently. In this subsection, we will see that topological insulator nanoribbons exhibit a finite-size gap. This gap can be closed to generate a single gapless helical 1D mode in the presence of an axial magnetic flux $\Phi = \Phi_0/2$, where Φ_0 is the magnetic flux quantum [65, 66, 67, 68, 69, 70]. A reader familiar with this subject may move on the next subsection.

The main ingredient are three-dimensional topological insulators (TIs) [16, 17], a type of matter which, as discussed in Chapter 2, exhibits the celebrated bulk-boundary correspondence. The nontrivial topology of the bulk matter goes hand in hand with a robust gapless Dirac-type surface state circumventing the fermion doubling theorem [71]. In this chapter, we consider nanowires made out of such topological insulator materials. The term ‘wire’ indicates effective one-dimensionality, i.e. the typical (nano) length scale of the width is small compared to the length of such a wire. Because of their layered structure, the nanowires of 3D TI materials commonly grow in a tape-like shape with rectangular cross sections of order $40 \times 100\mathrm{nm}^2$ [72, 73], explaining why the wires are referred to as nanoribbons. The Dirac fermion surface state governs the transport of three-dimensional topological insulator materials [16, 17] for chemical potential values within the bulk band gap E_g. The latter sets a length scale on which the surface Dirac fermion decays into the bulk, which is typically of the order of several nanometers. Quantum transport of bulk insulating TI nanowires with a width exceeding this length scale is therefore approximately accounted for by relying on surface theories (see e.g. Refs. [65, 66, 67, 68, 69, 70]). As explained in Refs. [65, 74], the surface theory can be obtained e.g. by starting from a massive Dirac Hamiltonian in three dimensions

$$H_{\mathrm{Bulk}} = \begin{pmatrix} -E_g & \boldsymbol{\sigma}\cdot\boldsymbol{p} \\ \boldsymbol{\sigma}\cdot\boldsymbol{p} & E_g \end{pmatrix}, \tag{3.1}$$

with E_g being the bulk band gap, $\boldsymbol{p} = -i\hbar\nabla$ the momentum operator and $\boldsymbol{\sigma} \equiv (\sigma_1, \sigma_2, \sigma_3)$ the vector of Pauli spin matrices. This Hamiltonian is defined in the space of the spin and pseudospin (sublattice) degrees of freedom and neglects other bands of the 3D TI energy spectrum. Let us assume that the interface of TI and the vacuum is defined by a position dependent normal vector $\hat{\boldsymbol{n}}$. Formally, one can derive the surface Hamiltonian by sending the mass parameter E_g to infinity away from the surface. In this way, one obtains the Hamiltonian [65]

$$H_{\mathrm{Surface}} = \frac{\hbar v}{2}\nabla\cdot\hat{\boldsymbol{n}} + \frac{v}{2}\left(\hat{\boldsymbol{n}}\cdot[\boldsymbol{p}\times\boldsymbol{\sigma}] + [\boldsymbol{p}\times\boldsymbol{\sigma}]\cdot\hat{\boldsymbol{n}}\right), \tag{3.2}$$

with v the Dirac velocity. This Hamiltonian describes a single species of a two-dimensional massless Dirac fermion. In the topology dominated transport of TI nanowires, accounting for the precise details of the wire geometry is often inessential in predicting transport properties. Indeed, the obtained low-energy band structure is very similar when the idealization of a cylindrical nanowire is invoked to describe a nanoribbon with the same cross section [14, 69, 70]. Assuming a cylindrical nanowire with radius R and in alignment with the z-axis, the Eq. (3.2) yields the TI wire Hamiltonian

$$H_0 = -i\hbar \upsilon_1 \sigma_y \partial_z + \frac{\hbar \upsilon_2}{R} \sigma_z i \partial_\theta, \tag{3.3}$$

with the coordinate θ parametrizing the wire circumference [14, 75, 76]. The parameters υ_1 and υ_2 are the Fermi velocities in the longitudinal and circumferential direction. In deriving this Hamiltonian, a unitary transformation (spin rotation) has been performed, which implies antiperiodic boundary conditions for the spinor wave function, i.e.

$$\psi(z, 0) = -\psi(z, 2\pi). \tag{3.4}$$

An immediate consequence of the antiperiodic boundary condition (3.4) is a gap in the spectrum, physically originating in the necessary finite transverse momentum. The energy scale $\sim \hbar \upsilon_2 / R$ characterizes the transversal confinement.[1]

Now, we imagine that a homogeneous axial magnetic field B is being turned on. According to the standard procedure of minimal substitution, the dimensionless magnetic flux

$$\varphi \equiv \frac{\Phi}{\Phi_0} \tag{3.5}$$

longitudinally threading the wire appears as an azimuthal vector potential in Eq. (3.3), yielding

$$H_0 = -i\hbar \upsilon_1 \sigma_y \partial_z - \frac{\hbar \upsilon_2}{R} \sigma_z (-i\partial_\theta + \varphi). \tag{3.6}$$

It is instructive to understand the qualitative features of the corresponding spectrum for a translationally invariant wire. We may perform a Fourier transformation of the spinor wave function, i.e.

$$\psi(z, \theta) = \int dz \sum_{j \in \left(\mathbb{Z} + \frac{1}{2}\right)} e^{ikz} e^{-ij\theta} \psi_{k,j}, \tag{3.7}$$

---

[1] In Ref. [76], a TI nanowire with arbitrary smooth, constant cross section perpendicular to the z-axis was considered. Hence, the surface of such a wire has no intrinsic Riemannian curvature. The corresponding Hamiltonian can be transformed to coordinates (s, z) in which it takes on the flat space form [76], $H = -iv\hbar \left[\sigma_z \partial_z + \sigma_y \partial_s\right]$. Consequently, the use of the Hamiltonian (3.3) is not as restrictive as it may seem.

where we introduced the axial momentum k and the quantized angular momentum j [76]. The fact that the summation is performed over half-integers accounts for the antiperiodic boundary conditions. The Hamiltonian separates into blocks of the form $H_{k,j} = \hbar v_1 k \sigma_y + \frac{\hbar v_2}{R}(j+\varphi)\sigma_z$. The spectrum is obtained by squaring $H_{k,j}$, which results in [14]

$$E_{k,j} = \pm\hbar\sqrt{v_1^2 k^2 + \frac{v_2^2}{R^2}(j+\varphi)^2}. \tag{3.8}$$

This spectrum has been plotted in Fig. 3.1.1, where the qualitative differences for different values of the dimensionless flux are being displayed. One of the key takeaways from the spectrum is that for $\varphi = 1/2$ there is a non-degenerate gapless linear band. This is precisely the condition for the underlying normal state of a TSC [6, 7]. The spectrum makes it intuitive to anticipate that the system in proximitiy to an s-wave SC will give rise to MBSs.

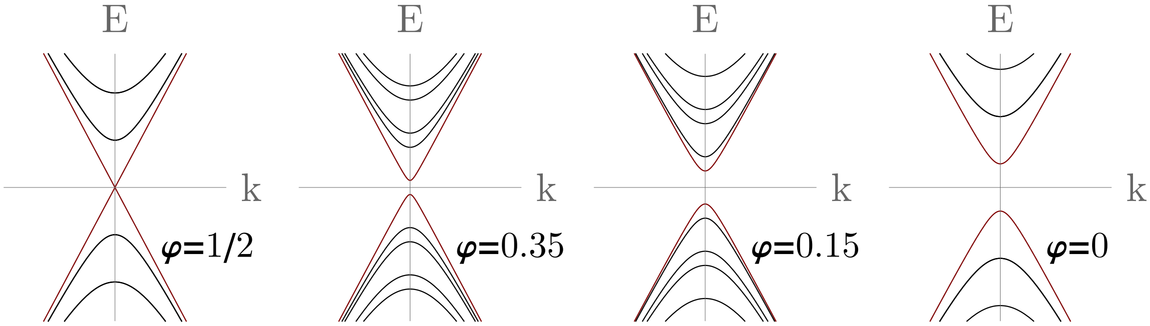

Figure 3.1: Energy spectrum (schematic) of a TI nanoribbon as a function of the longitudinal momentum k for different values of the threading dimensionless flux φ. For $\varphi = 1/2$ (left), the system is effectively time reversal symmetric and there is a non-degenerate linear gapless band. All the other bands have twofold degeneracy. Hence, for any value of the chemical potential there is an odd number of Fermi points for $k > 0$. In the absence of magnetic flux $\varphi = 0$ (right), there is a gap in the spectrum as discussed in the main text and every band has a twofold degeneracy. In the intermediate cases $\varphi = 0.35$ (center left) and $\varphi = 0.15$ (center right), the system is gapped and every band is nondegenerate. (The plot has been created with Mathematica.)

3.1.2 Dirac fermion model of proximitized TI nanoribbons

In the previous Subsection 3.1.1, we have seen that TI nanowires with half-integer axial flux quantum $\varphi = 1/2$, e.g. made of the strong TI Bi_2Se_3, exhibit an odd number of

Fermi points for $k > 0$ for any value of the chemical potential within the bulk band gap. According to Kitaev [6], in proximity to an s-wave SC, MBSs should emerge in such a situation if the superconductivity gaps the spectrum. For the proximitized TI nanowire system, topological superconductivity was first predicted by Cook and Franz in Refs. [13, 14] and subsequently analyzed e.g. in Refs. [77, 78, 79, 80]. We now discuss the proximitized system again using a surface Dirac fermion model, which is wrapped around the nanowire. For a cylindrical wire, due to its rotational symmetry with respect to the z-axis, the total angular momentum is conserved with half-integer eigenvalue j. According to the discussion in the previous subsection (see Eq. (3.6)), the effective Dirac surface Hamiltonian of the j-branch is given by

$$H_0 = -i\hbar v_1 \sigma_y \partial_z - \frac{\hbar v_2}{R(z)} \left(j + \varphi(z)\right) \sigma_z - \mu(z)\sigma_0, \tag{3.9}$$

where we now explicitly included a chemical potential μ. For given angular momentum quantum number $j \in \mathbb{Z} + 1/2$, the surface state in spin space is generally of the form [14]

$$\psi_j(z,\theta) = \frac{e^{ij\theta}}{\sqrt{2\pi}} \begin{pmatrix} e^{-i\theta/2} f_j(z) \\ e^{i\theta/2} g_j(z) \end{pmatrix}, \tag{3.10}$$

where θ is again the azimuthal coordinate parametrizing the circumference of the cylinder. The functions f_j and g_j are subject to the normalization condition

$$\int dz (|f_j(z)|^2 + |g_j(z)|^2) = 1. \tag{3.11}$$

Expressed in this way, the Hamiltonian effectively acts on spinor states $(f_j(z), g_j(z))^T$ in a reduced 1D description. We now add the superconducting term needed to account for the proximity effect with induced pairing Δ, which yields the description of the system via the Bogoliubov-de Gennes (BdG) Hamiltonian in Nambu space [14]

$$H_{BdG} = \begin{pmatrix} H_0(z) & i\sigma_2 \Delta(z) \\ -i\sigma_2 \Delta^*(z) & -H_0(z) \end{pmatrix}. \tag{3.12}$$

Surface states inside the gap of the bulk TI are then found as eigenstates of the BdG Hamiltonian. In Subsection 3.1.3 and Section 3.2, we will apply the Hamiltonian (3.12) to describe proximitized nanowire systems where Δ, φ and μ are functions of the coordinate z defined along the wire axis.

For an infinite, translationally invariant system with a uniform flux φ, the BdG solutions are plane waves with axial momentum k. Under these assumptions, the dispersion relation is given by [14]

$$E_{k,j,\sigma,\sigma'} = \sigma\sqrt{(\hbar v_1 k)^2 + (M_j + \sigma'\Delta)^2}, \tag{3.13}$$

where $\sigma, \sigma' \in \{\pm 1\}$. The parameter characterizing the size quantization gap is defined as

$$M_j = \frac{\hbar v_2}{R}\left|\varphi + j\right|. \tag{3.14}$$

The gap associated with the mode $j = -1/2$ is denoted

$$M_{-\frac{1}{2}} \equiv M(\varphi) \equiv \frac{\hbar v_2}{R}\left|\varphi - 1/2\right| \tag{3.15}$$

and is zero for half a flux quantum, i.e. for $\varphi = 1/2$. We consider TI nanoribbon cross sections that are sufficiently small such that $\sim \hbar v_2/R$ is a large energy scale and modes with angular momentum $j \neq -1/2$ can be neglected within a low-energy approximation scheme. We discuss possible causes and effects of flux mismatch away from $\varphi = 1/2$ in our discussion in Subsection 3.3.3. Note that a gapless branch exists for $M_j = \pm\Delta$, signaling a topological phase transition [4]. We will see in more detail in the next subsection how an interface of both types of gaps gives rise to MBSs localized at the ensuing domain walls. These MBSs emerge under the circumstances of Altland-Zirnbauer symmetry class D with broken spin $SU(2)$ symmetry and broken time reversal symmetry (TRS). This is despite the fact that the infinite proximitized TI nanoribbon with flux $\varphi = 1/2$ gives rise to an effective time reversal invariance placing it in symmetry class DIII, because the non-quantized magnetic flux at the wire ends breaks TRS [14].

3.1.3 MBS at the interface of TI wire segments of different width

A novel idea that will play a prominent role in our discussion of qubit architectures is to consider an interface separating TI nanowire segments of different radius such that the thicker right half with flux $\Phi = \Phi_0/2$ is proximitized and the thinner left half is not (see Fig. 3.2). We derive now the Jackiw-Rebbi zero-mode solution corresponding to a localized MBS at the interface. We treat the problem analogously to Refs. [13, 14], where a MBS arising at the interface with a magnetically gapped domain has been considered. In this subsection, we follow the presentation in these references using the effective BdG Hamiltonian (3.12) discussed in the previous subsection. The respective energy gaps M and Δ on the two sides are rooted in the size quantization[2] and the superconducting pairing. A radius smoothly varying in the interface region leads to a

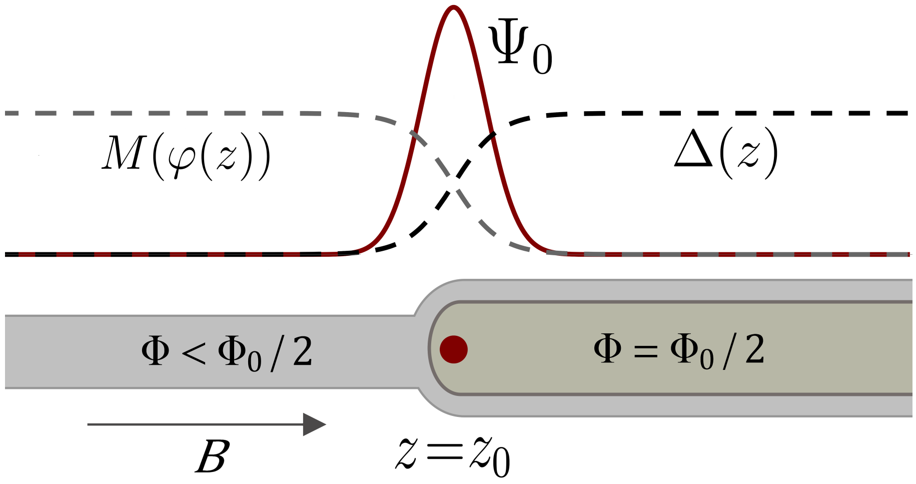

Figure 3.2: TI nanowire (gray) divided into two halves of different radius such that only the thicker right half is in proximity to an s-wave SC (gray-green). An axially aligned magnetic field B is adjusted in strength to generate a flux $\Phi = \Phi_0/2$ in the proximitized half (right). Consequently, the flux in the left half is $\Phi < \Phi_0/2$, implying the occurrence of a size quantization gap. This gap as well as the pairing gap may be approximated by real, smooth functions $M(\varphi(z))$ and $\Delta(z)$ describing the effective gaps of different origin in the effective BdG Hamiltonian given in Eq. (3.12). This leads to a Jackiw-Rossi Majorana zero-mode (red) localized at the interface $z = z_0$, where the two kinds of gaps coincide, i.e. $\Delta(z_0) = M(\varphi(z_0))$.

---

[2] As discussed in Subsection 3.1.2, we assume that modes with angular momentum $j \neq -1/2$ can be neglected at low energies.

smooth flux profile[3] $\varphi(z)$ and we assume $\Delta(z_0) = M(\varphi(z_0))$ at the interface point $z = z_0$, which is the condition for a gapless branch in the dispersion relation of Eq. (3.13). Furthermore, we assume the flux to vary only in the vicinity of the interface $z = z_0$ such that $\varphi(z \ll z_0) \simeq \varphi_0 < 1/2$ and $\varphi(z \gg z_0) \simeq 1/2$. Moreover, the gap function

$$M(\varphi(z)) = \frac{\hbar v_2}{R} \left|\varphi(z) - 1/2\right| \tag{3.16}$$

and the (assumed to be real) pairing gap $\Delta(z)$ vary only around $z = z_0$ as well. On the non-proximitized half we assume $\Delta(z \ll z_0) \simeq 0$ and $M(\varphi(z \ll z_0)) \simeq M_0 > 0$. On the other hand, for the proximitized half it holds that $\Delta(z \gg z_0) \simeq \Delta_0 > 0$ and $M(\varphi(z \gg z_0)) \simeq 0$.

In accordance with general principles, under such conditions a localized Jackiw-Rossi zero-mode comes into being in between the two domains. In the present case it corresponds to a localized Majorana zero-mode and can be approximated as the zero energy solution of the Hamiltonian (3.13) with the smooth, real gap functions discussed above. In the language of second quantization this solution can be expressed as [13, 14]

$$\hat{\Psi}_0(z) = \frac{1}{2} \int dz \left(f(z) - g(z) + f^\dagger(z) - g^\dagger(z)\right) u(z), \tag{3.17}$$

which is localized at $z = z_0$ with

$$u(z) = u_0 \exp\left(\int_{z_0}^{z} \frac{dy}{\nu_F} \left[M(\varphi(y)) - \Delta(y)\right] \right). \tag{3.18}$$

Hence, $1/M_0$ and $1/\Delta_0$ define length scales of exponential decay of $u(z)$ in the left and right region respectively. The operators f and g correspond to the functions defined in Eq. (3.10). Due to the reality property $u(z) = u^*(z)$, the field operator is Hermitian

$$\hat{\Psi}_0 = \hat{\Psi}_0^\dagger. \tag{3.19}$$

Thus, $\hat{\Psi}_0$ represents a Majorana zero-mode, because creation and annihilation are represented by the same operator. The topological nature of this Majorana zero-mode is reflected in the fact that the precise form of $M(\varphi(z)) - \Delta(z)$ does not matter, as long as the sign of this expression changes at $z = z_0$. Since the total number of unpaired MBSs in an electronic system must be even, there must exist another unpaired MBS in

---

[3] We neglect flux channelling effects due to the smallness of the magnetic susceptibility.

a finite system. It can neither be on the non-proximitized half nor in the gapped bulk of the proximitized half. Hence, it must exist on the other end independently of the details of the boundary condition [14].

3.2 Gate tunable coupling of Majorana states across a constriction

In this section, we quantitatively analyze the following idea: A weak link between two proximitized TI nanoribbons is engineered by means of a narrower, non-proximitized nanowire segment (see Fig. 3.3). For suitably adjusted flux, MBSs form at both sides of this central constriction, which is characterized by a local gap due to the lowered local flux. As will be quantitatively analyzed in detail below, this allows creation and annihilation of MBSs localized across the constriction, because two TSCs can be electrically disconnected by means of gating. In contrast to the discussion in Subsection 3.3.3, where the narrow wire segment was infinite, it now has finite length W.

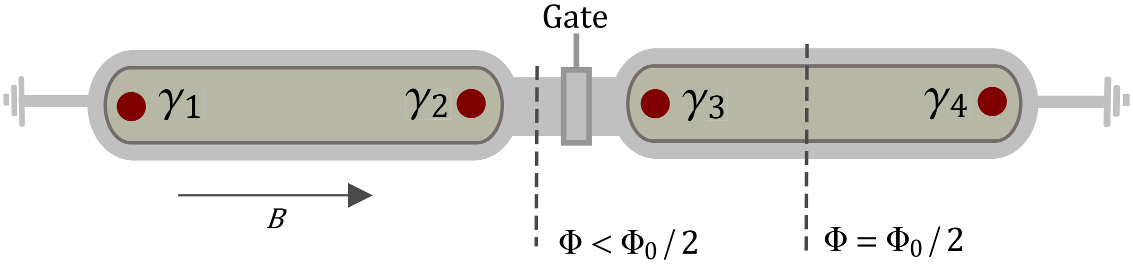

Figure 3.3: A narrow non-proximitized TI nanoribbon segment of length W is fabricated in between two thicker outer sections of the TI nanoribbon. These outer sections are proximitized by an s-wave SC (gray-green) and enclose a flux $\Phi = \Phi_0/2$ due to a fine tuned magnetic field B giving rise to four MBSs γ_α (red dots). The central constriction results in a local gap opening in the one-dimensional surface mode due to the enclosed magnetic flux $\varphi < 1/2$. As is quantitatively analyzed below, the top gate (center) allows to manipulate the hybridization of the MBSs γ_2 and γ_3 localized across the constriction. We assume the proximitized sections are long compared to the length scale $\xi_\Delta = \hbar v_1/\Delta$ such that the outer red dots are effective MZMs.

For convenience, we model the device depicted in Fig. 3.3 with system parameters that exhibit a step-like dependence on the z coordinate along the wire. To derive the finite wavefunction overlap of the inner MBSs γ_2 and γ_3 (see Fig. 3.3), we assume for the moment the length L of the two outer TSCs to be infinite. Hence, we model the radius of the cylindrical wire as a Heaviside step function,

$$R(z) = R_0 + (R - R_0)\Theta(|z| - W/2) \tag{3.20}$$

with R the radius of the outer part and $R_0 < R$ the smaller radius of the inner part. It assumes interfaces with extension over a few lattice sites which are of order of 3nm [17]. The axial magnetic field B is fine tuned such that the dimensionless flux $\varphi(z) \equiv \Phi(z)/\Phi_0$ takes on the value 1/2 in the outer parts. Thus, as a function of the z parameter, we model φ as

$$\varphi(z) = \varphi_0 + \left(\frac{1}{2} - \varphi_0\right) \Theta(|z| - W/2). \tag{3.21}$$

The dimensionless flux through the constriction φ_0 is calculated to be $\varphi_0 \equiv R_0^2/(2R^2) < 1/2$. The associated size quantization gap is denoted by

$$M_0 \equiv M(\varphi_0) = \frac{\hbar v_2}{R} \left|\varphi_0 - 1/2\right|. \tag{3.22}$$

The relation (3.21) neglects the effect of magnetic screening (flux channeling) in the constriction, which is justified because the magnetic susceptibility is small, especially since the surface state spectrum is gapped. For the superconducting gap $\Delta(z)$ induced by the proximitized s-wave SC in the outer regions of the device, we make the assumption that its absolute value is the same on the left and right segments, i.e. $|\Delta(|z| > W/2)| = \Delta$, with $\Delta \in \mathbb{R}$. We include a difference between the superconducting phases on both sides denoted by ϕ, i.e.

$$\Delta(z) = \Delta e^{-\mathrm{sgn}(z) i\phi/2} \Theta(|z| - W/2). \tag{3.23}$$

This relation neglects the breaking of rotational symmetry due to the s-wave superconductors, which has been discussed in Ref. [77]. We mention that ϕ will be a dynamical quantity in a Coulomb blockaded device. We also include an electrochemical potential term μ in the constriction which is induced by means of the gate electrode on top of the constriction (see Fig. 3.3)

$$\mu(z) = \mu \Theta(W/2 - |z|). \tag{3.24}$$

Despite this convenient choice, we note that finite μ in the outer region $|z| > W/2$ is not predicted to result in qualitatively different physics.

To construct the solution of the 1D BdG equation [5],

$$H_{BdG}\Psi = E\Psi, \tag{3.25}$$

we take note that the interface points, $z = \pm W/2$, define three regions in which the problem is effectively uniform. For large energies, the solution is obtained via a plane-wave ansatz. But we are interested in the low-energy subgap regime $|E| < \min(\Delta, M_0)$, where angular momentum modes with $j \neq 1/2$ are negligible for moderate values of the chemical potential $\mu < M_0$. Making an appropriate evanescent state ansatz in the three regions, we can write the requirement of continuity of the spinor wave function $\Psi(z)$ in the form of a corresponding condition of a vanishing determinant

$$D(E) = 0. \tag{3.26}$$

Further details on the derivation and the specific form of the determinant $D(E)$ for $|E| < \min(\Delta, M_0)$ are provided in Appendix A. The relation (3.26) contains the information about the low-energy spectrum, which for general parameter values is obtained via numerical solution. We find the robust existence of subgap states at $E = \pm\varepsilon$, which can be confirmed to constitute the expected pair of MBSs. With the self-consistent assumption $|\varepsilon| < \min(\Delta, M_0)$, a formula for ε can be derived from Eq. (3.26) by second-order expansion of $D(E)$ in E. The Majorana hybridization energy associated with the inner two MBSs γ_2 and γ_3 is then given by

$$\varepsilon(\phi) = \varepsilon(0)\cos\left(\frac{\phi}{2}\right), \tag{3.27}$$

where the energy at vanishing phase difference, $\phi = 0$, is given by

$$\varepsilon(0) = \frac{2\Delta}{M_0}\frac{(\hbar v_1/\xi)^2}{\Delta + \hbar v_1/\xi}e^{-W/\xi}. \tag{3.28}$$

Here, we have introduced the localization length scale

$$\xi(\mu) = \frac{\hbar v_1}{\sqrt{M_0^2 - \mu^2}} \tag{3.29}$$

of wave function decay into the non-proximitized part. The central constriction of width W realizes an insulating tunneling barrier between two 1D TSCs with MBSs at their terminations. The dependence of the splitting $\varepsilon(\phi)$ of the ground state degeneracy on the difference in the SC phases ϕ exhibits 4π-periodicity, according to Eq. (3.27). This is a consequence of the fractional Josephson effect [4, 40] and, hence, in agreement with the theoretical predictions for a Josephson junction with MBSs. The exactness of the 4π-periodicity is an artifact of the fact that only the $j = -1/2$ mode has been included in the derivation. The surface states with $j \neq -1/2$ cause small conventional 2π-periodic contributions.

The size of the hybridization ε is mainly determined by the length of the constriction W in units of the length scale $\xi\,(\mu)$. In particular, the splitting is exponentially suppressed, $\varepsilon \sim \exp\left(-W/\xi\right)$, and thus negligible for sufficient spatial distance $W \gg \xi$ between the MBSs. In the limit $W \to \infty$, a pair of exact Majorana zero modes is present and the approximate ground state degeneracy becomes exact. The Bogoliubov-de Gennes solution (see Appendix A) $\Psi(z)$ describing the Majorana states localized at the interfaces decays exponentially into the outer segments $|z| > W/2$ on the length scale

$$\xi_\Delta = \frac{\hbar \upsilon_1}{\Delta}. \tag{3.30}$$

We now consider the example of a $\mathrm{Bi_2Se_3}$ nanowire with radius $R = 35nm$ in the outer regions and an inner radius of $R_0 = R/2$. The Fermi velocities of $\mathrm{Bi_2Se_3}$ along the e_z direction is given by $\hbar\upsilon_1 = 226\mathrm{meV} \times \mathrm{nm}$ and along the azimuthal direction it is $\upsilon_2 = 1.47\upsilon_1$ [68]. The size quantization gap $M_0 \simeq 7.14\mathrm{meV}$ reigning in the constriction is large compared to the proximity gap, which we assume to be $\Delta = 0.18\mathrm{meV}$ in the outer regions. In Fig. 3.4, we plot the Majorana hybridization energy $\varepsilon = \varepsilon(0)$ depending on the constriction length W for different fixed values of the electrochemical potential μ. This plot has been obtained by numerical solution of Eq. (3.26) and is in agreement with the exponential suppression $\varepsilon \sim \exp\left(-W/\xi\right)$ for $W \gg \xi$ predicted in formula Eq. (3.28). Moreover, the length scale $\xi = \xi(\mu)$ of decay in Fig. 3.4 is consistent with Eq. (3.29). We infer from Fig. 3.4 that in the limit of a short constriction, $W \to 0$, we find $\varepsilon \to \Delta$. This behavior is expected since the MBSs increase their overlap and eventually reach the quasiparticle continuum of the spectrum.

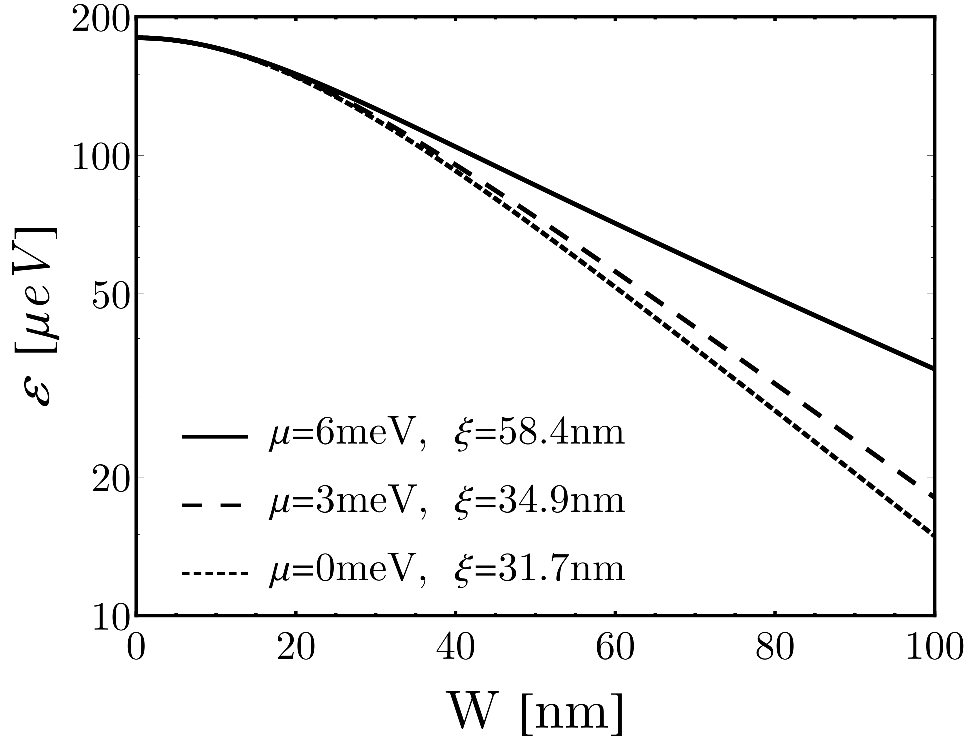

Figure 3.4: Hybridization ε (in units of μm) of the two inner Majorana states γ_2 and γ_3 for $\phi = 0$ plotted (semi-logarithmically) as a function of the length W (in nm) of the unproximitized central part for the device displayed in Fig. 3.3. The proximity gap and the size quantization gap are assumed to be $\Delta = 0.18$meV and $M_0 \simeq 7.14$meV respectively. Furthermore, we consider the TI nanoribbon to be made of Bi_2Se_3. We display the result for several values of the electrochemical potential μ in the central region. The corresponding length scale ξ is shorter for smaller values of μ. In the case that $W \gg \xi$, the plots are in agreement with the prediction $\varepsilon \sim e^{-W/\xi}$ of Eq. (3.28). On the other hand, for $\varepsilon \to \Delta$ we obtain $W \to 0$ as expected. The plot was taken from our publication Ref. [64].

In practice, the constriction width W is constant, but the experimentalist can tune the effective length scale $\xi\,(\mu)$ in Eq. (3.29) by changing the local chemical potential using a local gate, see Fig. 3.3. Hence, the gating allows to manipulate the effective distance between the two inner Majorana states. Increasing the electrochemical potential μ makes the weak link more transparent and the coupling ε is enhanced. The coupling is at its minimum for $\mu = 0$. In Fig. 3.4, the hybridization ε is numerically plotted as a function of μ. These numerical plots are consistent with the analytical formulas stated in Eq. (3.28). Thus, the results displayed in Fig. 3.5 indicate that ε can be conveniently controlled.

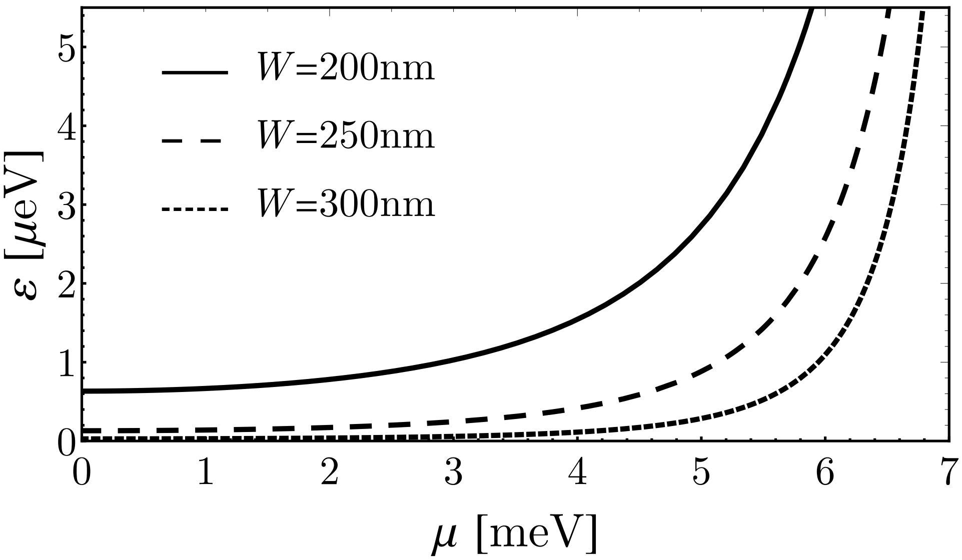

Figure 3.5: Hybridization ε (in units of μm) between the inner Majorana states γ_2 and γ_3 for $\phi = 0$ plotted as a function of the electrochemical potential μ (in units of meV). The plots are displayed for the constriction widths $W = 200$nm, $W = 250$nm and $W = 300$nm. Like in Fig. 3.4, we consider Bi_2Se_3 and use the parameters $\Delta = 0.18$meV and $M_0 \simeq 7.14$meV. The hybridization ε is minimal for $\mu = 0$ and remains close to this value for $\mu \ll M_0$. However, at some point ε begins to grow at a bigger rate upon the increase of μ. The plot shows that the coupling of the MBSs can be manipulated via local gating in the constriction. The plot was taken from our publication Ref. [64].

3.3 Majorana box qubits from TI nanoribbons

The Subsection 3.3.1 is inspired by the Refs. [11, 12] and analyzes the Coulomb blockaded version of the proposed device presented in the previous section to perform readout and initialization. In Subsection 3.3.2, we study the options to realize devices with switchable grounding of the TI nanoribbon platform following Ref. [39]. Finally, in Subsection 3.3.3, we compare the TI nanoribbon based approach to Majorana qubits to the SM based approach.

3.3.1 Floating box qubit and elementary quantum operations

To encode topologically protected qubits, we consider the floating version of the TI nanoribbon device, as shown in Fig. 3.6, with four MBSs on the box defining the corresponding Hilbert space. We assume the outer MBSs γ_1 and γ_4 to be effective zero-modes. This means that the length L of the proximitized segments is large compared to $\xi_\Delta = \hbar v_1/\Delta$ such that the wave functions of the outer MBSs γ_1 and γ_4 have negligible overlap with all other MBSs hosted by the floating island.

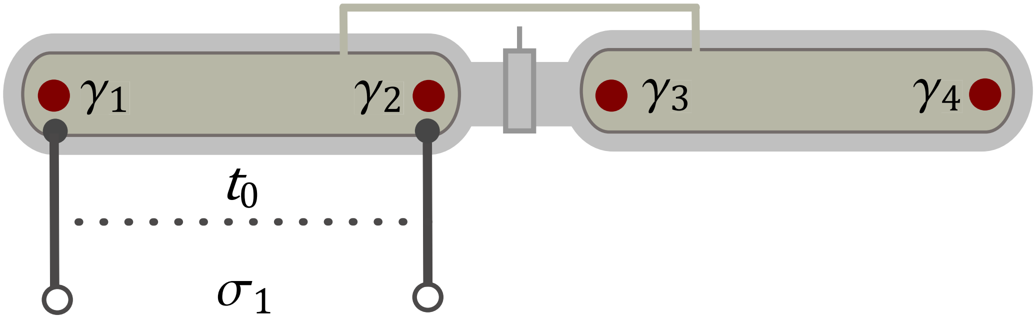

Figure 3.6: Floating version of the quantum device shown in Fig. 3.3 with four localized MBSs γ_α (red dots). The s-wave SCs (gray-green) coating the TI nanoribbon (gray) on the outer regions have a SC bridge in between them so that the Majorana island is characterized by a single charging energy E_C. Normal leads (thick black lines) are tunnel coupled to MBSs, and coupled amongst themselves by an interference link t_0. This is to make use of interferometric readout schemes [11, 12] of the nonlocal Pauli operators, here $\sigma_1 = i\gamma_1\gamma_2$.

Note that the two superconducting halves are connected by a superconducting bridge (see Fig. 3.6) such that the box is characterized by a single charging energy E_C. In this case, the effective Hamiltonian of the qubit device capturing the physics on energy scales small in comparison to Δ and E_C is dominated by the hybridization energy ε given in Eq. (3.27). It reads

$$H_{\text{eff}} = \varepsilon(i\gamma_2\gamma_3) + E_C \left(\hat{N} - n_g\right)^2, \tag{3.31}$$

where a side-gate controls the charging term via the back gate parameter n_g. The operator $\hat{N} = 2\hat{N}_s + \hat{n}_{12} + \hat{n}_{34}$ counts the number of electrons on the island, where $\hat{N}_s$ counts the island Cooper pairs, and $\hat{n}_{12} + \hat{n}_{34}$ yields the number of fermions in the Majorana domain. Here, $\hat{n}_{ij} \equiv d^\dagger_{ij} d_{ij}$ is the occupation of the nonlocal fermion $d^\dagger_{ij} = \gamma_i - i\gamma_j$. Physically, the low-energy Hamiltonian H_{eff} neglects quasiparticles above the topological gap Δ as well as the high lying surface states with $j \neq -1/2$. The degree to which the inner Majoranas at the two sides of the constriction hybridize sets the qubit lifetime due to dephasing. On time scales below this dephasing time and below the characteristic poisoning time, the state of the qubit is restricted to the almost degenerate low-energy ground state manifold. For n_g close to an integer value, the charge quantization on the box implies that global fermion parity is fixed [25]. For concreteness, we assume the parity to be odd, i.e.

$$\mathcal{P} \equiv \gamma_1\gamma_2\gamma_3\gamma_4 = -1. \tag{3.32}$$

Analogously to the box qubits based on SM nanowires discussed in Section 2.2, the box degrees of freedom are given by the fractionalized Majorana bilinears [25]

$$\sigma_1 = i\gamma_1\gamma_2, \quad \sigma_2 = i\gamma_3\gamma_2, \quad \sigma_3 = i\gamma_3\gamma_1. \tag{3.33}$$

Since fermion parity is conserved, the identification of a bilinear, e.g. formed from the pair γ_2 and γ_3, always automatically determines the bilinear formed from the remaining two Majoranas, e.g. $i\gamma_1\gamma_4 = -i\gamma_2\gamma_3$. Labeling eigenstates based on the eigenvalues n_{ij}, the nonlocal logical qubit state $|\psi\rangle$ can be encoded in the 2D Hilbert space spanned by the states $|\uparrow\rangle \equiv |0_{12}, 1_{34}\rangle$ and $|\downarrow\rangle \equiv |1_{12}, 0_{34}\rangle$. Qubit states can now be defined as $|\psi\rangle = \alpha|\uparrow\rangle + \beta|\downarrow\rangle$ with $\alpha, \beta \in \mathbb{R}$. Hence, it holds e.g. that $\sigma_1|\uparrow\rangle = |\uparrow\rangle$ and $\sigma_1|\downarrow\rangle = -|\downarrow\rangle$. To readout and initialize the qubit, the interferometric projective conductance measurement scheme [11, 12] reviewed in Chapter 2 can be applied. In this way, all bilinears in Eq. (3.33) can be addressed via electrodes tunnel-coupled to the corresponding pair of MBSs. We point out that the interference link required to read out $\sigma_2 = i\gamma_3\gamma_2$ does not have to be realized as an additional structure, because the superconducting bridge (see Fig. 3.6) can be used for this purpose [12].

3.3.2 Devices with switchable grounding

We now discuss the option to switch the devices from the grounded to the non-grounded regime and vice versa. This has been discussed to be useful for "parity-to-charge" conversion protocols, as well as for fusion rule or braiding confirmation, by Aasen et al. in Ref. [39]. The discussion in this reference is geared to the semiconductor based platform but can be applied to the TI nanoribbon based platform as well.

The switchable grounding requires to connect the proximitized nanoribbon which hosts MBSs, to a grounded superconducting bulk reservoir. To implement such a coupling, we again employ a non-proximitized TI nanoribbon with a lesser cross section than the proximitized nanoribbon, as shown in Fig. 3.7. The principle is the same as for the weak link connecting the two poximitized TI nanowire segments discussed in Section 3.2: Due to geometric confinement, the connecting section is gapped and, therefore, constitutes a tunnel junction.

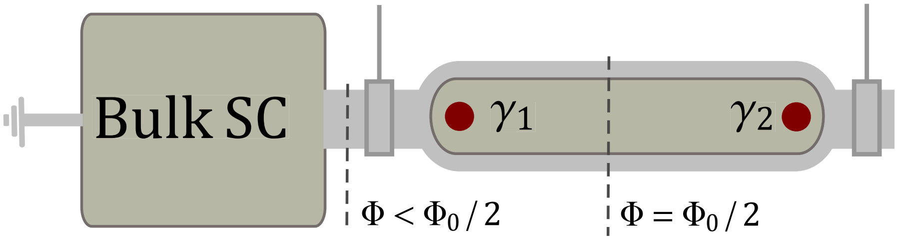

Figure 3.7: Switchable grounding [39] can be achieved by once again employing a non-proximitized TI wire segment of smaller cross section. In the present case, this segment is used to couple a proximitized TI nanoribbon realizing a TSC to a grounded bulk superconducting reservoir. A local top gate is installed at the narrowed segment and allows to control the Josephson coupling between the reservoir and the TSC. In this way, the ratio of charging energy E_C and Josephson energy E_J can be tuned. Switching from the grounded regime ($E_J \gg E_C$) to the floating regime ($E_C \gg E_J$) makes it possible to achieve "parity-to-charge conversion" and to read out the corresponding charge states using a charge sensor [39].

The Hamiltonian of the device shown in Fig. 3.7 contains not only the charging energy E_C, but also the Josephson energy E_J describing the coupling to the bulk superconductor due to Cooper pair tunneling [25, 28, 39],

$$H_{\text{eff}} = \varepsilon(i\gamma_2\gamma_3) + E_C\left(2\hat{N}_s + \hat{n}_{12} + \hat{n}_{34} - n_g\right)^2 - E_J\cos\hat{\phi}_s. \tag{3.34}$$

The hybridization energy ε of the inner MBSs γ_2 and γ_3 has already been stated in Eq. (3.27). Furthermore, $\hat{N}_s$ and $\hat{n}_{12}+\hat{n}_{34}$ are defined as in 3.3.1. Note that $\hat{N}_s$ is canonically conjugate to the phase difference $\hat{\phi}_s$ between the left and right superconductors. The tunneling strength and, thus, the Josephson energy E_J can now be influenced by a gate placed on top of the narrow TI wire segment. This makes it possible to tune from the grounded regime ($E_J \gg E_C$), where two SCs behave essentially like a single SC, to the floating regime ($E_C \gg E_J$) and vice versa. The tuning of the ratio E_J/E_C provides a way to read out $i\gamma_1\gamma_2$ by converting the corresponding parity eigenstates into charge states [39]. The latter can be read out by a capacitively coupled single electron transistor acting as a charge sensor. For nanowires of length of a few μm, a typical charging energy is $E_C \simeq 0.1$K. We then expect a tunable parameter range of order $0.1 \lesssim E_J/E_C \lesssim 10$ [64].

3.3.3 Majorana qubit comparison: TI nanoribbon vs SM platform

In this section, we critically discuss and evaluate the proximitized TI nanoribbon platform and compare it to other approaches to Majorana qubits. Moreover, we discuss potential challenges of the devices e.g. due to harmful physical mechanisms. The MBSs in the TI nanoribbon construction derive from the protected surface states of a topological insulator. Those surface states are endowed with robust protection from pair-breaking disorder as well as from elastic impurity scattering [75]. The device cleanliness of the semiconducting nanowire platform is presently more pure [15, 64]. Thus, advances in the experimental physics of TI nanoribbons are required for proof-of-principle demonstration of the platforms practicability, e.g. towards QIP applications.

An important property of the MBSs is their typical localization length scale. For the TI nanoribbon platform the decay of the Majorana wavefunction into the proximitized segment is characterized by the length scale $\xi_\Delta = \hbar v_1/\Delta$, which is vastly longer than that for the decay into the constriction. If we assume a Bi_2Se_3 nanowire and a proximity gap $\Delta = 0.18$meV, we obtain $\xi_\Delta = 1.25\mu$m. This estimate reveals that the proximitized TI nanowires have to be of substantial length $\gtrsim 5\mu$m in order to have sufficiently small overlap of γ_1 and γ_2 (γ_3 and γ_4). We note in this context that nanoribbons of such length are already available [72, 73]. Nevertheless, the required wire length is a slight disadvantage in comparison to the semiconductor nanowires, where a spin-orbit coupling energy of order $\hbar\alpha \approx 20\text{eV} \times \text{nm}$ corresponds to a localization length of 125nm [81]. The MBS localization length scale reigning in the inner, non-proximitized segment is given by $\xi\left(\mu\right) = \hbar v_1/\sqrt{M_0^2 - \mu^2}$ and is typically shorter than ξ_Δ for realistic system parameters, as discussed in Section 3.2.

Experimentally, it may be challenging to arrange the magnetic flux in such a way that it realizes the desired value $\varphi = 1/2$ in the proximitized segments. Despite the fact that magnetic fields can be fine tuned with great precision, a mismatch of the flux could be caused for several reasons:

1. The area of cross section is not completely homogeneous. Such imperfections imply that the flux will display small variations as a function of z.
2. The spatial orientation of the TI nanoribbon has to be completely parallel to the applied magnetic field. This is another source of error which also causes slight breaking of the rotational symmetry leading to admixtures of the higher-energy states with $j \neq -1/2$.
3. The different segments of the device have to be aligned along a common axis, which constitutes another source of error.

Despite these factors, we expect that the discrepancy in magnetic flux can be limited to be a rather weak perturbation. A flux $\varphi = \frac{1}{2} + \delta\varphi$ with small constant mismatch $\delta\varphi \ll 1$ results in a finite mass parameter $M(\varphi) = \frac{\hbar v_2}{R}\left|\delta\varphi\right|$ in the proximitized regions. We note that in this case a finite electrochemical potential $\mu_S = \mu(|z| > W/2)$ in the proximitized regions is required, i.e. Eq. (3.24) has to be modified. More precisely, $M(\varphi) < |\mu_S| < \hbar v_2/R$ is necessary for well-defined 1D surface states for $\Delta = 0$, which is the condition for MBSs at finite pairing. In summary, we anticipate that the inevitable flux discrepancy is not detrimental to the robustness of the MBSs. The electrochemical potential μ_S (focusing on the case $\varphi = 1/2$) does not change the qualitative results: the quantity μ_S manifests itself mainly in the difference $\mu - \mu_S$ which enters the formulas.

This is expected since the dispersion of the $j = -1/2$ states is linear in the absence of a proximitized superconductor.

In view of quantum hardware applications, the maximal time scale τ_0 on which the Majorana box quit is operational is an important characteristic property. As discussed above, in our proposed platform the qubit splitting due to the wave function overlap of the two inner MBSs eventually dephases the state of the qubit. Thus, the time scale is given by

$$\tau_0^{-1} = \varepsilon(0) \tag{3.35}$$

with $\varepsilon(0)$ as given in Eq. (3.28). For a given device this scale can be maximized by designing the constriction section W as long as possible. For $W = 300$nm an electrochemical potential within the window $|\mu| < 0.2$meV keeps the hybridization bounded as follows: $\varepsilon(0) < 0.027\mu$eV. This corresponds to coherence time scales longer than $\tau_0 > 2.4\mu$s. Notably, the time scale for semiconductor nanowires is shorter [39], i.e. this is a clear advantage of the proximitized nanoribbon architecture. While the maximum of τ_0 is achieved for $\mu = 0$, there is reasonable range for the chemical potential set by the parameter M_0 in Eq. (3.22) in which the hybridization is not affected too much. For the proximitized semiconducting nanowires on the other hand, the workable interval is smaller. Indeed, the chemical potential needs to be tuned to the bottom of the band. This makes the states more sensible to disorder.

Semiconducting nanowires currently represent the experimentally most advanced platform toward MBS realization. In such devices the QP poisoning time has been studied and was found to be $\gtrsim 1\mu$s [31]. Similar investigations still have to be performed for the proximitized TI devices. This is another important aspect in a comprehensive platform comparison. Regarding the links that provide a way to interferometrically read out and initialize the qubit, the TI nanoribbon platform offers the perspective to forge these links from the TI itself (see Fig. 3.3). This may be another advantage compared to SM devices, where the need for separate links has proven to be challenging [82].

3.4 Conclusions and outlook

In this chapter, we have presented new design architectures for Majorana qubits that are based on TI nanoribbons, e.g. made of $\mathrm{Bi_2Te_3}$ or $\mathrm{Bi_2Se_3}$. In proximity to an s-wave SC and in the presence of a fine tuned axial magnetic field, TI nanoribbons realize a 1D TSC. In the proposed layouts, shown e.g. in Fig. 3.3, two linearly aligned TSCs of this kind are connected by a non-proximitized narrow TI constriction, effectively dividing the TSC into two halves. Due to lowered magnetic flux in the TI element connecting the two halves, a size quantization gap is opened locally. As discussed in Sections 3.1 and 3.2, MBSs are localized at the two domain walls that separate regions either dominated by the pairing gap Δ or by the size quantization gap M_0. In Section 3.2, we have calculated the coupling of the two MBSs (γ_2 and γ_3 in Fig. 3.3) localized across a constriction of finite length W, with the result being stated in Eqs. (3.27) and (3.28). Importantly, we identified the length scale $\xi(\mu) = \hbar\upsilon_1/\sqrt{M_0^2 - \mu^2}$, with υ_1 being the Fermi velocity in longitudinal direction. This length scale sets the effective distance between the inner MBSs γ_2 and γ_3. Tuning of the local electrochemical potential μ in the constriction therefore enables to control the hybridization of the pair of MBSs. This tuning can be conveniently performed via gating and allows to switch from a regime where the Majoranas are coupled, to a regime where the coupling is suppressed and the quantum information is (better) protected from decoherence. Furthermore, the derived result for the hybridization exhibits 4π-periodicity in the superconducting phase difference ϕ, which is in agreement with the theoretical predictions for the fractional Josephson effect [4, 40].

Throughout this analysis, several approximations have been made. First, the results have been derived under the assumption that the two outer MBSs (γ_1 and γ_4 in Fig. 3.3) are far enough away to have negligible wavefunction overlap. Moreover, we worked in a low-energy approximation scheme throughout this chapter. Thus, we have neglected modes with angular momentum $j \neq -1/2$ under the assumption that the energy scale $\sim \hbar\upsilon_2/R$ is large. Perturbative inclusion of the bands with $j \neq -1/2$ leads to corrections, e.g. 2π-periodic admixtures are expected in the result for the Majorana coupling stated in Eq. (3.27). Moreover, we neglected any contributions from the bulk of the TI nanoribbon. The effects of flux mismatch were discussed in Subsection 3.3.3. Despite the simplifications, we are confident that the most essential low-energy features were captured in the modeling.

We note that an alternative technique to describe the device consists in the use of

$\boldsymbol{k} \cdot \boldsymbol{p}$-theory. This approach is based on the low-energy bulk Hamiltonian and requires imposition of Dirichlet boundary conditions on the nanoribbon surface (see e.g. Ref. [68]). The problem posed in this way can be approached numerically. The general expectation is that the essential theoretical results described above can be reproduced with this method.

As long as functional Majorana qubits are not at our disposal, it is important that different promising proposals are being actively pursued, because it is difficult to predict a priori which approach will work best. The comparison to the semiconducting quantum wire platform, performed in Subsection 3.3.3, has shown that, in fact, TI nanoribbon Majorana qubits represent a promising and viable alternative. The reasons for this include but are not limited to the fact that the TI nanoribbon surface states can be anticipated to yield MBSs of reasonably high robustness, possibly more so than for SM wire platforms, because of the linear spectrum of the 1D modes. Moreover, the only requirement for the chemical potential is that it lies within the bulk band gap. In contrast to other TI based proposals, a ferromagnetic insulator is not necessary to realize an edge localizing Majorana states.

Overall, we believe the platform could prove to be versatile and accommodating for the purpose of demonstrating and ultimately using Majorana qubits. However, further experimental progress has to be made regarding the material platform. TI nanoribbons of sufficient length are already available [72, 73]. And moreover, experiments have reported Andreev reflection from the surface states in a TI nanowire Josephson junction based on the TI material $\mathrm{BiSbSeTe_2}$ [83, 84]. This gives further credence to the prospect that the achievement of topological superconductivity in these platforms is realistic (as was also pointed out in Ref. [76]). A proximitized nanowire could initially be checked by making point contacts at the ends so that the ZBCPs and their dependence on the flux can be measured. In the next subsection, we discuss applications of the device platforms that can be envisioned once they are under experimental control.

3.4.1 Outlook: Majorana surface code and beyond

We now turn to more ambitious long-term applications of the TI nanoribbon qubit devices. We start by a discussion of a particularly attractive application, namely, the Majorana surface code. This code holds promise for efficient quantum information processing and its theory has been developed in the Refs. [85, 86, 87, 88]. Majorana surface code implementations require to manufacture extended 2D network structures comprising many tunnel coupled Majorana box qubits, see Fig. 3.8. Hence, a precondition for the Majorana surface code is that the qubits are established and under experimental control.

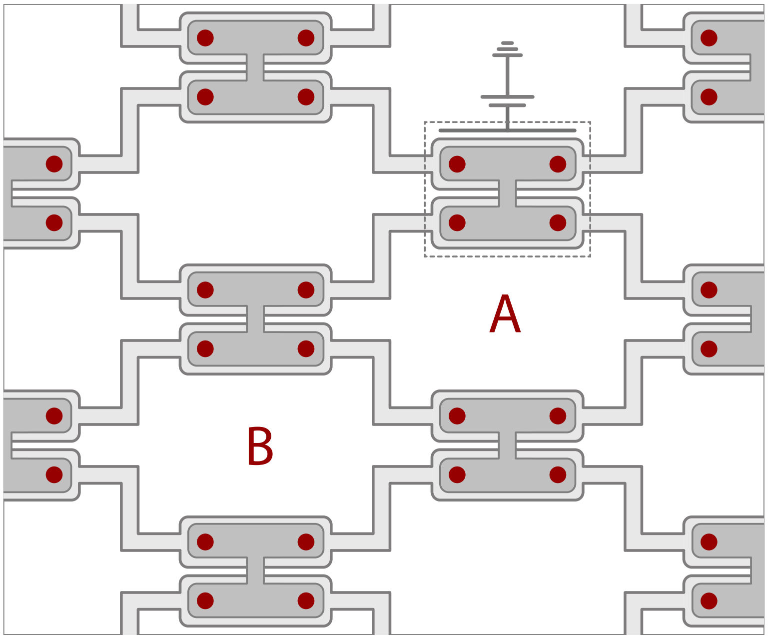

Figure 3.8: Majorana surface code (see Refs. [86, 87, 88]) relying on Majorana box qubits made of two parallel proximitized TI nanoribbons connected by a SC bridge. Each of the boxes is therefore described in terms of its own charging energy, and hosts four MBSs (red dots). Neighboring qubits are tunnel coupled, where the tunneling can be formed by using the TI material itself. In the two-dimensional network structure, stabilizer operators of two types, denoted A and B, are defined as products of eight Majorana operators belonging to MBSs (red dots) going around minimal plaquettes of type A or B as indicated. The figure was taken from our publication Ref. [64].

For the purpose of serving as the building block in a Majorana surface code, we expect that it is convenient to realize the TI based Majorana qubit in a "H"-shaped geometry, see Fig. 3.8. This is achieved by having two parallel, proximitized TI nanoribbons connected by a superconducting bridge. In contrast, in the Sections 3.2 and 3.3, we considered two 1D TSCs aligned on the same axis (see Figs. 3.3 and 3.6). Moreover, the necessary tunneling links to connect MBSs on neighboring boxes (as well as interference links for the interferometric readout) could be realized from the TI material itself. The network fabrication itself is a challenging task that may be achieved using refined

lithographic and wet etching techniques.
The operational principle of the Majorana surface code is founded on the so-called stabilizer operators of which there are two types denoted A and B. These operators are defined as the products of the eight Majorana operators corresponding to the minimal loops of type A and B displayed in Fig. 3.8. The mutually commuting stabilizer operators have eigenvalues ±1, defining the so called physical qubits of the system. All stabilizer operators are now repeatedly measured, hence, projecting the code onto a well-defined highly entangled simultaneous eigenstate of the system. The logical qubits are formed by a few qubits that are not being measured. The access elements for initialization, readout and manipulation can be realized by tunnel conductance probes and charge pumping by means of single-electron transistors [87].

Another perspective for the TI nanoribbon platform is the confirmation of Majorana fusion rules using the protocol of Aasen et al. [39]. It may be possible to apply this protocol to a proximitized TI nanoribbon device as shown in Fig. 3.9. This qubit device is connected on both ends with a bulk superconducting reservoir as described in Subsection 3.3.2. Additionally to the two non-proximitzed constrictions serving for this purpose, the device contains a third narrow TI constriction connecting the two proximitized halves of the nanoribbon as discussed in Section 3.2. As outlined before, the manipulation of the three junctions can be achieved via gates placed at the three constrictions.

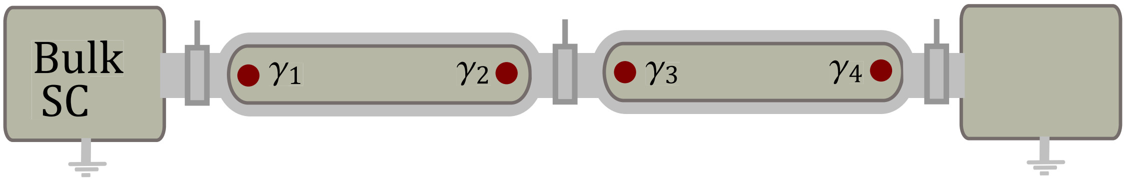

Figure 3.9: The TI nanoribbon qubit device (see Fig. 3.3) is connected with bulk superconducting reservoirs at both ends, as described in Subsection 3.3.2. The three non-proximitized constrictions constitute barriers that can be regulated via gates. Following the protocol of Aasen et. al may make it possible to confirm Majorana fusion rules [39] by reading out the charge on the two floated halves after the necessary steps of the protocol are performed. The time-dependent steps of the protocol involve the lowering and raising of the three barriers in a certain order.

Following the steps of the aforementioned protocol, could make it possible to confirm Majorana fusion rules. At the end of this protocol, the two fusion channels of the Ising anyons manifest themselves in a probabilistic readout of the charge in the two floated halves of the device [39].

Another perspective is that as soon as lithographically defined TI nanoribbons are demonstrated, fabrication efforts could concentrate on T-junction geometries [37] to carry out braiding experiments [39]. In summary, there are multiple exciting directions to pursue once the platform is under experimental control.

Chapter 4

Majorana qubit detection via simultaneous weak measurement of its nonlocal Pauli operators

In this chapter, we introduce a novel weak measurement approach to Majorana qubit detection based on the shot noise of tunneling current probes. We formulate protocols that lie within the scope of present day experimental physics and provide experimentally verifiable, quantitative predictions that allow to test the genuineness of MBSs. The protocols aim at a core property of the Majorana qubit, its nonlocal Pauli algebra, which is closely related to the non-Abelian braiding.

The remainder of this chapter is structured as follows: In Section 4.1, we give an explanation and qualitative discussion of the envisioned experiments. The Sections 4.2 and 4.3 describe the theoretical modeling of the corresponding devices. The phenomenology of the Majorana box qubit is presented in detail in Section 4.4, and to draw a contrast the corresponding signatures for Andreev bound states (ABSs) are discussed in Section 4.5. These results are condensed into experimental protocols that allow for the clear identification of MBSs and Majorana qubits in Section 4.6. Throughout this chapter, we work in units of

$$\hbar = e = k_B = 1. \tag{4.1}$$

Most results presented in this chapter are published in Ref. [89]. The present chapter also contains additional details and results in comparison to the published material, e.g. in Subsections 4.4.2, 4.4.3, 4.4.4 and 4.4.5.

4.1 Experimental setting and qualitative discussion

According to fundamental quantum physics, it is impossible as a matter of principle to simultaneously perform projective measurements of noncommuting observables. Nevertheless, simultaneous measurements are, in fact, possible using weak continuous quantum measurements [90]. It is at the heart of our proposal to study the Majorana box qubit to simultaneously realize continuous weak measurement of its two nonlocal Pauli components σ_1 and σ_2. This approach is illustrated in the schematic of Fig. 4.1 where two tunneling currents I_1 and I_2 are sensitive to σ_1 and σ_2, respectively. For an introduction to weak continuous measurement we refer to Refs. [91, 92, 93]. The simultaneous weak measurement of orthogonal qubit components was previously considered in Refs. [90, 94, 95]. The observables σ_1 and σ_2 cannot be known sharply at the same time. Instead, there is a competing tendency to partially collapse the system state over time. This implies a random diffusion of the density matrix in the Bloch sphere [95]. Furthermore, the information about the initial state of the qubit is lost

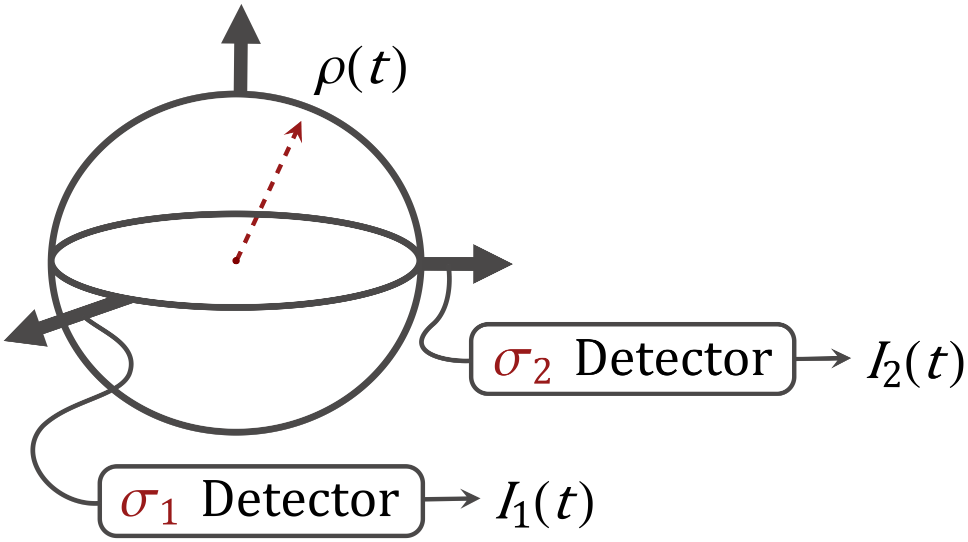

Figure 4.1: Bloch sphere for a qubit described by the density matrix ρ. The variables $I_\alpha(t)$ with $\alpha = 1, 2$ are the outputs of detectors weakly continuously measuring the qubit component σ_α yielding a time continuous noisy signal (e.g. voltage but in the realizations discussed below it is current). The interaction between the qubit and the detectors is assumed to be sufficiently weak so that it takes time to accumulate information and distort the qubit. For the simultaneous monitoring of the noncommuting pseudospin components the different imprecise (weak) readouts are incompatible. This figure was inspired by Ref. [95].

on the timescale of the dephasing rate [94]. However, as we will see the statistics of the detector outcomes encode valuable information about the underlying Pauli algebra. The latter is a unique property of the Majorana qubit, which is alternatively verified by means of a more elaborate braiding protocol.

How can the situation abstractly illustrated in Fig. 4.1 be realized in terms of concrete devices? The experimental setup we propose contains a Coulomb blockaded topological superconductor island with three normal-conducting leads weakly coupled with amplitudes λ_α to different Majorana states, see Fig. 4.2. If the neighboring leads are coupled amongst themselves with weak tunnel links t_0, a two-sided interferometric setting is realized. As discussed in Section 2.2, the effective low-energy tunneling between the leads 0 and 1 is known to be described by the effective Hamiltonian $\tilde{H}_T = (t_0 + t_1(i\gamma_1\gamma_0))\, c_1^\dagger c_0 + \text{H.c.}$ with $c_\alpha = \sum_k c_{\alpha,k}$ the lead fermions [11]. For decoupled lead 2 and applied bias V, the measurement of the tunneling current $I_1(t)$ effectively constitutes a continuous weak measurement of $i\gamma_1\gamma_0$. The latter becomes projective after a time of order $\sim 1/V$. Depending on the eigenstate of $i\gamma_1\gamma_0$ that the system gets

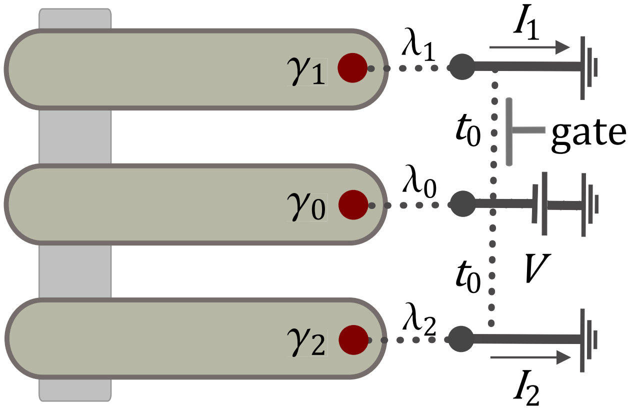

Figure 4.2: Floating Majorana island realized from three parallel Majorana quantum wires (gray-green) connected by a topologically trivial SC backbone (gray). The three Majorana states γ_α localized at the right ends of the wires (red dots) are tunnel coupled to normal-conducting electrodes (thick black lines) with amplitudes λ_α. To realize a two-sided interferometer, direct tunneling links t_0 are installed in between neighboring leads. The central lead ($\alpha = 0$) is operated as a source of electrons by means of an applied bias voltage V driving the currents I_1 and I_2 to ground, which couple to $\sigma_1 = i\gamma_1\gamma_0$ and $\sigma_2 = i\gamma_2\gamma_0$ respectively. The MBSs localized at the left wire ends may or may not be fused into a single Majorana, and are not displayed since they are uncoupled and do not influence the transport.

projected to, one finds two outcomes (in units of $e^2/\hbar$) [11]

$$\langle I_1 \rangle = 2\pi\nu^2 V \left(|t_0|^2 + |t_1|^2 + 2\mathrm{Re}(t_0^* t_1)(i\gamma_1\gamma_0) \right). \tag{4.2}$$

Because of the symmetry of the setting, the same thing can be said about the average current $\langle I_2 \rangle$ if lead 1 is decoupled instead of lead 2. When all three leads are coupled and the bias is applied, the two readouts of the tunneling current $I_{\alpha=1,2}(t)$ are therefore incompatible. No simultaneous eigenstate of $\sigma_1 = i\gamma_1\gamma_0$ and $\sigma_2 = i\gamma_2\gamma_0$ exists and the qubit is conflicted and cannot approach a pure state. Strong Coulomb blockade is a crucial ingredient for this physics, because in a grounded device an electron tunneling into γ_0 would be approximately uncorrelated with an electron tunneling out of the island via γ_1 or γ_2. Our strategy is to look for signatures in the shot noise of the two currents that reflect the continuous monitoring of the nonlocal Pauli operators [25],

$$\sigma_1 = i\gamma_1\gamma_0, \quad \sigma_2 = i\gamma_2\gamma_0, \quad \sigma_3 = i\gamma_2\gamma_1. \tag{4.3}$$

Note that the algebra is not of the Pauli type anymore in the competing case of ABSs, which, as we will show, has profound consequences that allow to distinguish such bound states. The prime observable of interest is the current cross-correlation amplitude,

$$S_{12} = \int_0^t dt \, \langle\langle I_1(t) I_2(0) \rangle\rangle \,, \tag{4.4}$$

where we define the second cumulant in the standard way as $\langle\langle AB \rangle\rangle = \langle AB \rangle - \langle A \rangle \langle B \rangle$. In this chapter, we study the observable S_{12} in the long time limit, both in the presence and absence of interference links (see the vertical dashed lines in Fig. 4.2) connecting the electrodes coupled to the island amongst themselves. The structure defined by these links can be controlled via gate electrodes during an experiment and makes a detailed noise profile of MBSs clearly accessible as we will see. The signatures are qualitatively unique to the fluctuating current for a device with either MBSs or Andreev bound states.

4.1.1 Device geometries

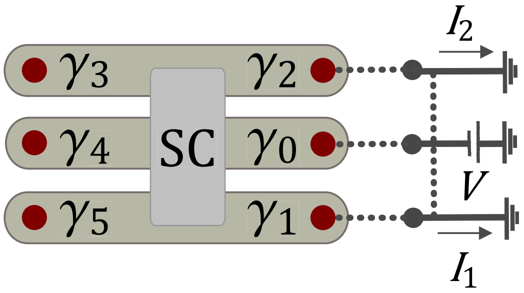

Figure 4.3: The envisioned experiment can be carried out on a wide range of possible device layouts with the hexon geometry [12] being a viable and advantageous option. This system consists of three parallel Majorana wires (gray-green) joined by a trivial SC (gray) to form a single island. Of the six MBSs present in the system, only those localized on the right ends are being addressed by coupled leads (here: γ_0, γ_1 and γ_2). The three MBSs on the other side (here: γ_3, γ_4 and γ_5) are far enough away to be decoupled and irrelevant for the transport. In this geometry as well as in the geometry displayed in Fig. 4.2, it is possible to have sufficiently short interference paths (vertical dashed lines) to maintain phase coherence.

The envisioned effects and experiments can be carried out on a wide range of device geometries as well as different condensed matter platforms that give rise to zero-dimensional MBSs. For concreteness in this chapter, we have the semiconducting wire platform in mind. The geometry displayed in Fig. 4.2 represents a one-sided hexon. The topologically trivial SC backbone connects three parallel SM wires that are driven into the topological phase. The MBSs to the left are either fused into a single uncoupled Majorana or not, but are in any case uncoupled and inconsequential for the physics of interest. Instead, one can also use the hexon geometry, see Fig. 4.3. Of the six Majoranas present in this system, we are only addressing three of them that are localized on one side. Another possible option is to use geometries where only two topological superconducting wires are connected by a trivial superconductor to form a single island. For a genuine Majorana qubit, the charge quantization on such islands implies the parity constraint $\gamma_0\gamma_1\gamma_2\gamma_3 = \pm 1$ [25]. The first example of such a device is shown in Fig. 4.4 where one uses the “tetron” or “Majorana box qubit” geometry [11, 12] discussed in 2.2. The second option displayed in Fig. 4.4 arranges the two SM wires on the same axis connected by a U-shaped s-wave superconducting bridge. This can also be seen as a close relative of the device discussed in Chapter 3. The drawback

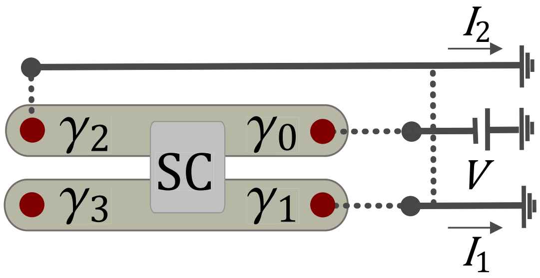

Figure 4.4: The schematic gives another example for a realistic geometry where only two topological superconducting wires (gray-green) are connected by a trivial superconductor (gray) to form a single island, in this case a “tetron” or “Majorana box qubit” [11, 12]. Compared to the geometries based on three parallel Majorana wires forming a single island the displayed geometry has an important drawback: one of the interference links has to transport electrons phase coherently along the entire length of the Majorana wire. It has been proposed to use another Coulomb blockaded Majorana wire to realize a long phase coherent interference link [11].

of the geometries shown in Fig. 4.4 and 4.5 is the fact that one of the interference links has to transport electrons along the entire length of the Majorana wire. The latter have to be of the order of one micrometer for the MBSs to have sufficiently small overlap, which clearly exceeds typical phase coherence lengths of e.g. a semiconductor. It has therefore been proposed, e.g. in Ref. [11], to use another Coulomb blockaded SM wire in the topological phase to realize a sufficiently long phase coherent interference path.

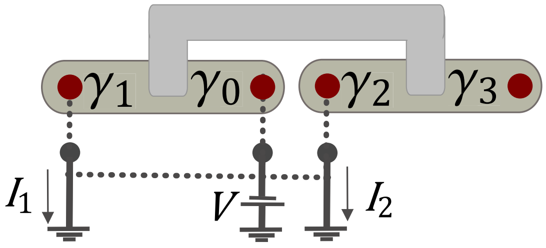

Figure 4.5: The schematic gives a second example for a realistic geometry where only two topological superconducting wires (gray-green) are connected by a trivial superconductor (gray) to form a single island and are positioned on the same axis. One can also think of the qubit geometry based on proximitized TI nanoribbons proposed in Chapter 3. Once again, this geometry makes it necessary to have a reference arm of length of the 1D TSC itself.

4.2 Effective Hamiltonian for the weak measurement settings

In this section we discuss the low-energy effective Hamiltonian description of the three-terminal Majorana devices (see Figs. 4.2, 4.3, 4.4 and 4.5). Assuming the parallel proximitized nanowires are driven into the topological regime by a sufficiently strong magnetic field ($\Gamma > \Gamma_c$), MBSs emerge at the wire terminations. The topological gap $\varDelta$ separating the corresponding (almost) zero energy states and the quasicontinuum of extended states as well as the charging energy E_C shall define much larger energy scales than temperature and the applied bias, i.e.

$$V, T \ll \Delta, E_C. \tag{4.5}$$

The charge conservation on the mesoscopic island implies that the conjugate variables of island electron number N and superconducting phase ϕ are described by operators with commutation relation $[\phi, N] = 2i$. Exponentiation of the phase operator $e^{\pm i\phi/2}$ yields an operator which adds (removes) an electron charge [29]

$$e^{\pm i\phi/2} |N\rangle = |N \pm 1\rangle , \tag{4.6}$$

where $|N\rangle$ is the charge state of the island. Now, consider the field operator Ψ_α which annihilates an electron on the SC close to the nearby lead α. In general, Ψ_α is expanded in terms of all MBSs on the island as well as the Bogoliubov quasiparticles of the SC. However, we are now interested in the low-energy physics where the quasiparticles above the gap are not important. Furthermore, in the considered geometries the MBSs localized near leads $\alpha' \neq \alpha$ have exponentially suppressed amplitudes and do not contribute. Thus, the field operator Ψ_α affords the low-energy representation solely in terms of the N_α MBSs localized close to lead α [29, 30]

$$\Psi_\alpha = \sum_{j=1}^{N_\alpha} \xi^*_{\alpha,j} e^{-i\phi/2} \gamma^j_\alpha + \dots , \tag{4.7}$$

where $\xi^*_{\alpha,j}$ is related to the wavefunction belonging to γ^i_α. This relation encapsulates the break-up of the electron statistics and its charge degree of freedom after it has tunneled into the superconductor. Its fermionic anticommutation relations are maintained within the neutrally charged localized MBSs while its charge is spread over the whole SC island. By inserting the low-energy approximation (4.7) of the electron field operators into the tunneling Hamiltonian $H_{\mathrm{T}} = \sum_k \sum_{\alpha=0}^{2} \tilde{\lambda}_\alpha c^\dagger_{\alpha,k} \Psi_\alpha$+H.c. between the leads and Majorana island [30], we obtain the low-energy tunnel Hamiltonian

$$H_{\mathrm{T}} \simeq \sum_{j=1}^{N_\alpha} \sum_k \sum_{\alpha=0}^{2} \lambda^j_\alpha c^\dagger_{\alpha,k} \gamma^j_\alpha e^{-i\phi/2} + \mathrm{H.c.} \tag{4.8}$$

with $\lambda^i_\alpha \equiv \tilde{\lambda}_\alpha \xi^*_{\alpha,i}$ and $c_{\alpha,k}$ the respective lead fermions. According to (4.8), the zero mode operators γ^i_α are tunnel coupled with amplitude λ^i_α to the respective lead fermions $c_{\alpha,k}$. Such a Hamiltonian is by now standard and has been considered e.g. in the following Refs. [25, 26, 29, 28].

Hence, we model the three-terminal Majorana devices (see Figs. 4.2, 4.3, 4.4 and 4.5) using the Hamiltonian

$$H = H_{\mathrm{Leads}} + H_{\mathrm{T}} + H_C, \tag{4.9}$$

with the charging term

$$H_C = E_c \left(\hat{N} - n_g \right)^2, \tag{4.10}$$

and the backgate parameter n_g. The metallic leads are described by the Hamiltonian H_{Leads} to be specified later. We assume that we are far away from the charge degeneracy point. Throughout this chapter, the charging energy is assumed to be a large energy scale. The significant size of the charging energy scale means that a low-energy electron will be merely virtually present in the island and has to tunnel out again immediately. As discussed in Chapter 2, the MBSs enable a highly nonlocal electron transfer process where an electron tunneling into γ^i_α tunnels out from $\gamma^j_{\alpha'}$ while sustaining phase coherence even when the pair of MBSs is separated by a sizable distance [29]. We expand around the unique charge ground state $|N_0\rangle$ taking into account fluctuations to the next higher charge states $|Q_0 \pm 1\rangle$ with energy of order of the charging energy E_C. Neglecting the frequency dependence of the self-energy, we can write a series expansion of the effective Hamiltonian [96]

$$H_{\mathrm{eff}} = \sum_{n=1}^{\infty} H^{(n)}_{\mathrm{eff}}, \tag{4.11}$$

with the n-th order term

$$H_{\mathrm{eff}}^{(n)} = P_0 H_{\mathrm{T}} \left(\frac{1}{-H_C} H_{\mathrm{T}} \right)^{n-1} P_0. \tag{4.12}$$

Here P_0 is the projection operator onto the charge ground state $|N_0\rangle$. This procedure yields the effective low-energy Hamiltonian (see e.g. Refs. [87, 88] for similar derivations)

$$H_C + H_{\mathrm{T}} \to \tilde{H}_T \equiv H_{\mathrm{eff}}. \tag{4.13}$$

As shown in Appendix B, the leading order contribution to the effective tunneling in our case is given by

$$\tilde{H}_T = \frac{1}{2} \sum_{\alpha \neq \alpha'} \mathcal{O}_{\alpha\alpha'} \sum_{k,k'} c^\dagger_{\alpha,k} c_{\alpha',k'} + \text{H.c.}, \tag{4.14}$$

where the operator $\mathcal{O}_{\alpha\alpha'}$ is a linear combination of Majorana bilinears

$$\mathcal{O}_{\alpha\alpha'} = \sum_{j=1}^{N_\alpha} \sum_{j'=1}^{N_{\alpha'}} t^{jj'}_{1,\alpha\alpha'} (i\gamma^j_\alpha \gamma^{j'}_{\alpha'}). \tag{4.15}$$

Here we have introduced the cotunneling amplitudes

$$t^{jj'}_{1,\alpha\alpha'} \simeq \frac{2i\lambda^j_\alpha (\lambda^{j'}_{\alpha'})^*}{E_C}. \tag{4.16}$$

The next higher terms contributing to the Hamiltonian in the expansion (4.11) are of order $\mathcal{O}\left(E_C^{-2} |\lambda^j_\alpha|^3\right)$ and thus strongly suppressed in the relevant limit of weak tunnelings and large charging energy. We further note that from the definition (4.15) we read off that $t^{jj'}_{1,\alpha\alpha'} = -(t^{jj'}_{1,\alpha'\alpha})^*$ and therefore

$$\mathcal{O}_{\alpha\alpha'} = \mathcal{O}^\dagger_{\alpha'\alpha}. \tag{4.17}$$

This operator will play the role of a jump operator in a quantum master equation later in this chapter.

4.3 Formalism for weak measurement protocols applied to Majorana devices

In this subsection, we describe an efficient formalism to access the signatures of electron transport in the three-terminal Majorana devices introduced in subsection 4.1, see Figs. 4.2, 4.3 and 4.4. To this end we start by introducing some necessary background on the methodology of full counting statistics (FCS). In particular, we derive a variant of the Liouville-von Neumann equation, which is modified by counting fields [27]. Based on this equation as well as on the effective Hamiltonian derived in Subsection 4.2, we go on to derive quantum master equations augmented with counting parameters. Finally, we take a Markovian limit and explicitly state the resulting equation for the conditions of practical importance for us, namely the limit in which temperature is low compared to the applied bias voltage V.

4.3.1 Method of full counting statistics

The experimental scenario introduced in section 4.1 realizes a three-terminal structure. We argued that the crucial information regarding MBS detection is contained in the noise, or more generally the statistics of electron transport. To prepare for the detailed analysis of this statistics, we introduce the necessary elements of the theory of full counting statistics (FCS). For a general M-terminal structure we introduce the probability [97]

$$P_\tau(\mathbf{Q}) \equiv P_\tau(Q_1, \ldots, Q_M) \tag{4.18}$$

that Q_α electrons transfer to terminal $\alpha \in \{1, \ldots, M\}$ during the time interval $[0, \tau]$. Hence, a negative value of Q_α implies that charges have left the terminal α during this time interval. The probability distribution can be written as the Fourier transformation

$$P_\tau(\mathbf{Q}) = \int_{-\pi}^{\pi} \frac{d\chi_1}{2\pi} \cdots \int_{-\pi}^{\pi} \frac{d\chi_M}{2\pi} \mathcal{Z}(\boldsymbol{\chi}, \tau) e^{-i\boldsymbol{\chi}\mathbf{Q}} \tag{4.19}$$

of the characteristic function $\mathcal{Z}(\boldsymbol{\chi}, \tau)$ [27, 98], also called moment generating function, which is the central quantity of interest to us. For the Fourier variables we introduced the shorthand notation $\boldsymbol{\chi} \equiv (\chi_1, \ldots, \chi_M)^T$ with the parameter χ_α counting electrons in lead α. Moreover, we have defined $\boldsymbol{Q} \equiv (Q_1, \ldots, Q_M)^T$. Now let $\rho(t)$ be the density operator of the system which is governed by the Liouville-von Neumann equation [24]

$$\frac{\partial}{\partial t}\rho(t) = -i\left[H, \rho(t)\right], \tag{4.20}$$

where H is the Hamiltonian. Quantum mechanically, the probability $P_\tau(\mathbf{Q})$ can be expressed using the projection postulate which states that $P_\tau(\mathbf{Q}) = \mathrm{Tr}\left(\rho(t)\hat{P}(\mathbf{Q})\right)$, where $\hat{P}_\tau(\mathbf{Q})$ is the projection operator onto the subspace with eigenvalues $\{Q_1, Q_2, \ldots\}$. This can be rewritten in the following way [98]

$$\begin{aligned}
P_\tau(\mathbf{Q}) &= \mathrm{Tr}\left(\rho(t)\sum_{n_1=0}^{\infty}\cdots\sum_{n_M=0}^{\infty}\delta_{n_1 Q_1}\ldots\delta_{n_M Q_M}\hat{P}(\boldsymbol{n})\right) \\
&= \int_{-\pi}^{\pi}\frac{d\chi_1}{2\pi}\cdots\int_{-\pi}^{\pi}\frac{d\chi_M}{2\pi}e^{-i\boldsymbol{\chi}\mathbf{Q}}\mathrm{Tr}\left(\rho(t)\sum_{n_1=0}^{\infty}\cdots\sum_{n_M=0}^{\infty}e^{i\boldsymbol{\chi}\mathbf{n}}\hat{P}(\boldsymbol{n})\right) \\
&= \int_{-\pi}^{\pi}\frac{d\chi_1}{2\pi}\cdots\int_{-\pi}^{\pi}\frac{d\chi_M}{2\pi}e^{-i\boldsymbol{\chi}\mathbf{Q}}\mathrm{Tr}\left(\rho(t)e^{i\boldsymbol{\chi}\hat{\mathbf{Q}}}\right),
\end{aligned} \tag{4.21}$$

with $\boldsymbol{n} \equiv (n_1, \ldots, n_M)^T$. In the third equality we have used the spectral representation $e^{i\boldsymbol{\chi}\hat{\mathbf{Q}}} = \sum_{n_1=0}^{\infty}\cdots\sum_{n_M=0}^{\infty}e^{i\boldsymbol{\chi}\mathbf{n}}\hat{P}(\boldsymbol{n})$. We assume $\rho(t=0) \equiv \rho_0$ to be the initial time density operator describing a state where each terminal α is in a definite charge state $Q_{\alpha,0}$. The operators $\hat{Q}_\alpha$ count the net difference of electrons added and hence satisfy $\hat{Q}_\alpha\rho(0) = 0$. The moment generating function, which is inferred to be $\mathcal{Z}(\boldsymbol{\chi}, t) = \mathrm{Tr}(\rho(t)e^{i\boldsymbol{\chi}\hat{\mathbf{Q}}})$ by comparing (4.21) and (4.19), in this case yields the statistics of transported electrons during the time interval $[0, \tau]$ [99]. We now use the cyclic invariance of the trace, the fact that $\rho(0) = e^{-i\boldsymbol{\chi}\hat{\mathbf{Q}}}\rho(0)$ and $[\hat{Q}_\alpha, \rho(0)] = 0$, to rewrite the moment generating function in a more symmetric form [98]:

$$\begin{aligned}
\mathcal{Z}(\boldsymbol{\chi}, t) &= \mathrm{Tr}\left(U(t)\rho(0)U^\dagger(t)e^{i\boldsymbol{\chi}\hat{\mathbf{Q}}}\right) \\
&= \mathrm{Tr}\left(e^{\frac{i}{2}\boldsymbol{\chi}\hat{\mathbf{Q}}}U(t)e^{-\frac{i}{2}\boldsymbol{\chi}\hat{\mathbf{Q}}}\rho(0)e^{-\frac{i}{2}\boldsymbol{\chi}\hat{\mathbf{Q}}}U^\dagger(t)e^{\frac{i}{2}\boldsymbol{\chi}\hat{\mathbf{Q}}}\right) \\
&\equiv \mathrm{Tr}\left(U_{\boldsymbol{\chi}}(t)\rho(0)U^\dagger_{-\boldsymbol{\chi}}(t)\right).
\end{aligned} \tag{4.22}$$

Here we defined the time evolution operator [27, 98]

$$U_{\boldsymbol{\chi}}(t) \equiv e^{\frac{i}{2}\boldsymbol{\chi}\hat{\mathbf{Q}}}U(t)e^{-\frac{i}{2}\boldsymbol{\chi}\hat{\mathbf{Q}}} = \exp\left(-\frac{i}{\hbar}\int_0^t ds H_{\boldsymbol{\chi}}(s)\right) \tag{4.23}$$

with the Hamiltonian

$$H_{\boldsymbol{\chi}} \equiv e^{\frac{i}{2}\boldsymbol{\chi}\hat{\mathbf{Q}}} H e^{-\frac{i}{2}\boldsymbol{\chi}\hat{\mathbf{Q}}} \tag{4.24}$$

modified by the counting parameters. Note that Eq. (4.22) implies that the forward and backward time evolution is generated by a different Hamiltonian. We also mention in passing that $H_{\boldsymbol{\chi}}$ is Hermitian. We now define a generalized density operator according to

$$\rho(\boldsymbol{\chi}, t) = U_{\boldsymbol{\chi}}(t)\rho(0)U^{\dagger}_{-\boldsymbol{\chi}}(t). \tag{4.25}$$

Unlike for a real density operator its trace is not unity, but in fact yields the moment generating function, i.e. $\mathcal{Z}(\boldsymbol{\chi}, \tau) = \mathrm{Tr}\,(\rho(\boldsymbol{\chi}, \tau))$. Moreover, its time evolution obeys the following modified Liouville-von Neumann equation [27, 98],

$$\frac{\partial}{\partial t}\rho(\boldsymbol{\chi}, t) = -iH_{\boldsymbol{\chi}}\rho(\boldsymbol{\chi}, t) + i\rho(\boldsymbol{\chi}, t)H_{-\boldsymbol{\chi}}. \tag{4.26}$$

The equation is solved with the initial condition $\rho(\boldsymbol{\chi}, 0) = \rho(0)$. The generating function of irreducible moments is given by the logarithm of the moment generating function evaluated at the final time τ after the measurement, $\mathcal{F}(\boldsymbol{\chi}, \tau) = \ln \mathrm{Tr}\,(\rho(\boldsymbol{\chi}, \tau))$. By differentiation with respect to the counting fields all cumulants (irreducible moments) of the charge Q_α in lead $\alpha = 1, 2$ can be obtained via

$$\langle\langle (Q_\alpha)^n \, (Q_{\alpha'})^m \ldots \rangle\rangle = \left(-i\frac{\partial}{\partial \chi_\alpha}\right)^n \left(-i\frac{\partial}{\partial \chi_{\alpha'}}\right)^m \ldots \ln \mathrm{Tr}\,(\rho(\boldsymbol{\chi}, \tau))\bigg|_{\boldsymbol{\chi}=(0,0,\ldots)}. \tag{4.27}$$

The fact that the probability adds to unity $\sum_{\{Q_\alpha\}} P_\tau(\mathbf{Q}) = 1$ implies that $\mathcal{F}(\boldsymbol{\chi} = \mathbf{0}, \tau) = 0$. Moreover, the cumulant generating function generally is 2π periodic in each χ_α [97],

$$\mathcal{F}(\ldots, \chi_\alpha + 2\pi, \ldots, \tau) = \mathcal{F}(\ldots, \chi_\alpha, \ldots, \tau). \tag{4.28}$$

This is related to the fact that the transferred charge physically is an integer multiple of the charge of the electron. The conservation of charge now implies that the moment and the cumulant generating function only depend on counting field differences [97]. More concretely, the difference $\chi_\alpha - \chi_{\alpha'}$ is associated with the charge transfer between the terminals α and α'. Therefore, there is a redundancy in the counting fields $\chi_1, \ldots, \chi_M$ and we may choose a gauge with $\chi_M \equiv 0$ and keep $M - 1$ independent counting fields which we denote by $\boldsymbol{\chi} \equiv (\chi_1, \ldots, \chi_{M-1})$ [97].

4.3.2 Modified Liouville-von Neumann equation

As argued in section 4.1 the correlations of the currents coupled to the Majorana Pauli algebra contain considerably more information than is contained in simple current averages. To formalize this we now draw on our discussion of full counting statistics in the previous subsection 4.3.1 and apply it to our present problem. The setup introduced in subsection 4.1 is a three-terminal structure that can be described using two counting fields $\boldsymbol{\chi} \equiv (\chi_1, \chi_2)$ by setting $\chi_0 \equiv 0$. We want to work with the generalized density matrix governed by the modified Liouville-von Neumann equation in the interaction picture. To this end we split the effective Hamiltonian of the full system including the interference links into two contributions

$$H = H_0 + H_I. \tag{4.29}$$

The unperturbed part is the Hamiltonian,

$$H_0 = \sum_{\alpha=0}^{2} \sum_{k} (\xi_k - V\delta_{\alpha 0}) c^\dagger_{\alpha,k} c_{\alpha,k} \tag{4.30}$$

describing metallic leads and has a continuum of states with dispersion $\xi_k = \frac{k^2}{2m}$. Here m is an effective mass and k the momentum quantum number. The voltage bias V in the central lead $\alpha = 0$ is applied such that it acts as the source of electrons that are transmitted either to the leads $\alpha = 1$ or $\alpha = 2$. The interaction part of the Hamiltonian is given by

$$H_I = H_{\text{ref}} + \tilde{H}_T, \tag{4.31}$$

with $\tilde{H}_T$ as defined in Eq. (4.14) and H_{ref} the interference link Hamiltonian defined as

$$H_{\text{ref}} = \sum_{\alpha=1}^{2} \sum_{k,k'} (t_{0,\alpha} c^\dagger_{\alpha,k} c_{0,k'} + \text{H.c.}). \tag{4.32}$$

Thus, the gate tunable tunnel couplings t_0 introduce a direct link between the source and drain leads. The modified Liouville-von Neumann equation [27] discussed in the previous subsection 4.3.1 now stated for the interaction picture density matrix $\rho_I(\boldsymbol{\chi}, t)$ takes on the form

$$\frac{\partial}{\partial t}\rho_I(\boldsymbol{\chi},t) = -iH_{I,\boldsymbol{\chi}}(t)\rho_I(\boldsymbol{\chi},t) + i\rho_I(\boldsymbol{\chi},t)H_{I,-\boldsymbol{\chi}}(t) \tag{4.33}$$

and is solved with the initial condition $\rho(\boldsymbol{\chi},0) = \rho(0)$. With the time evolution operator $U_0(t) = e^{-itH_0}$ generated by the lead Hamiltonian Eq. (4.30) we define the interaction picture operators

$$H_{I,\boldsymbol{\chi}}(t) = U_0^\dagger(t)H_{I,\boldsymbol{\chi}}U_0(t). \tag{4.34}$$

The Hamiltonian modified with the counting fields (4.24) is given by

$$H_{I,\boldsymbol{\chi}} = \frac{1}{2}\sum_{\alpha\neq\alpha'} e^{\frac{i}{2}(\chi_\alpha-\chi_{\alpha'})}(t_{0,\alpha}\delta_{0\alpha'} + \mathcal{O}_{\alpha\alpha'})\sum_{k,k'} c^\dagger_{\alpha,k}c_{\alpha',k'} + \text{H.c.} \tag{4.35}$$

where the operators $\mathcal{O}_{\alpha\alpha'}$ were defined in Eq. (4.15).

4.3.3 Derivation of the quantum master equation

We use the quantum master equation to study the electronic transport through the weakly coupled mesoscopic Majorana island with Coulomb blockade. In this section, we will provide a detailed weak coupling limit derivation of the Bloch Redfield equation, which we use to model the Majorana devices and from which we obtain the full counting statistics (FCS). The microscopic derivation of quantum master equations in the weak coupling limit is a well established method in the theory of open quantum systems [24, 100]. In this subsection, we will apply this method. In our context, the role of the environment, which will be traced out, is played by the weakly coupled fermionic reservoirs. The starting point is the modified Liouville-von Neumann equation (4.33) from the previous section. We continue to work in the interaction picture and reiterate the equation in its integrated form

$$\tilde{\rho}_{\text{total}}(\boldsymbol{\chi},t) = \tilde{\rho}_{\text{total}}(0) + \int_0^t ds\mathcal{L}_s[\tilde{\rho}_{\text{total}}(\boldsymbol{\chi},s)], \tag{4.36}$$

where $\tilde{\rho}_{\text{total}}$ is the interaction picture density matrix (we omit the index I) of the total system. The total system consists of the Majorana island, the metallic leads and the tunnel couplings between the two. In Eq. (4.36) we have defined a Liouvillesuperoperator by its action on an arbitrary density operator ρ according to

$$\mathcal{L}_t[\rho] := -iH_{I,\boldsymbol{\chi}}(t)\rho + i\rho H_{I,-\boldsymbol{\chi}}(t). \tag{4.37}$$

By plugging this relation into Eq. (4.33) we obtain

$$\frac{\partial}{\partial t}\tilde{\rho}_{\text{total}}(\boldsymbol{\chi}, t) = \mathcal{L}_t[\tilde{\rho}_{\text{total}}(0)] + \int\limits_0^t ds\mathcal{L}_t\left[\mathcal{L}_s[\tilde{\rho}_{\text{total}}(\boldsymbol{\chi}, s)]\right], \tag{4.38}$$

which governs the time evolution of the density operator of the full system $\tilde{\rho}_{\text{total}}(\chi, t)$. We define the generalized reduced density matrix in the low-energy subspace defined by the Majorana operators γ_α^i via the partial trace Tr_L over the fermionic reservoirs

$$\rho(\boldsymbol{\chi}, t) := \text{Tr}_L\left(\tilde{\rho}_{\text{total}}(\boldsymbol{\chi}, t)\right). \tag{4.39}$$

The integro-differential evolution equation obeyed by the reduced density operator reads

$$\frac{\partial}{\partial t}\rho(\boldsymbol{\chi}, t) = \text{Tr}_L\left(\mathcal{L}_t[\tilde{\rho}_{\text{total}}(0)]\right) + \int\limits_0^t ds\text{Tr}_L\left(\mathcal{L}_t\left[\mathcal{L}_s[\tilde{\rho}_{\text{total}}(\boldsymbol{\chi}, s)]\right]\right). \tag{4.40}$$

This exact equation can be treated within the framework of perturbation theory. In the case of weak coupling between the quantum system and the fermionic reservoirs, the Born approximation of a factorized total density matrix

$$\tilde{\rho}_{\text{total}}(\boldsymbol{\chi}, s) = \rho(\boldsymbol{\chi}, s) \otimes \rho_{\text{L}} \tag{4.41}$$

(for $s > 0$) is permissible. This applies to our setting since we envision the reservoirs to be weakly coupled to the mesoscopic superconducting island. The master equation in Born approximation is then given by

$$\frac{\partial}{\partial t}\rho(\boldsymbol{\chi}, t) = \text{Tr}_L\left(\mathcal{L}_t[\rho(0) \otimes \rho_{\text{L}}]\right) + \int\limits_0^t ds\text{Tr}_L\left(\mathcal{L}_t\left[\mathcal{L}_s[\rho(\boldsymbol{\chi}, s) \otimes \rho_{\text{L}}]\right]\right). \tag{4.42}$$

Physically, the Born approximation is well justified if the back action of the system on the fermionic reservoirs is negligible such that the latter effectively remain in the state ρ_{L}. Naively, it may seem a bit contradictory to neglect the back action on the fermionic reservoir, given that we are interested in the changes of particle number in those reservoirs. However, it is valid since Eq. (4.42) does not describe the fermionic reservoirs but the reduced density matrix in the low-energy subspace of the mesoscopic island.

We now apply a Markovian approximation which involves two steps. First, we assume that the density matrix varies on a slower time scale than the typical decay time of the correlation functions of the fermionic leads. This assumption justifies the replacement

$$\rho(\boldsymbol{\chi}, s) \to \rho(\boldsymbol{\chi}, t), \tag{4.43}$$

which makes the master equation time-local. For $\boldsymbol{\chi} = (0, 0)$ the equation preserves Hermiticity as well as unit trace of the density matrix. The coefficients still exhibit a time dependence. Thus, we substitute $s \to t - s$ and extended the time integration to infinity. This is justified by the assumption that the correlation functions of the fermionic reservoirs decay quickly. We arrive at the Markovian master equation

$$\frac{\partial}{\partial t}\rho(\boldsymbol{\chi}, t) = \mathrm{Tr}_L\left(\mathcal{L}_t[\rho(0) \otimes \rho_{\mathrm{L}}]\right) + \int\limits_0^\infty ds \mathrm{Tr}_L\left(\mathcal{L}_t\left[\mathcal{L}_{t-s}[\rho(\boldsymbol{\chi}, t) \otimes \rho_{\mathrm{L}}]\right]\right), \tag{4.44}$$

where according to (4.37) the operator on the right hand side reads

$$\begin{aligned}\mathcal{L}_t\left[\mathcal{L}_{t-s}[\rho]\right] &= H_{I,\boldsymbol{\chi}}(t)\rho H_{I,-\boldsymbol{\chi}}(t-s) + H_{I,\boldsymbol{\chi}}(t-s)\rho H_{I,-\boldsymbol{\chi}}(t) \\ &\quad - H_{I,\boldsymbol{\chi}}(t) H_{I,\boldsymbol{\chi}}(t-s)\rho - \rho H_{I,-\boldsymbol{\chi}}(t-s) H_{I,-\boldsymbol{\chi}}(t).\end{aligned} \tag{4.45}$$

The next step is to trace out the fermionic reservoirs. We approximate the latter to be in thermal equilibrium,

$$\rho_{\mathrm{L}} \sim e^{-\frac{1}{T}H_0} \tag{4.46}$$

with respect to the lead Hamiltonian (4.30) since the coupling due to H_{ref} and $\tilde{H}_T$ is weak. One finds that the following term vanishes, $\mathrm{Tr}_L\left(\mathcal{L}_t[\rho(0) \otimes \rho_{\mathrm{L}}]\right) = 0$. Hence, we arrive at the equation

$$\frac{\partial}{\partial t}\rho(\boldsymbol{\chi}, t) = \int\limits_0^\infty ds \mathrm{Tr}_L\left(\mathcal{L}_t\left[\mathcal{L}_{t-s}[\rho(\boldsymbol{\chi}, t) \otimes \rho_{\mathrm{L}}]\right]\right). \tag{4.47}$$

Using Eq. (4.14), we write the integrand on the right hand side in the following form:

$$\mathrm{Tr}_L\left(\mathcal{L}_t\left[\mathcal{L}_{t-s}[\rho(\boldsymbol{\chi},t)\otimes\rho_{\mathrm{L}}]\right]\right)=\sum_{\alpha=0}^{2}\tilde{\mathcal{L}}_{\alpha,s}\left[\rho(\boldsymbol{\chi},t)\right]. \tag{4.48}$$

With the shorthand notation

$$Q_{\alpha\alpha'}=\sum_{k,k'}c^{\dagger}_{\alpha,k}c_{\alpha',k'} \tag{4.49}$$

the Liouvillians $\tilde{\mathcal{L}}_{\alpha,s}[\rho]$ are given by

$$\begin{aligned}
\tilde{\mathcal{L}}_{0,s}[\rho] \;=\;& \left(e^{i(\chi_2-\chi_1)}\mathcal{O}^{\dagger}_{12}\rho\mathcal{O}_{12}-\mathcal{O}_{12}\mathcal{O}^{\dagger}_{12}\rho\right)\mathrm{Tr}_{\mathrm{L}}\left(\rho_{\mathrm{L}}Q_{12,t}Q^{\dagger}_{12,t-s}\right)\\
&+\left(e^{i(\chi_2-\chi_1)}\mathcal{O}^{\dagger}_{12}\rho\mathcal{O}_{12}-\rho\mathcal{O}_{12}\mathcal{O}^{\dagger}_{12}\right)\mathrm{Tr}_{\mathrm{L}}\left(\rho_{\mathrm{L}}Q_{12,t-s}Q^{\dagger}_{12,t}\right)\\
&+\left(e^{-i(\chi_2-\chi_1)}\mathcal{O}_{12}\rho\mathcal{O}^{\dagger}_{12}-\rho\mathcal{O}^{\dagger}_{12}\mathcal{O}_{12}\right)\mathrm{Tr}_{\mathrm{L}}\left(\rho_{\mathrm{L}}Q^{\dagger}_{12,t-s}Q_{12,t}\right)\\
&+\left(e^{-i(\chi_2-\chi_1)}\mathcal{O}_{12}\rho\mathcal{O}^{\dagger}_{12}-\mathcal{O}^{\dagger}_{12}\mathcal{O}_{12}\rho\right)\mathrm{Tr}_{\mathrm{L}}\left(\rho_{\mathrm{L}}Q^{\dagger}_{12,t}Q_{12,t-s}\right)
\end{aligned} \tag{4.50}$$

and

$$\begin{aligned}
\tilde{\mathcal{L}}_{\alpha=1,2,s}[\rho] \;=\;& t_{0,\alpha}[\mathcal{O}^{\dagger}_{\alpha0},\rho]\mathrm{Tr}_{\mathrm{L}}\left(\rho_{\mathrm{L}}Q_{\alpha0,t-s}Q^{\dagger}_{\alpha0,t}-\rho_{\mathrm{L}}Q^{\dagger}_{\alpha0,t}Q_{\alpha0,t-s}\right)\\
&+t^{*}_{0,\alpha}[\mathcal{O}_{\alpha0},\rho]\mathrm{Tr}_{\mathrm{L}}\left(\rho_{\mathrm{L}}Q^{\dagger}_{\alpha0,t-s}Q_{\alpha0,t}-\rho_{\mathrm{L}}Q_{\alpha0,t}Q^{\dagger}_{\alpha0,t-s}\right)\\
&+\left(e^{-i\chi_\alpha}\mathcal{O}^{\dagger}_{\alpha0}\rho\mathcal{O}_{\alpha0}-\mathcal{O}_{\alpha0}\mathcal{O}^{\dagger}_{\alpha0}\rho\right)\mathrm{Tr}_{\mathrm{L}}\left(\rho_{\mathrm{L}}Q_{\alpha0,t}Q^{\dagger}_{\alpha0,t-s}\right)\\
&+\left(e^{-i\chi_\alpha}\mathcal{O}^{\dagger}_{\alpha0}\rho\mathcal{O}_{\alpha0}-\rho\mathcal{O}_{\alpha0}\mathcal{O}^{\dagger}_{\alpha0}\right)\mathrm{Tr}_{\mathrm{L}}\left(\rho_{\mathrm{L}}Q_{\alpha0,t-s}Q^{\dagger}_{\alpha0,t}\right)\\
&+\left(e^{i\chi_\alpha}\mathcal{O}_{\alpha0}\rho\mathcal{O}^{\dagger}_{\alpha0}-\rho\mathcal{O}^{\dagger}_{\alpha0}\mathcal{O}_{\alpha0}\right)\mathrm{Tr}_{\mathrm{L}}\left(\rho_{\mathrm{L}}\mathcal{O}^{\dagger}_{\alpha0,t-s}Q_{\alpha0,t}\right)\\
&+\left(e^{i\chi_\alpha}\mathcal{O}_{\alpha0}\rho\mathcal{O}^{\dagger}_{\alpha0}-\mathcal{O}^{\dagger}_{\alpha0}\mathcal{O}_{\alpha0}\rho\right)\mathrm{Tr}_{\mathrm{L}}\left(\rho_{\mathrm{L}}\mathcal{O}^{\dagger}_{\alpha0,t}Q_{\alpha0,t-s}\right)\\
&+(e^{-i\chi_\alpha}-1)\left[t^{*}_{0,\alpha}\rho\mathcal{O}_{\alpha0}+t_{0,\alpha}\mathcal{O}^{\dagger}_{\alpha0}\rho+|t_{0,\alpha}|^2\rho\right]\\
&\qquad\times\mathrm{Tr}_{\mathrm{L}}\left(\rho_{\mathrm{L}}Q_{\alpha0,t-s}Q^{\dagger}_{\alpha0,t}+\rho_{\mathrm{L}}Q_{\alpha0,t}Q^{\dagger}_{\alpha0,t-s}\right)\\
&+(e^{i\chi_\alpha}-1)\left[t^{*}_{0,\alpha}\mathcal{O}_{\alpha0}\rho+t_{0,\alpha}\rho\mathcal{O}^{\dagger}_{\alpha0}+|t_{0,\alpha}|^2\rho\right]\\
&\qquad\times\mathrm{Tr}_{\mathrm{L}}\left(\rho_{\mathrm{L}}Q^{\dagger}_{\alpha0,t}Q_{\alpha0,t-s}+\rho_{\mathrm{L}}Q^{\dagger}_{\alpha0,t-s}Q_{\alpha0,t}\right).
\end{aligned} \tag{4.51}$$

Furthermore, we make the assumption that the bandwidth of the reservoirs $\mathit{\Lambda}$ is large compared to the energy scales V and T. Exemplarily, this yields relations that can be obtained by standard techniques [101] like e.g.

$$\int_0^\infty ds \left\langle Q^\dagger_{\alpha 0,t-s} Q_{\alpha 0,t} - Q_{\alpha 0,t} Q^\dagger_{\alpha 0,t-s} \right\rangle = \nu^2 (i\Lambda + \pi V), \tag{4.52}$$

where Λ is the bandwidth of the leads and ν the density of states and $\langle \ldots \rangle \equiv \mathrm{Tr}_\mathrm{L}\left(\rho_\mathrm{L} \ldots\right)$. Analogously, we obtain, for instance,

$$\int_0^\infty ds \left\langle Q_{\alpha 0,t-s} Q^\dagger_{\alpha 0,t} + Q_{\alpha 0,t} Q^\dagger_{\alpha 0,t-s} \right\rangle = 2\pi \nu^2 V n_B(V), \tag{4.53}$$

where $n_B(V)$ is the Bose function which is negligible in the limit $T \ll V$. The terminals $\alpha = 1, 2$ are at the same potential such that thermal cotunneling processes are relevant here,

$$\int_0^\infty ds \left\langle Q_{12,t-s} Q^\dagger_{12,t} + Q_{12,t} Q^\dagger_{12,t-s} \right\rangle = 2\pi \nu^2 T. \tag{4.54}$$

Further technical details concerning the tracing out of the leads are found in Appendix C. We now go on to discuss the master equation, which emerges from the outlined procedure in the next subsection.

4.3.4 Resulting quantum master equation for weak measurement setup

The resulting quantum master equation is a Lindblad equation modified with counting parameters. It is valid for arbitrary number of Majoranas N_α coupled to reservoir α. The equation governs the time evolution of the reduced density matrix ρ_t in the Hilbert space corresponding to the Majorana operators γ_α^i. Without the assumption $T \ll V$, it reads

$$\begin{aligned}\frac{\partial}{\partial t}\rho_t &= -i[\widetilde{H}_q, \rho_t] + 2\pi\nu^2 V \sum_{\alpha=1}^{2}(e^{i\chi_\alpha} - 1)\left(t_{0,\alpha}^* \mathcal{O}_{\alpha 0}\rho_t + t_{0,\alpha}\rho_t \mathcal{O}_{\alpha 0}^\dagger + |t_{0,\alpha}|^2 \rho_t\right) \\ &\quad + 2\pi\nu^2 T\left(\mathcal{D}_{12}(\rho_t) + \mathcal{D}_{21}(\rho_t)\right) + 2\pi\nu^2 V n_B(V)\sum_{\alpha=1}^{2}\mathcal{D}_{0\alpha}(\rho_t) \\ &\quad + 2\pi\nu^2 V(1 + n_B(V))\sum_{\alpha=1}^{2}\mathcal{D}_{\alpha 0}(\rho_t). \end{aligned} \tag{4.55}$$

Here we have defined the superoperator

$$\mathcal{D}_{\alpha\alpha'}(\rho) \equiv e^{i(\chi_\alpha - \chi_{\alpha'})}\mathcal{O}_{\alpha\alpha'}\rho\mathcal{O}_{\alpha\alpha'}^\dagger - \frac{1}{2}\{\mathcal{O}_{\alpha\alpha'}^\dagger \mathcal{O}_{\alpha\alpha'}, \rho\}. \tag{4.56}$$

The jump operator $\mathcal{O}_{\alpha\alpha'}$ is again defined as

$$\mathcal{O}_{\alpha\alpha'} = \sum_{j=1}^{N_\alpha}\sum_{j'=1}^{N_{\alpha'}} t_{1,\alpha\alpha'}^{jj'}(i\gamma_\alpha^j \gamma_{\alpha'}^{j'}), \tag{4.57}$$

and describes the tunneling of an electron from the terminal α' to α. The coherent part of the evolution in Eq. (4.55) is described by a Hamiltonian $\widetilde{H}_q$ which we will specify below in the limit $T \ll V$.

Throughout this chapter, we mostly focus on the low temperature limit $T \ll V \ll \Lambda$, with Λ the lead bandwidth. In this limit, the Bloch Redfield equation (4.55) takes on the form

$$\begin{aligned}\frac{\partial}{\partial t}\rho_t &= -i[H_q, \rho_t] + 2\pi\nu^2 V \sum_{\alpha=1}^{2}(e^{i\chi_\alpha} - 1)\left(t_{0,\alpha}^* \mathcal{O}_{\alpha 0}\rho_t + t_{0,\alpha}\rho_t \mathcal{O}_{\alpha 0}^\dagger + |t_{0,\alpha}|^2 \rho_t\right) \\ &\quad + 2\pi\nu^2 T\left(\mathcal{D}_{12}(\rho_t) + \mathcal{D}_{21}(\rho_t)\right) + 2\pi\nu^2 V \sum_{\alpha=1}^{2}\mathcal{D}_{\alpha 0}(\rho_t), \end{aligned} \tag{4.58}$$

where the Hamiltonian part of the dynamics in the limit $V \ll \Lambda$ (see Appendix C) is generated by

$$\begin{aligned} H_q &= -\Lambda\nu^2 \sum_{\alpha=1}^{2} \left(t^*_{0,\alpha}\mathcal{O}_{\alpha 0} + \text{H.c.}\right) - \frac{\nu^2\Lambda}{2}\sum_{\alpha<\beta}\{\mathcal{O}^\dagger_{\alpha\beta}, \mathcal{O}_{\alpha\beta}\} \\ &\quad + \nu^2 V \ln(\Lambda/2V)\sum_{\alpha=1}^{2}[\mathcal{O}_{\alpha 0}, \mathcal{O}^\dagger_{\alpha 0}]. \end{aligned} \tag{4.59}$$

The Eq. (4.58) is of the Lindblad form but modified with counting parameters. The equation is time-local and for zero counting parameters it preserves Hermiticity and unit trace. Similar equations have been studied in Refs. [94, 102, 103]. We are interested in obtaining the statistics of charge transported during the time interval $t \in [0, \tau]$. To this end, we solve (4.58) with the initial condition $\rho(\chi, 0) = \rho_0$ and obtain the generating function of the charge variables [27, 98] by performing the trace in the reduced generalized qubit space $\mathcal{Z}(\boldsymbol{\chi}, \tau) = \text{Tr}_q\left(\rho_\tau(\chi_1, \chi_2)\right)$. The equation is valid in the weak coupling limit defined by $\nu t_{0,\alpha}, \nu t^{jj'}_{1,\alpha\alpha'} \ll 1$. Its Markovian property implies that we are neglecting memory effects.

4.4 Phenomenology of the Majorana box qubit

In this section, we present the resulting weak measurement phenomenology of the Majorana box qubit. We start by providing instructive details on the derivation of the generating function in Subsection 4.4.1. In Subsection 4.4.2, we analyze the obtained current statistics and describe a remarkable effect of strong current cross-correlations. We present results on the effects of finite temperature in Subsection 4.4.3 and then go on to study the outcome distribution and the statistics of rare current outcomes in Subsection 4.4.4. Finally, we consider finite hybridizations of MBSs on the box qubit in Subsection 4.4.5.

This entire section is founded on the evolution equation for genuine MBSs governing the time evolution of the qubit density matrix $\rho_t \equiv \rho_t(\chi_1, \chi_2)$. To obtain the equation, we have to set $\mathcal{O}_{\alpha\alpha'} = t_{1,\alpha\alpha'}(i\gamma_\alpha\gamma_{\alpha'})$ in Eq. (4.58). Where possible, we use the simplified notation $t_{0,\alpha} = t_0$ and $t_{1,\alpha\alpha'} = t_1$ throughout this chapter. The resulting equation reads

$$\begin{aligned} \frac{\partial}{\partial t}\rho_t &= -i[\tilde{H}_q, \rho_t] + \sum_{\alpha>\alpha'} \frac{\mathit{\Gamma}_{\alpha\alpha'}}{2} \left(z_{\alpha\alpha'}(i\gamma_\alpha\gamma_{\alpha'})\rho_t(i\gamma_\alpha\gamma_{\alpha'}) - \rho_t\right) \\ &\quad + 2\pi V \sum_{\alpha=1}^{2} (e^{i\chi_\alpha} - 1)\left(t_0^* t_1 (i\gamma_\alpha\gamma_0)\rho_t + t_0 t_1^* \rho_t (i\gamma_\alpha\gamma_0)\right) \end{aligned} \tag{4.60}$$

with the rates defined as $\mathit{\Gamma}_{\alpha 0} = 4\pi V \nu^2 |t_1|^2$, $\mathit{\Gamma}_{21} = 4\pi\nu^2 T |t_1|^2$ and with $z_{\alpha 0} = e^{i\chi_\alpha}$, $z_{21} = 2\cos(\chi_1 - \chi_2)$. The Hamiltonian evolution is generated by

$$\tilde{H}_q = -2\nu^2(\Lambda \mathrm{Re}(t_0^* t_1) + \pi V \mathrm{Im}(t_0^* t_1)) \sum_{\alpha=1}^{2} (i\gamma_\alpha\gamma_0). \tag{4.61}$$

Notice that the splitting (4.61) of the qubit energy is due to the presence of the interference paths. The splitting term leads to precession physics and will play an important role for the counting statistics.

4.4.1 Derivation of the generating function for the Majorana qubit

To solve the evolution equation (4.60) and derive the generating function, we reparametrize the time variable, $\rho_t = e^{\theta t}\tilde{\rho}_t$, with

$$\begin{aligned} \theta &= 2\pi\nu^2(|t_0|^2 + |t_1|^2)V\sum_{\alpha=1}^{2}(e^{i\chi_\alpha} - 1) \\ &\quad +4\pi\nu^2|t_1|^2 T(\cos(\chi_1 - \chi_2) - 1). \end{aligned} \tag{4.62}$$

Furthermore, we define the rates as $\tilde{\varGamma}_{\alpha 0} = 4\pi V\nu^2|t_1|^2 e^{i\chi_\alpha}$ and $\tilde{\varGamma}_{21} = 8\pi\nu^2 T|t_1|^2\cos(\chi_1 - \chi_2)$. To solve the Bloch Redfield equation, we parametrize the density matrix as

$$\rho_t = \sum_{\mu=0}^{3}\rho_{\mu,t}\sigma_\mu. \tag{4.63}$$

Thus, we obtain a first order system of four coupled equations for $\tilde{\rho}$ given by

$$\frac{\partial}{\partial t}\tilde{\rho}_{\mu,t}(\chi_1,\chi_2) = \sum_{\mu=0}^{3}\Omega_{\mu\nu}\tilde{\rho}_{\nu,t}(\chi_1,\chi_2). \tag{4.64}$$

The matrix Ω of coefficients reads

$$\Omega = \begin{pmatrix} 0 & a_1 & a_2 & 0 \\ a_1 & -\tilde{\varGamma}_{20} - \tilde{\varGamma}_{21} & 0 & h_2 \\ a_2 & 0 & -\tilde{\varGamma}_{10} - \tilde{\varGamma}_{21} & -h_1 \\ 0 & -h_2 & h_1 & -\tilde{\varGamma}_{10} - \tilde{\varGamma}_{20} \end{pmatrix} \tag{4.65}$$

with

$$a_\alpha = 4\pi V\nu^2 \mathrm{Re}(t_0^* t_1)(z_\alpha - 1), \tag{4.66}$$

$$h_\alpha = -4\nu^2\Lambda \mathrm{Re}(t_0^* t_1) - 4\pi\nu^2 V \mathrm{Im}(t_0^* t_1)e^{i\chi_\alpha}. \tag{4.67}$$

The Eq. (4.60) is solved with the initial condition $\rho(\chi, 0) = \rho_0$ where ρ_0 is the initial reduced density matrix of the qubit [27, 94, 98]. Moreover, we assume the counting fields χ_1 and χ_2 to be constant in the time interval $(0,\tau)$ of measurement. The solution is given by a matrix exponential

$$\rho_{\mu,\tau}(\chi_1,\chi_2) = e^{\theta\tau}\sum_{\nu=0}^{3}\exp(\tau\Omega)_{\mu\nu}\rho_{\nu,0}, \tag{4.68}$$

where ρ_0 is the initial reduced density matrix of the qubit and thus in particular $\rho_{0,0} = \frac{1}{2}$. We obtain the statistics of the currents by considering the logarithm of the generating function

$$\ln \mathcal{Z}(\boldsymbol{\chi},\tau) \equiv \ln \mathrm{Tr}_q\left(\rho_\tau(\chi_1,\chi_2)\right). \tag{4.69}$$

In the long time limit $\mathit{\Gamma}\tau \gg 1$ the cumulant generating function reads

$$\ln \mathcal{Z}(\boldsymbol{\chi}) = \tau\theta(\chi_1,\chi_2) + \tau\lambda_0(\chi_1,\chi_2). \tag{4.70}$$

Here θ is defined as in (4.62) and $\lambda_0(\chi_1,\chi_2)$ is the (unique) solution of the characteristic polynomial of Ω

$$\lambda^4 + c_1(\boldsymbol{\chi})\lambda^3 + c_2(\boldsymbol{\chi})\lambda^2 + c_3(\boldsymbol{\chi})\lambda + c_4(\boldsymbol{\chi}) = 0, \tag{4.71}$$

which satisfies

$$\lambda_0(0,0) = 0. \tag{4.72}$$

Here the $c_i(\boldsymbol{\chi})$ are counting parameter dependent coefficients. Such a solution always exists because $c_4(\chi_1 = 0, \chi_2 = 0) = 0$. The other eigenvalues $\lambda_{i=1,2,3}$ of Ω have a negative real part at $(\chi_1,\chi_2) = (0,0)$. In the limit $T \ll V \ll \mathit{\Lambda}$, we expand Eq. (4.70) to first order in V to obtain the counting statistics. This results in the cumulant generating function

$$\ln \mathrm{Tr}\rho_\tau(\chi_1,\chi_2) = \frac{\Gamma\tau}{2}\left(\frac{2|t_0|^2+|t_1|^2}{|t_1|^2}z - 1 + \sqrt{(z+1)^2 + \frac{8\left[\mathrm{Re}(t_0^* t_1)\right]^2}{|t_1|^4}z^2}\right) \tag{4.73}$$

with

$$z \equiv \frac{1}{2}e^{i\chi_1} + \frac{1}{2}e^{i\chi_2} - 1. \tag{4.74}$$

The two physical observables can now be obtained by taking derivatives according to Eq. (4.27). E.g. the current $\alpha = 1, 2$ is calculated via

$$\langle I_\alpha \rangle = -i\tau^{-1} \frac{\partial}{\partial \chi_\alpha} \ln \mathrm{Tr}_q \left(\rho_\tau(\chi_1, \chi_2) \right) \Big|_{(\chi_1,\chi_2)=(0,0)} . \tag{4.75}$$

The cross-correlations are obtained by means of the relation

$$S_{12} = -\, \tau^{-1} \frac{\partial^2}{\partial \chi_1 \partial \chi_2} \ln \mathrm{Tr}_q \left(\rho_\tau(\chi_1, \chi_2) \right) \Big|_{(\chi_1,\chi_2)=(0,0)} . \tag{4.76}$$

4.4.2 Pronounced shot noise cross-correlations and qubit evolution

In this subsection, we present the results for the shot noise as well as the evolution of the Majorana qubit density matrix. In particular, we discuss below that positive cross-correlations $S_{12} = F \langle I \rangle$ with a Fano factor $F = \mathcal{O}(1)$ characterize the Majorana system in the limit of low temperature $T \ll V$ and weak tunnel couplings. First, however, it is insightful to take a closer look at the dynamics of the qubit density matrix in the absence of the counting parameters. Completely independent of the initial qubit state, the qubit density matrix ρ_t approaches the maximally mixed state

$$\rho_{t \gg \Gamma^{-1}} \simeq \frac{1}{2} \sigma_0 \tag{4.77}$$

on the time scale Γ^{-1} with $\Gamma \equiv 4\pi\nu^2 |t_1|^2 V$. We take note that this time scale is set by voltage and the dimensionless conductance contribution due to cotunneling. The associated loss of quantum information regarding the qubit state is reflected in the averages of the currents passing through the outer barriers as well. In fact, on time scales larger than Γ^{-1}, these averages (in units of $e^2/\hbar$)

$$\langle I_\alpha \rangle = \langle I \rangle \equiv 2\pi\nu^2 V (|t_0|^2 + |t_1|^2) \tag{4.78}$$

do not depend on the qubit state anymore. This is a striking feature since it is in sharp contrast to the individual readout of a single current I_α (see Eq. (4.2)), which couples to the parity $i\gamma_\alpha\gamma_0$ [11] if the other drain terminal is completely decoupled. Nevertheless, it is expected for the simultaneous measurement of noncommuting operators that the quantum information of the initial state of the qubit gets wiped out. Now we turn our attention to the study of the second cumulant $S_{\alpha\alpha'} = \int_0^t dt \, \langle\langle I_\alpha(t) I_{\alpha'}(0)\rangle\rangle$ for $\alpha, \alpha' \in \{1,2\}$ and $\langle\langle AB\rangle\rangle = \langle AB\rangle - \langle A\rangle \langle B\rangle$, in the long time limit $\Gamma\tau \gg 1$, and under the assumption $T \ll V \ll \varLambda$. The shot noise in the current signals $\alpha = 1, 2$ can then be derived to be

$$S_{\alpha\alpha} = \langle I_\alpha\rangle + \frac{4\pi V \nu^2 \left[\mathrm{Re}(t_0^* t_1)\right]^2}{|t_1|^2}. \tag{4.79}$$

The first term is the standard Schottky contribution with $\langle I_\alpha\rangle \equiv 2\pi\nu^2 V(|t_0|^2 + |t_1|^2)$ being the average current as discussed above. The second term shows that the noise level is enhanced whenever the currents I_1 and I_2 couple to the underlying Pauli algebra, because $\mathrm{Re}(t_0^* t_1) \neq 0$ is precisely the condition for Pauli dependent current averages, see Eq. (4.2). The most noteworthy observable signature is the current cross-correlation amplitude S_{12}, which is given by

$$S_{12} = \frac{4\pi V \nu^2 \left[\mathrm{Re}(t_0^* t_1)\right]^2}{|t_1|^2}. \tag{4.80}$$

We point out that this result is derived under the assumption that $t_1 \neq 0$[1]. We may conveniently reexpress Eq. (4.80) by defining the Fano factor F which characterizes the correlations via the relation

$$S_{12} = F \langle I\rangle, \tag{4.81}$$

with $\bar{I}$ as given in (4.78). The corresponding Fano factor again for $T \ll V$ is then given by

$$F = \frac{2\left[\mathrm{Re}(t_0^* t_1)\right]^2}{|t_1|^2 \left(|t_0|^2 + |t_1|^2\right)} = \mathcal{O}(1). \tag{4.82}$$

This result is interesting for a multitude of reasons, one of them being that the currents are positively correlated. The most important aspect of this result, however, is the largeness of the shot noise correlations, $F = \mathcal{O}(1)$. To appreciate this point, it is instructive to draw the contrast with noninteracting electrons in a T-shaped junction [104]. In this case, negative correlations are observed due to processes involving two electrons and the Fano factor is parametrically suppressed in the dimensionless tunnel conductances[2]. This makes it clear that rather different physical mechanisms

---

[1] The maximally mixed state $\frac{1}{2}\sigma_0$ is reached after the timescale Γ^{-1}. Hence, for $t_1 = 0$ this state is never reached and the contribution (4.80) does not arise.

[2] Consider e.g. three leads with a central lead $\alpha = 0$ and drain leads $\alpha = 1, 2$ tunnel coupled

must be active to give rise to the striking result (4.82). Indeed, the competing weak measurements of the Pauli operators $\sigma_1 = i\gamma_1\gamma_0$ and $\sigma_2 = i\gamma_2\gamma_0$ cause a frustration in the system. The large positive cross-correlations in the two incompatible currents I_1 and I_2 coupled to the underlying Pauli algebra are the observable consequence of this frustration. Consistent with this interpretation is the fact that the cross-correlation contribution (4.82) vanishes only for $\mathrm{Re}(t_0^* t_1) = 0$, in which case the currents do not measure the Pauli operators on average. Since $\mathrm{Re}(t_0^* t_1) = 0$ implies a considerable amount of fine tuning generically one will observe $F(V \gg T) = \mathcal{O}(1)$. The fact that in the absence of the reference links, $t_0 = 0$, the Fano factor is parametrically suppressed, i.e. $F \ll 1$, will turn out to be useful for the formulation of measurement protocols. A complementary physical interpretation of (4.82) is that an electron incoming from the source which contributes to I_1 helps to project $i\gamma_1\gamma_0$ onto a definite state. This, in turn, introduces more uncertainty in the expectation value of $i\gamma_2\gamma_0$ and, therefore, affects the current I_2. This physical picture conveys how an electron can exert influence on a subsequent electron that might be incoming much later.

---

according to $H_{\mathrm{ref}} = \sum_{\alpha=1}^{2} \sum_{k,k'} (t_0 c_{\alpha,k}^\dagger c_{0,k'} + \mathrm{H.c.})$. With a bias V applied to operate lead 0 as source, the average current is given by $\langle I_\alpha \rangle = 2\pi\nu_\alpha\nu_0|t_0|^2 V$ with $\alpha = 1, 2$. In a symmetric situation where each lead has the density of states ν, the cross-correlations are given by $F_{\mathrm{non-interacting}} = -\nu^2|t_0|^2$ [104] and thus $|F_{\mathrm{non-interacting}}| \ll 1$. The minus sign is a result of the fact that a single electron is either transmitted to lead 1 or 2.

4.4.3 The effects of finite temperature

For the most part of this chapter we neglect finite temperature contributions assuming that temperature is much smaller than the applied bias. For completeness, we now take a look at corrections due to a small[3] finite temperature $T \lesssim V$ in the all-important result (4.82) for the Fano factor F. As before, we still assume $V, T \ll E_C, \Delta$. Physically, the corrections originate in direct cotunneling processes back and fourth from the two drain terminals 1 to 2 with the amplitude $t_{1,12}$. For clarity, we distinguish this parameter from the cotunneling amplitudes from the source to the drains, which we again assume to be equal, $t_{1,10} = t_{1,20}$. The finite temperature corrected current shot noise (4.79) is given by

$$S_{\alpha\alpha} = \langle I_\alpha \rangle + 4\pi\nu^2 |t_{1,12}|^2 T + \frac{4\pi V^2 \nu^2 \left[\mathrm{Re}(t_0^* t_{1,10})\right]^2}{V|t_{1,10}|^2 + 2T|t_{1,12}|^2}. \tag{4.83}$$

The current cross-correlation formula in the long time limit is given as a sum of two contributions

$$S_{12} = -4\pi\nu^2 |t_{1,12}|^2 T + \frac{4\pi V^2 \nu^2 \left[\mathrm{Re}(t_0^* t_{1,10})\right]^2}{V|t_{1,10}|^2 + 2T|t_{1,12}|^2}. \tag{4.84}$$

The first term is negative and proportional to the temperature T. This term originates in the above mentioned processes where electrons thermally cotunnel via the Majorana states on the box from lead 1 to lead 2 or vice versa. The second term can be identified with the finite temperature version of the formula (4.82). It shows that finite temperature has the effect of weakening the positive $F = \mathcal{O}(1)$ Fano factor, but confirms that in the regime of interest $T \ll V$ the positive second term in Eq. (4.84) is the dominant contribution and results in pronounced positive cross-correlations.

---

[3] To be precise we keep terms linear in temperature in the Bloch Redfield equation, but approximate $\coth(V/2T) \simeq 1$.

4.4.4 Outcome distribution and extreme value statistics

In this section we examine the joint probability distribution $P(I_1, I_2)$ of the current outcomes. In particular, we address the statistics of extreme values and show that there are large fluctuations in the currents. Furthermore, we will plot the joint distribution for several parameters. The probability for the current values (I_1, I_2) is given as the Fourier transformation of the generating function

$$P(I_1, I_2) = \int_{-\pi}^{\pi} \frac{d\chi_1}{2\pi} \int_{-\pi}^{\pi} \frac{d\chi_2}{2\pi} \mathrm{Tr}_q\left(\rho_\tau(\chi_1, \chi_2)\right) e^{-i(\chi_1 I_1 + \chi_2 I_2)\tau}. \tag{4.85}$$

In the limit of a measurement duration $\tau \gg \mathit{\Gamma}^{-1}$, where again $\Gamma \equiv 4\pi\nu^2 |t_1|^2 V$, we can make a saddle point approximation and write the logarithm of the probability distribution in the form [89]

$$\frac{\ln P(I_1, I_2)}{\Gamma\tau} \simeq \min_{\{\mu_\alpha\}} \left[\frac{\ln \mathrm{Tr}_q\left(\rho_\tau(i\mu_1, i\mu_2)\right)}{\Gamma\tau} + \frac{1}{2}\left(|t_0/t_1|^2 + 1\right) \sum_{\alpha=1}^{2} \mu_\alpha (I_\alpha/\bar{I}) \right]. \tag{4.86}$$

According to (4.73), we here have

$$\begin{aligned} \frac{\ln \mathrm{Tr}_q\left(\rho_\tau(i\mu_1, i\mu_2)\right)}{\Gamma\tau} \quad = \quad & \frac{1}{4}\sqrt{(e^{-\mu_1} + e^{-\mu_2})^2 + \frac{8\left[\mathrm{Re}(t_0^* t_1)\right]^2}{|t_1|^4}(e^{-\mu_1} + e^{-\mu_2} - 2)^2} \\ & + \frac{1}{2}\left(|t_0/t_1|^2 + \frac{1}{2}\right)(e^{-\mu_1} + e^{-\mu_2}) - \left(|t_0/t_1|^2 + 1\right). \end{aligned} \tag{4.87}$$

For simplicity of discussion, we again choose system parameters such that I_1 and I_2 have the same average value $\bar{I} = 2\pi\nu^2 V(|t_0|^2 + |t_1|^2)$ for long times $\mathit{\Gamma}\tau \gg 1$. According to the relation (4.86), the probability distribution is found by minimization. For atypically large current outcomes $I_\alpha \gg \bar{I}$, this minimization can be done analytically. In fact, the minimum is located at $\mu_\alpha \simeq \ln\left(\bar{I}/I_\alpha\right)$ and as a result, the probability for these rare events is given by [89]

$$P(I_1, I_2) \overset{I_\alpha \gg \bar{I}}{\simeq} \prod_{\alpha=1}^{2} \left(\frac{\bar{I}}{I_\alpha}\right)^{I_\alpha \tau}. \tag{4.88}$$

We thus see that that there are large fluctuations and rare events occur more often than a Gaussian model would predict. The formula (4.88) derived under the assumption

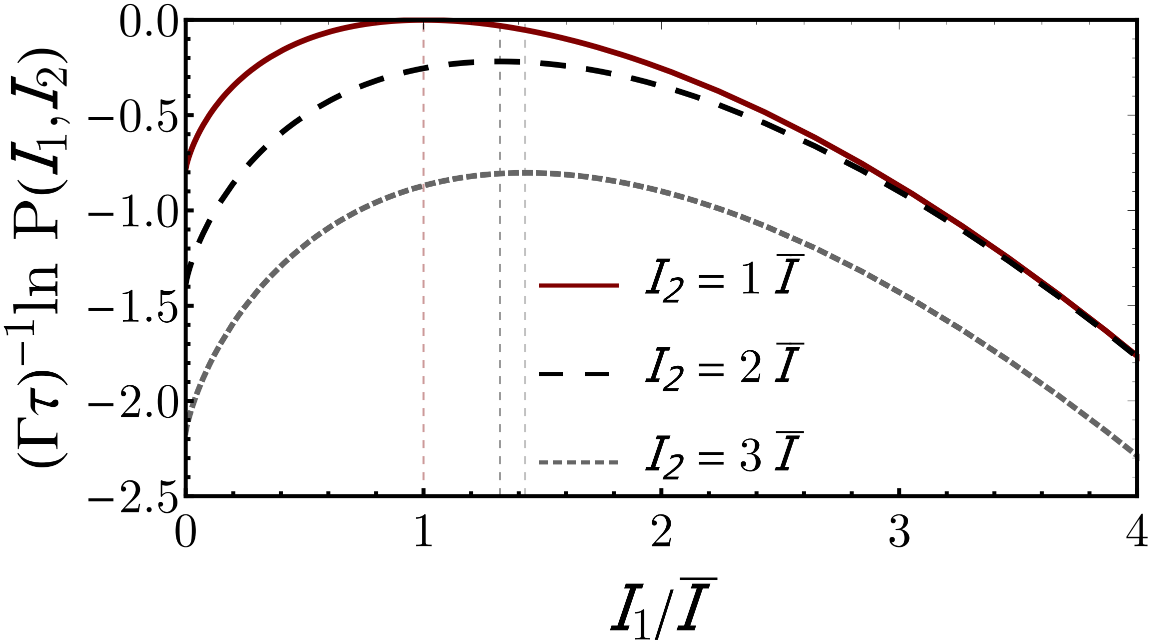

Figure 4.6: Logarithm of the outcome distribution for the Majorana box qubit in the long time limit $\Gamma\tau \gg 1$ as a function of $I_1/\bar{I}$ for several the fixed values of I_2. We choose the parameters $|t_0/t_1|^2 = 1$ and $\mathrm{Re}(t_0^* t_1) = |t_0 t_1|$. For fixed $I_2 = \bar{I}$, the maximum is located at $I_1 = \bar{I}$ as expected. For fixed $I_2 > \bar{I}$, the maximum shifts to $I_1 > \bar{I}$ consistent with the predicted strong positive cross-correlations stated in Eq. (4.82)

$I_\alpha \gg \bar{I}$ factorizes, which means that the distributions are independent in this case. In general, the two tunnel current outcomes are strongly conditioned to each other, because of the simultaneous incompatible measurement. This is visualized in Fig. 4.6 where the probability distribution is plotted based on Eq. (4.86) as a function of I_1 for several fixed values of I_2. There it can be seen that for fixed $I_2 > \bar{I}$ the maximum of the distribution as a function of I_1 shifts to a value bigger than its average as well. This is consistent with the positive cross-correlations, see Eq. (4.82). In contrast, at the fine tuned point $\mathrm{Re}(t_0^* t_1) = 0$ the probability distribution (4.86) factorizes in fact for all values of the currents I_1 and I_2. Accordingly, all maxima are located at $I_1/\bar{I} = 1$ independent of the value of I_2. This is because in this case the current I_α does not couple to σ_α on the average and the strong cross-correlation effect (4.82) vanishes. Finally, in Fig. 4.7 we plot the distribution Eq. (4.86) for a larger range of outcomes to illustrate the probability distribution for rare events. This plot is consistent with the formula (4.88) and also goes beyond it by showing the full regime in which e.g. only I_1 is large and $I_2 = \bar{I}$ fixed.

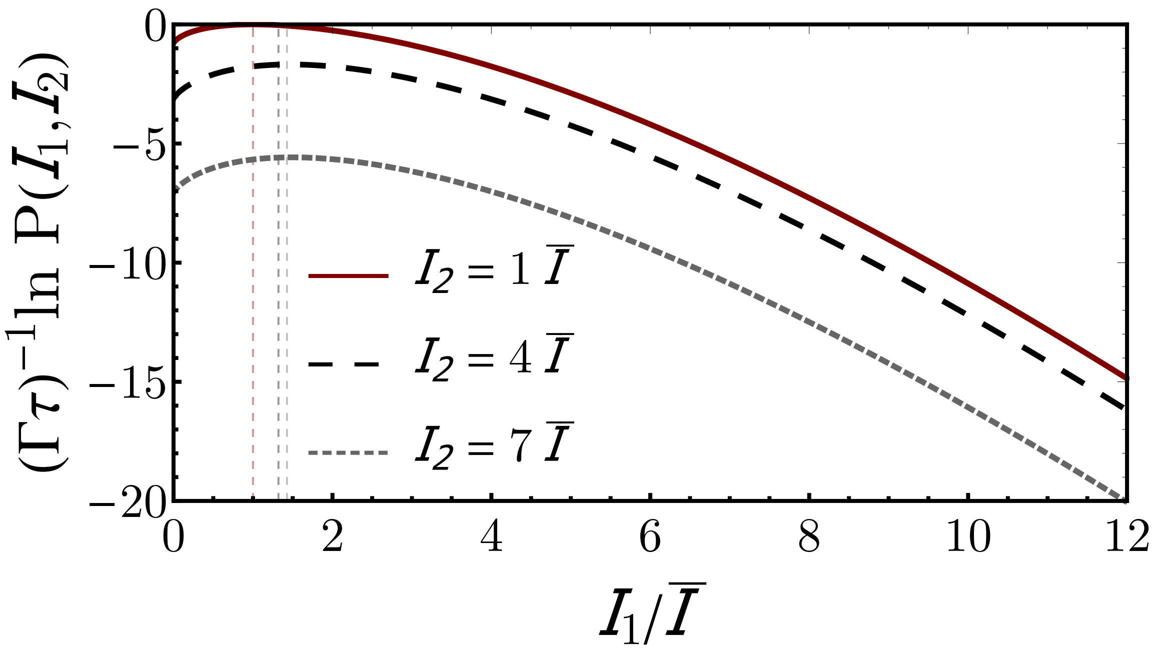

Figure 4.7: Logarithm of the outcome distribution in the case of authentic Majorana states as a function of $I_1/\bar{I}$ for several fixed values of I_2 in the limit $\Gamma\tau \gg 1$. The parameters are chosen such that $|t_0/t_1|^2 = 1$. Furthermore, we choose $\arg(t_0^* t_1) = 0$, which means that the strong positive cross-correlations, Eq. (4.82), characterizing the Majorana box qubit are present. For fixed $I_2 = \bar{I}$, the maximum is located at $I_1/\bar{I} = 1$ as expected. For fixed $I_2 > \bar{I}$, the maximum shifts to $I_1/\bar{I} > 1$, which is consistent with the latter result. For bigger values of $I_1/\bar{I}$, the probability for rare events can be inferred.

4.4.5 The effects of finite MBS coupling on the box qubit

The overlap of the Majorana wave functions results in additional finite coupling terms in the Hamiltonian $\tilde{H}_q$ given in Eq. (4.61),

$$\tilde{H}_q \to \tilde{H}_q + \sum_{\alpha=1}^{3} \varepsilon_\alpha \sigma_\alpha. \tag{4.89}$$

Finite $\varepsilon_1 \neq 0$ or $\varepsilon_2 \neq 0$ does not affect the main result for F given in formula (4.82) as long as it does not approximately cancel the splitting due to the interference links, see Eq. (4.61). Consequently, there is a high degree of robustness with respect to finite hybridizations $\sim i\gamma_\alpha\gamma_0$ coupling source and drain MBSs. However, the cross-correlations exhibit sensitivity with respect to the addition of the term $\varepsilon_3 \neq 0$ to the Hamiltonian $\tilde{H}_q$. More precisely, such hybridizations of the MBSs γ_1 and γ_2 coupled to the drain leads cause a modification of the Fano factor F in the formula (4.82). As shown in Appendix D, this modification is given by

$$F' = \eta \frac{2\left[\mathrm{Re}(t_0^* t_1)\right]^2}{|t_1|^2\left(|t_0|^2 + |t_1|^2\right)} \tag{4.90}$$

with

$$\eta = \frac{\Lambda^2\left[\nu^2 \mathrm{Re}(t_0^* t_1)\right]^2}{\Lambda^2\left[\nu^2 \mathrm{Re}(t_0^* t_1)\right]^2 + \varepsilon_3^2}. \tag{4.91}$$

Hence, $F = \mathcal{O}(1)$ is generically maintained as long as the finite coupling ε_3 fulfills $\varepsilon_3^2 \lesssim \Lambda^2\left[\nu^2 \mathrm{Re}(t_0^* t_1)\right]^2$ with Λ the bandwidth of the leads. We note that in our proposed geometries γ_1 and γ_2 are localized on different topological wires such that it is reasonable to expect that the corresponding hybridization $|\varepsilon_3|$ is sufficiently small.

4.5 Counting statistics for Andreev bound states

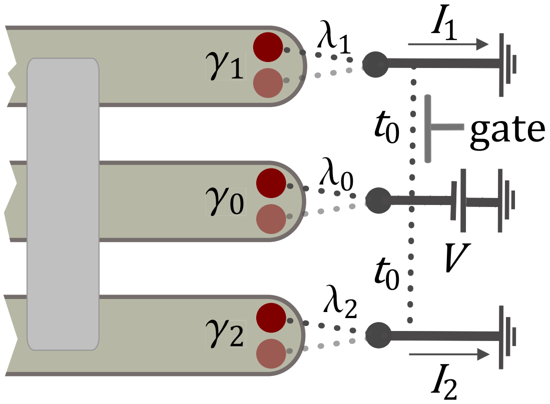

Figure 4.8: Illustration of the device setting where Andreev states are represented as pairs of MBSs γ_α^i with $i = 1, 2$. The respective couplings are denoted by λ_α^i and faded red dots represent the $i = 2$ states in each wire α. The cross-correlation shot noise Fano factor F of the currents I_1 and I_2 enables to distinguish whether a single MBS or multiple MBSs are coupled to the leads.

In this section, we analyze the full counting statistics assuming that low-energy Andreev bound states (ABSs) are coupled to the nearby leads. The latter are equivalent to a pair of Majorana components whose overlap can be generically quite small, see e.g. Ref. [50]. We adopt the simplified notation

$$t_{1,\alpha\alpha'}^{jj'} \equiv t_{\alpha\alpha'}^{jj'}, \tag{4.92}$$

and distinguish the two MBSs $\gamma_\alpha^{j=1,2}$ which may be coupled to lead α. To this end, the effective amplitude (4.92) is endowed with indices which according to Eqs. (4.14) and (4.15) refer to cotunneling processes from the i-th Majorana operator in lead α to the j-th Majorana operator in lead α'. Generally, we assume that both MBSs couple to the adjacent lead with a strength of the same order of magnitude, i.e. $\mathcal{O}(|\lambda_\alpha^i|) = \mathcal{O}(|\lambda_{\alpha'}^j|)$, such that the same is true for the effective cotunneling parameters, i.e. $\mathcal{O}(|t_{\alpha\alpha'}^{ij}|) = \mathcal{O}(|t_{\delta\delta'}^{kl}|)$. These assumptions are discussed in detail in Section 4.7. In the analysis that follows, we are again interested in the low temperature regime defined by $T \ll V$. It is not important, though, that voltage is small compared to lead bandwidth.

In terms of the Majorana operators γ_α^i and the effective tunneling amplitudes $t_{\alpha\alpha'}^{ij}$, the general evolution equation (4.58) governing the generalized density matrix $\rho_t \equiv$

$\rho_t(\chi_1, \chi_2)$ takes on the form

$$\begin{aligned}
\frac{\partial}{\partial t}\rho_t &= -i[\tilde{H}_q, \rho_t] + 2\pi\nu^2 V \left(\sum_{\alpha=1}^{2} \sum_{i,j=1}^{2} |t_{\alpha 0}^{ij}|^2 [e^{i\chi_\alpha}(i\gamma_\alpha^i\gamma_0^j)\rho_t(i\gamma_\alpha^i\gamma_0^j) - \rho_t] \right. \\
&\quad + \sum_{\alpha=1}^{2} e^{i\chi_\alpha} \sum_{(i,j)\neq(k,l)} [t_{\alpha 0}^{ij}(t_{\alpha 0}^{kl})^*(i\gamma_\alpha^i\gamma_0^j)\rho_t(i\gamma_\alpha^k\gamma_0^l) + t_{\alpha 0}^{kl}(t_{\alpha 0}^{ij})^*(i\gamma_\alpha^k\gamma_0^l)\rho_t(i\gamma_\alpha^i\gamma_0^j)] \\
&\quad + \sum_{\alpha=1}^{2}\sum_{i=1}^{2} \left[\mathrm{Im}(t_{\alpha 0}^{i1}(t_{\alpha 0}^{i2})^*)\{i\gamma_0^1\gamma_0^2, \rho_t\} + \mathrm{Im}(t_{\alpha 0}^{1i}(t_{\alpha 0}^{2i})^*)\{i\gamma_\alpha^1\gamma_\alpha^2, \rho_t\} \right] \\
&\quad \left. - \sum_{\alpha=1}^{2} \mathrm{Re}\left(t_{\alpha 0}^{11}(t_{\alpha 0}^{22})^* - t_{\alpha 0}^{21}(t_{\alpha 0}^{12})^*\right) \{\gamma_\alpha^1\gamma_\alpha^2\gamma_0^1\gamma_0^2, \rho_t\} \right). \qquad (4.93)
\end{aligned}$$

Here the Hamiltonian evolution is generated by

$$\begin{aligned}
\tilde{H}_q &= 4\nu^2 V(1 + \ln(\Lambda/2V)) \sum_{l,\alpha=1}^{2} \left[\mathrm{Im}((t_{\alpha 0}^{l1})^* t_{\alpha 0}^{l2}) i\gamma_0^1\gamma_0^2 + \mathrm{Im}((t_{\alpha 0}^{1l})^* t_{\alpha 0}^{2l}) i\gamma_\alpha^1\gamma_\alpha^2 \right] \\
&\quad - 2\nu^2\Lambda \sum_{\alpha<\alpha'} \mathrm{Re}\left((t_{\alpha\alpha'}^{11})^* t_{\alpha\alpha'}^{22} - (t_{\alpha\alpha'}^{21})^* t_{\alpha\alpha'}^{12}\right) \gamma_\alpha^1\gamma_\alpha^2\gamma_{\alpha'}^1\gamma_{\alpha'}^2. \qquad (4.94)
\end{aligned}$$

4.5.1 Counting statistics for source lead coupled to ABS

In this subsection, we will show that the shot noise cross-correlation amplitude is extremely sensitive to an ABS coupled to the source lead. In fact, the cross-correlations are characterized generically by a Fano factor $|F| = \mathcal{O}(1)$ whenever more than a single MBS is coupled to the source lead, i.e. $N_0 > 1$. For this statement it does not matter whether the drain leads are coupled to MBSs or ABSs and whether the interference links are present or not.

We demonstrate this by first considering the case $N_0 = 2$, $N_{1,2} = 1$ in the absence of the interference links, i.e. for $t_0 = 0$. After times $\tilde{\mathit{\Gamma}}_\alpha \tau \gg 1$ with the rates $\tilde{\mathit{\Gamma}}_\alpha = 2\pi\nu^2(|t_{\alpha 0}^{11}|^2 + |t_{\alpha 0}^{12}|^2)V$ and at low temperature, $T \ll V$, we obtain (see Appendix E) the cumulant generating function $\tau^{-1}\ln\mathcal{Z}$ as the eigenvalue of $\tilde{\theta}\mathbb{I} + \tilde{M}$ which vanishes at $(\chi_1, \chi_2) = (0, 0)$. Here we have defined

$$\tilde{\theta} = 2\pi\nu^2 V \sum_{\alpha=1}^{2}\sum_{i=1}^{2} |t_{\alpha 0}^{1i}|^2 (e^{i\chi_\alpha} - 1) \qquad (4.95)$$

and the matrix

$$\tilde{M} = 4\pi\nu^2 V \sum_{\alpha=1}^{2} \begin{pmatrix} 0 & -\eta_\alpha(e^{i\chi_\alpha} - 1) \\ \eta_\alpha(e^{i\chi_\alpha} + 1) & -(|t^{11}_{\alpha 0}|^2 + |t^{12}_{\alpha 0}|^2)e^{i\chi_\alpha} \end{pmatrix} \tag{4.96}$$

as well as an interference parameter $\eta_\alpha = \mathrm{Im}(t^{11}_{\alpha 0}(t^{12}_{\alpha 0})^*)$. By performing the derivatives we obtain the second cumulant

$$\begin{aligned} S_{12} \quad = \quad 2\pi\nu^2 V \Bigg[& \frac{[\mathrm{Im}((t^{11}_{10})^* t^{12}_{10})]^2 + [\mathrm{Im}((t^{11}_{20})^* t^{12}_{20})]^2}{|t^{11}_{10}|^2 + |t^{12}_{10}|^2} \\ & - \frac{2\mathrm{Im}(t^{11}_{10}(t^{12}_{10})^*)\mathrm{Im}(t^{11}_{20}(t^{12}_{20})^*) \left[\mathrm{Im}(t^{11}_{10}(t^{12}_{10})^*) + \mathrm{Im}(t^{11}_{20}(t^{12}_{20})^*)\right]^2}{\left(|t^{11}_{10}|^2 + |t^{12}_{10}|^2\right)^3} \Bigg]. \end{aligned} \tag{4.97}$$

This contribution is of the same order of magnitude as the current and hence the Fano factor is of order unity,

$$|F| = \mathcal{O}(1), \tag{4.98}$$

despite the absence of the interference links. This is in stark contrast to the case of the Majorana box qubit where interference links t_0 (of the order of $t^{11}_{1,\alpha 0}$) were essential to the observation of $|F| = \mathcal{O}(1)$. We can see from the formula (4.97) how the gradual decoupling of just one of the two MBS components belonging to the ABS causes this contribution to diminish. We stress that $|F| = \mathcal{O}(1)$ as long as the couplings $t^{jj'}_{\alpha\alpha'}$ are of the same order of magnitude, even when the couplings are made arbitrarily small. Let us further analyze the formula (4.97): It is straightforward to see that the first term is always positive, while the second term can have either sign. The second term vanishes when $\mathrm{Im}((t^{11}_{1,10})^* t^{12}_{1,10}) = -\mathrm{Im}((t^{11}_{1,20})^* t^{12}_{1,20})$ in which case the Fano factor characterizing the cross-correlations takes on the simple form

$$F = \frac{\left[\mathrm{Im}((t^{11}_{1,10})^* t^{12}_{1,10})\right]^2}{\left(|t^{11}_{1,10}|^2 + |t^{12}_{1,10}|^2\right)^2} = \mathcal{O}(1). \tag{4.99}$$

Moreover, it follows from Eq. (4.97) that $|F| = \mathcal{O}(1)$ is predicted to persist upon the inclusion of interference links, $t_0 \neq 0$, or the coupling of additional MBSs to either one of the leads as long as more than a single MBS is coupled to the source lead, $N_0 > 1$. This can be understood because additional MBSs or interference links result in additional parameters in the problem which are independent and hence generically cannot cancel the $\mathcal{O}(1)$ contribution displayed in Eq. (4.97).

Physically, despite being robustly energetically low-lying, the ABSs typically are are not exactly at zero energy. Rather, due to small overlap of the MBS components a finite term of the form

$$\tilde{H}_q \rightarrow \tilde{H}_q + \sum_{\alpha=1}^{3} \tilde{\varepsilon}_\alpha (i\gamma_\alpha^1 \gamma_\alpha^2) \tag{4.100}$$

arises. The parameters $\tilde{\varepsilon}_\alpha$ are small compared to the induced gap. We show in Appendix E that the inclusion of such a term does not affect the results discussed in this subsection. In fact, e.g. the formulas (4.97) and (4.99) are unaffected by it.

4.5.2 Counting statistics for drain leads coupled to ABSs

In this subsection we will show that the shot noise cross-correlation amplitude is unaffected if ABSs are coupled only to the drain leads, but not to the source lead. Therefore, we now analyze the case $N_{1,2} = 2$ and $N_0 = 1$ first in the absence of the interference links, $t_0 = 0$. We find that $\tau^{-1} \ln \mathrm{Tr}\rho_\tau$ is given by the unique eigenvalue of $\theta' I + M'$ which vanishes at $(\chi_1, \chi_2) = (0, 0)$, with

$$\theta' = 2\pi\nu^2 V \sum_{\alpha=1}^{2} \sum_{i=1}^{2} |t_{1,\alpha 0}^{i1}|^2 (e^{i\chi_\alpha} - 1) \tag{4.101}$$

and the matrix

$$M' = \begin{pmatrix} 0 & c_{1,-} & c_{2,-} & 0 \\ -c_{1,+} & -d_1 & 0 & c_{2,-} \\ -c_{2,+} & 0 & -d_2 & c_{1,-} \\ 0 & -c_{2,+} & -c_{1,+} & -d_1 - d_2 \end{pmatrix}. \tag{4.102}$$

The quantities $c_{\alpha,\pm}$ are defined as

$$c_{\alpha,\pm} = 4\pi\nu^2 V \mathrm{Im}(t_{1,\alpha 0}^{11} (t_{1,\alpha 0}^{21})^*)(e^{i\chi_\alpha} \pm 1). \tag{4.103}$$

Furthermore, d_α is defined as

$$d_\alpha = 4\pi\nu^2 V \sum_{j=1}^{2} |t_{1,\alpha 0}^{j1}|^2 e^{i\chi_\alpha}. \tag{4.104}$$

At zero temperature we obtain to the leading order of the current

$$S_{12} = 0. \tag{4.105}$$

In conclusion, this result shows that without interference links ($t_0 = 0$) one has a strongly suppressed Fano factor if the ABSs are only coupled to the drain leads. Hence, the key requirement for the observation of the signature $F = \mathcal{O}(1)$ for $t_0 = 0$ is that multiple MBSs couple to the source lead, i.e. $N_0 > 1$. On the other hand, for $N_0 = 1$ and more than a single MBS coupled to either or both of the drain leads, the predicted order of magnitude of F coincides with the Majorana qubit case. As we will discuss below, this fact can be effectively addressed by variation of the bias voltage configurations. We also remark that for finite ABS energy (4.100) the result stated in Eq. (4.105) remains unchanged.

4.6 Weak measurement protocols for MBS detection

The effect of remarkably pronounced current cross-correlations is an observable consequence of the underlying Pauli algebra of the Majorana box qubit. The conditions under which this effect occurs depend on the chosen device configuration. This leads to several qualitative and experimentally verifiable predictions that allow to test the genuineness of the Majorana qubit. Regarding the device configuration we have two choices in mind: First, the way in which the bias is applied and, second, whether the device is interferometric or not − meaning whether electrons have a second direct tunneling bridge t_0 available to reach either of the two leads. The prime observable is the Fano factor F, which characterizes the cross-correlations via the relation

$$S_{12} = F\bar{I}, \tag{4.106}$$

with the average current $\bar{I} = \langle I_\alpha \rangle$. The distinctive predictions for setups containing genuine MBSs and local fermionic states are summarized in Table 4.1.

	$\boldsymbol{t_0 \neq 0}$	$\boldsymbol{t_0 = 0}$
Majorana bound states ($N_\alpha = 1$)	$\lvert F\rvert = \mathcal{O}(1)$	$\lvert F\rvert \ll 1$
Andreev bound states ($N_0 = 2,\ N_{1,2} = 1,2$)	$\lvert F\rvert = \mathcal{O}(1)$	$\lvert F\rvert = \mathcal{O}(1)$
Andreev bound states ($N_0 = 1,\ N_{1,2} = 1,2$)	$\lvert F\rvert = \mathcal{O}(1)$	$\lvert F\rvert \ll 1$

Table 4.1: The results are shown for the Fano factor, $|F|$, depending on the number of MBSs coupled to each terminal α. A functional Majorana qubit is characterized by its underlying Pauli algebra and by single MBSs localized at the ends of the 1D TSCs. By measuring the Fano factor, both in the presence and absence of interference links t_0, the Majorana box qubit is clearly identified. It is important that for the non-interferometric configuration (for $t_0 = 0$) each terminal serves as source lead at least once, see Fig. 4.9. This addresses the fact that the Fano factor is sensitive only to Andreev states coupled to the source lead, $\alpha = 0$, which can be seen by comparing the first and the third row.

The continuous monitoring of a Majorana Pauli operator algebra reflects itself in strong positive cross-correlations with $F = \mathcal{O}(1)$ for the interferometric setting in which $t_0 \neq 0$. If a single Majorana state is coupled to the source lead (and the drain terminals either to MBSs or ABSs), the Fano factor is parametrically suppressed $|F| = \mathcal{O}(T/V, \nu^2 |t^{ij}_{\alpha\alpha'}|^2) \ll 1$ in the absence of these interference paths, $t_0 = 0$. If an ABS is coupled to the source lead (and either MBSs ore ABSs to the drain leads), there is a strong level of cross-correlations independent of the absence or presence of the interference links t_0. It is this insensitivity of the cross-correlation profile to the presence of the interference link which indicates the presence of an Andreev state coupled to the source electrode. Thus, for pinched off interference links, $t_0 = 0$, the cases of ABSs and MBSs coupled to the source lead differ by a strong observable effect. All of this is to be contrasted with noninteracting electrons in the limit $T \ll V$ in a T-shaped junction. In this case, the currents are approximately uncorrelated and the Fano factor is parametrically suppressed in the dimensionless tunnel conductance [104] as previously mentioned.

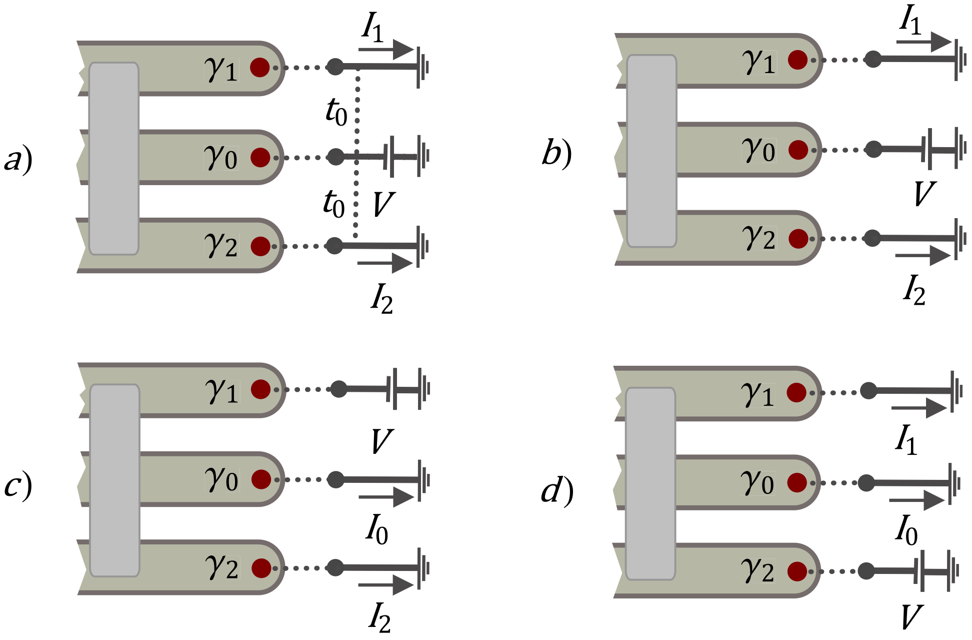

Figure 4.9: The four device configurations for which the Fano factor F has to be measured to identify the nonlocal Pauli algebra. In a) the interferometric setting with $t_0 \neq 0$ is shown, which allows to confirm the $F = \mathcal{O}(1)$ prediction for genuine MBSs. In the non-interferometric ($t_0 = 0$) settings b), c), d), each lead serves as source once, while the currents flowing to the drains are being measured. Here in each case $F \ll 1$ is predicted for a genuine Majorana box qubit.

Since the sensitivity of the Fano factor is limited to distinguish single and multiple MBSs that are coupled to the source terminal, it is important to exchange the role of the drain and source to clearly identify the Majorana box qubit with $N_\alpha = 1$ for $\alpha = 0, 1, 2$. This results in the following necessary measurement configurations, shown in Fig. 4.9, for which the Fano factor has to be determined:

$t_0 \neq 0$: Measurement of $|F|$ with the central lead $\alpha = 0$ as source to confirm a positive $F = \mathcal{O}(1)$.

$t_0 = 0$: Measurement of $|F|$ with the bias V applied such that each lead α (for $\alpha = 0, 1, 2$) serves as source at least once to confirm $|F| \ll 1$. As soon as one observes strong cross-correlations $|F| = \mathcal{O}(1)$ for lead α operated as source, one can conclude that $N_\alpha > 1$.

In addition, there are two control measurements that can be carried out to avoid misinterpretation: First, accidental fine tuning may be the origin of a $|F| \ll 1$ signature, e.g. if $\arg(t_0^* t_1) = \pi/2$ in Eq. (4.82). However, the suppression of the Fano factor $|F| \ll 1$ for ABSs requires substantial fine tuning and is non-generic. Therefore, this scenario can be ruled out by a modest number of measurement repetitions for different strengths of the gate potentials regulating the tunneling amplitudes as well as magnetic field values to change the microscopic details. Second, since all results hold to leading order in the tunnel conductances, one can repeat the protocol for a sequence of several decreasing conductance strengths. Contributions with entry $|F| = \mathcal{O}(1)$ in Table 4.1 remain unchanged parametrically, while the entries $|F| \ll 1$ are further suppressed.

4.7 Conclusions and outlook

The weak measurement protocols proposed in Section 4.6 constitute a new method to detect MBSs. For a given Majorana qubit candidate, several qualitative predictions can be tested to unveil the genuineness of the device. The observable to be measured is the current cross-correlation amplitude, which is characterized by a remarkably large Fano factor $|F| = \mathcal{O}(1)$, see Eq. (4.82). The Fano factor is of order unity even for arbitrarily small dimensionless tunnel conductances $2\pi\nu^2 t_{0,\alpha}$ and $2\pi\nu^2 t_{1,\alpha 0}$ as long as they are of the same order of magnitude[4].

These pronounced cross-correlations for a Majorana qubit arise due to the simultaneous measurement of the nonlocal Pauli operators $\sigma_1 = i\gamma_1\gamma_0$ and $\sigma_2 = i\gamma_2\gamma_0$, which are coupled to the two currents I_1 and I_2 respectively. The physical mechanism leading to this effect is intimately related to the incompatibility of the two current readouts and the ensuing frustration and conflictedness within the system. To better understand this point, consider an electron which is incoming from the source and contributes to the current I_1. This electron helps to project $i\gamma_1\gamma_0$ onto a definite state. This, in turn, increases the uncertainty in the expectation value of the operator $i\gamma_2\gamma_0$, which is noncommuting with $i\gamma_1\gamma_0$. In this way, the aforementioned electron affects the transmission phase shift in the cotunneling amplitude for a subsequent electron that contributes to the current I_2. This physical interpretation accounts for two important features: First, the occurrence of correlations even when the subsequent electron is incoming much later. This is the case in the weak tunneling limit of interest, where electrons tunnel one-by-one through the barriers. And second, it explains that the observation of $|F| = \mathcal{O}(1)$ for the Majorana qubit requires the setting to be interferometric, i.e. $t_{0,\alpha} \neq 0$. For completeness, we also performed an analysis on how the result for the Fano factor is affected by finite MBS hybridization on the box as well as finite temperature in the Subsections 4.4.3 and 4.4.5. There we found that both effects can cause a weakening of the Fano factor. However, we anticipate that the Fano factor $|F| = \mathcal{O}(1)$ will remain identifiable despite these effects due to the strength of the cross-correlations.

Several approximations have been made in our theoretical analysis. Generally, the results were derived perturbatively in the dimensionless tunnel conductances $2\pi\nu^2 t_{0,\alpha}$

---

[4] The dimensionless tunnel conductances are defined in the Hamiltonians given in Eqs. (4.14) and (4.32). According to these definitions, ν is the density of states in the leads and $t_{0,\alpha}$ describes the tunneling link connecting lead 0 and lead α. On the other hand, $t_{1,\alpha 0}$ describes the effective cotunneling form lead 0 to lead α.

and $2\pi\nu^2 t_{1,\alpha 0}$. Furthermore, the Lindblad equation augmented with counting parameters that we used to derive the results was subject to a Markovian approximation. The latter amounts to neglecting possible memory effects. Moreover, the low-energy Hamiltonian Eq. (4.14) does not include several features which are present in a real experiment. Such features include the Zeemann field, spin-orbit coupling and the detrimental effects of quasiparticles above the gap (more on this point below). However, the effective Hamiltonian accounts accurately for the essential physics on low energy scales compared to charging energy E_C and pairing gap Δ. And most importantly, the Fano factor of order unity represents such a strong effect that it will remain identifiable also upon the inclusion of further correction terms. Hence, we can draw the conclusion that the qualitative properties of the predicted signatures will persist when more sophisticated microscopic models are used.
We now turn in more detail to the in- and out-tunneling of quasiparticles through the MBSs. The noise and decoherence caused by these processes could potentially compromise the interpretation of the cross-correlation amplitudes, which were derived in the long time (zero-frequency) limit. The $F = \mathcal{O}(1)$ effect, Eq. (4.82), for genuine MBSs appears after the time scale Γ^{-1} with $\Gamma \equiv 2\pi\nu^2|t_1|^2V$. Therefore, we summarize a protocol [11] geared to the characterization of the typical timescale of quasiparticle poisoning processes. Consider both $t_{0,2} = \lambda_2^j = 0$ such that lead 2 remains decoupled. The current I_1 then depends on the state of the MBSs through the expectation value of σ_1 (or, more generally, that of an operator $\mathcal{O}_{10}$ if ABSs are present). Beyond a time scale $\tau_{\text{proj}} \sim 1/V$, the measurement of I_1 becomes projective, and a weakly fluctuating result defined by one of the two values $\langle\sigma_1\rangle \to \pm 1$ is approached. However, quasiparticle tunneling accidentally switching the state $\sigma_1 \to -\sigma_1$ will cause discrete jumps in the readout. Monitoring of the current signal therefore allows to study the quasiparticle poisoning processes.

We have shown that for Andreev bound states the Fano factor signatures generically differ in a drastic way. This is due to the underlying operator algebra, which in this case is different from the nonlocal Pauli algebra. We emphasize again that observation of the ABS signatures discussed in Section 4.6 requires that both Majorana components forming the ABS actually couple to the nearby lead. If one of the MBS components of the ABS is invisible to the nearby electrode, MBSs and ABSs are in principle indistinguishable. Note that there are studies stating that for smooth confining potentials, in fact, only one MBS component effectively couples while the coupling of the other component is exponentially smaller (see e.g. Refs. [49, 50]). It has also been discussed, however, that the coupled "fake" MBS could potentially still be used for braiding [52]. We reiterate that the protocol presented in Section 4.6 is tailor made to distinguish for each lead α a single coupled MBS, $N_\alpha = 1$, and multiple coupled MBSs, $N_\alpha > 1$. Hence, the protocol does not distinguish the topological (N_α odd) from the non-topological (N_α even) superconductor. However, we believe our protocol is highly useful in practice, because it is desirable to identify a functional Majorana qubit with $N_\alpha = 1$. This is because a topologically nontrivial system in which a genuine MBS coexists with additional low-lying Andreev states causes a reduced effective gap rendering the device computationally less useful.

In summary, the proposed protocols rely on available experimental hardware and, therefore, may allow to detect the Pauli algebra of a Majorana box qubit in the near future. The experiments have to be performed in the Coulomb blockade regime at low temperatures, $T \ll V$, and in the tunneling limit, i.e. $2\pi\nu^2 t_{0,\alpha} \ll 1$ and $2\pi\nu^2 t_{1,\alpha 0} \ll 1$. Here, one must not underestimate the task of shot noise measurement in nanoscale devices where the electrons tunnel one-by-one through the barriers. Despite that, the weak measurement protocols may represent the operationally and practically most viable option to detect the Pauli algebra of the Majorana box qubit and the nonlocality of MBSs. The successful completion of these experiments would constitute notable progress that could erase the doubts about the MBS. Nevertheless, at some point in the future actual braiding of MBSs has to be performed, which would constitute a landmark achievement in condensed matter physics.

Chapter 5

Further new approaches to MBS detection

The theory of MBS detection is a major theme in this thesis and has been addressed at length in Chapter 4. In the present chapter, we investigate two further transport spectroscopic methods. First, in Section 5.1, we discuss detection based on current cross-correlations for a single Coulomb blockaded Majorana quantum wire with three tunnel coupled electrodes. Second, in Section 5.2, we study MBS identification based on two terminal projective conductance measurements by means of a protocol that accesses the number of distinct current outcomes. Beyond the usefulness of these detection protocols, the discussion in Section 5.3 reveals that the aforementioned protocol of simultaneous monitoring a nonlocal Pauli algebra of Chapter 4 accesses the most information related to the fundamental nature of MBSs.

5.1 Current cross-correlations for a single Majorana quantum wire

5.1.1 Three-terminal device and theoretical model

We now explore current cross-correlation experiments based on a single TSC wire in the Coulomb blockade regime. In particular, we consider that one end of the Majorana wire is coupled to a source lead while two separate drain leads are coupled to the other end

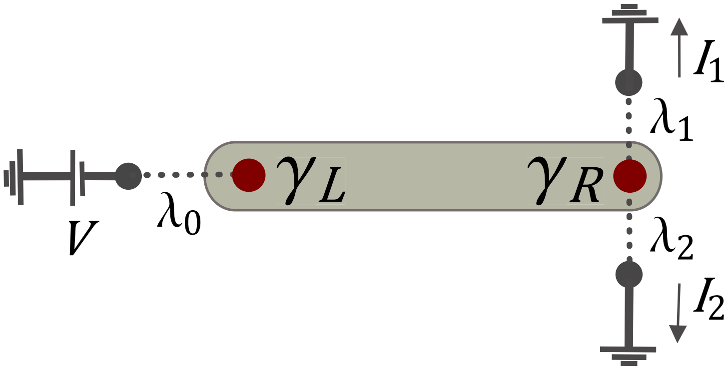

Figure 5.1: Experimental setting of a topological superconducting nanowire (green) coupled to three normal metal leads (thick black lines). A bias voltage V is applied to operate the lead 0, which is tunnel coupled to the MBSs γ_{L}^i localized at the left wire end (red dots), as the source. At the right end of the wire the two drain leads 1 and 2, which are electrically isolated from each other, are tunnel coupled to the MBSs γ_{R}^i. The two currents I_1 and I_2 are flowing to ground and the cross correlation amplitude $S_{12} = F \langle I \rangle$ gets measured with $\langle I_\alpha \rangle = \langle I \rangle$. The quantity F contains qualitative information on the number of MBSs $\gamma_{\mathrm{L/R}}^i$ that are coupled to the respective leads. The observation of $F \ll 1$ is consistent with single genuine MBSs. On the other hand, $F = O(1)$ implies that ABSs are being present.

(see Fig. 5.1). The experiments are envisioned to be carried out at low temperature T in comparison to the applied voltage bias V. The charging Hamiltonian is again given by $H_C = E_c \left(N - n_g\right)^2$ with a large charging energy E_C. Let the equilibrium charge on the floated wire be the integer N_0 in units of the elementary charge with the tunable backgate parameter $n_g = N_0 + \Delta n_g$ that is weakly detuned, $\Delta n_g \ll 1$. The microscopic tunneling Hamiltonian [30] for the system depicted in Fig. 5.1 reads

$$\begin{aligned} H &= H_{\mathrm{Leads}} + H_C + \sum_{j=1}^{N_{\mathrm{L}}} \sum_k \left[\lambda_0^j c_{0,k}^\dagger \gamma_{\mathrm{L}}^j e^{-i\phi/2} + \mathrm{H.c.} \right] \\ &\quad + \sum_{j=1}^{N_{\mathrm{R}}} \sum_k \left[(\lambda_1^j c_{1,k}^\dagger + \lambda_2^j c_{2,k}^\dagger) \gamma_{\mathrm{R}}^j e^{-i\phi/2} + \mathrm{H.c.} \right], \end{aligned} \tag{5.1}$$

with $N_{\mathrm{L/R}}$ MBSs $\gamma_{\mathrm{L/R}}^i$ being localized on the left and right end of the wire respectively. As before, the parameters λ_α^j are tunnel couplings, the operator $e^{-i\phi/2}$ lowers the island charge and H_{Leads} describes the metallic leads. Using perturbation theory for the case $N_{\mathrm{L/R}} = 1$ yields the effective tunneling Hamiltonian for single MBSs (see Appendix F)

$$H_{\mathrm{MBS,eff}} = \sum_{k,k'} \left[\eta^1 c^\dagger_{1,k} c_{2,k'} + i\gamma^1_{\mathrm{R}}\gamma^1_{\mathrm{L}} \sum_{\alpha=1}^{2} t^{11}_{\alpha 0} c^\dagger_{\alpha,k} c_{0,k'} + \mathrm{H.c.} \right], \tag{5.2}$$

where the direct hopping amplitude from lead 1 to 2 is given by

$$\eta^j \simeq -\frac{4\Delta n_g \lambda^j_1 (\lambda^j_2)^*}{E_C} \tag{5.3}$$

and $t^{jj'}_{\alpha\alpha'} \simeq 2i\lambda^j_\alpha (\lambda^{j'}_{\alpha'})^*/E_C$. Note that η^j is proportional to $\Delta n_g = n_g - N_0 \ll 1$ and originates in the tunneling process $c_2 \to \gamma^j_{\mathrm{R}} \to \gamma^j_{\mathrm{R}} \to c_1$ with $c_{\alpha=1,2}$ the drain lead fermions. For the case of ABSs $N_{\mathrm{L/R}} = 2$, we obtain the effective Hamiltonian (see Appendix F)

$$\begin{aligned} H_{\mathrm{ABS,eff}} &= H_{\mathrm{Leads}} + \sum_{\alpha=1}^{2}\sum_{j=1}^{2}\sum_{j'=1}^{2}\sum_{k,k'} \left[t^{jj'}_{\alpha 0} (i\gamma^j_{\mathrm{R}}\gamma^{j'}_{\mathrm{L}}) c^\dagger_{\alpha,k} c_{0,k'} + \mathrm{H.c.} \right] \\ &\quad + \sum_{k,k'} \left[\left(t^{12}_{12} (i\gamma^1_{\mathrm{R}}\gamma^2_{\mathrm{R}}) + \eta^1 + \eta^2 \right) c^\dagger_{1,k} c_{2,k'} + \mathrm{H.c.} \right]. \end{aligned} \tag{5.4}$$

In order to derive the counting statistics, we follow the same strategy as in Chapter 4. The equation governing the time evolution of the reduced density matrix $\rho_t(\chi_1, \chi_2)$ in the Hilbert space corresponding to the Majorana operators $\gamma^j_{L/R}$ is given by

$$\begin{aligned} \frac{\partial}{\partial t}\rho_t &= -i[H_q, \rho_t] + 2\pi\nu^2 V \sum_{\alpha=1}^{2} \tilde{\mathcal{D}}_{\alpha 0}(\rho_t) \\ &\quad + 2\pi\nu^2 T \left(\tilde{\mathcal{D}}_{12}(\rho_t) + \tilde{\mathcal{D}}_{21}(\rho_t) \right). \end{aligned} \tag{5.5}$$

The superoperator is defined as

$$\tilde{\mathcal{D}}_{\alpha\alpha'}(\rho) \equiv e^{i(\chi_\alpha - \chi_{\alpha'})} \mathit{\Pi}_{\alpha\alpha'} \rho \mathit{\Pi}^\dagger_{\alpha\alpha'} - \frac{1}{2}\{\mathit{\Pi}^\dagger_{\alpha\alpha'}\mathit{\Pi}_{\alpha\alpha'}, \rho\} \tag{5.6}$$

with the counting parameters χ_α defined as in Chapter 4 and again $\chi_0 \equiv 0$. The operators $\mathit{\Pi}_{\alpha\alpha'}$ are defined according to

$$\mathit{\Pi}_{\alpha 0} = \sum_{j,j'=1}^{2} t^{jj'}_{\alpha 0} (i\gamma^j_{\mathrm{R}}\gamma^{j'}_{\mathrm{L}}) \tag{5.7}$$

and

$$\mathit{\Pi}_{12} = \eta^1 + \eta^2 + t^{12}_{12}(i\gamma^1_{\mathrm{R}}\gamma^2_{\mathrm{R}}) \tag{5.8}$$

with $\mathit{\Pi}_{21} = \mathit{\Pi}^\dagger_{12}$. The Hamiltonian part of the dynamics for $T \ll V \ll \Lambda$ is generated by

$$H_q = \nu^2 V \ln(\Lambda/2V)) \sum_{\alpha=1}^{2} [\mathit{\Pi}_{\alpha 0}, \mathit{\Pi}^\dagger_{\alpha 0}] - \frac{\nu^2 \Lambda}{2} \sum_{\alpha<\alpha'} \{\mathit{\Pi}^\dagger_{\alpha\alpha'}, \mathit{\Pi}_{\alpha\alpha'}\}. \tag{5.9}$$

In the next subsection, we will discuss the resulting current cross-correlations.

5.1.2 Signatures of current cross-correlations

The cross-correlation amplitude $S_{12} = \int_0^t dt\, \langle\langle I_1(t) I_2(0)\rangle\rangle$ can be derived from the evolution equation augmented with counting parameters stated in Eq. (5.5), which is shown in Appendix F. In the case of genuine single MBSs, $N_{\mathrm{L/R}} = 1$, we obtain thermal anticorrelations as the leading order contribution to the cross-correlations:

$$S_{12} = -4\pi\nu^2 |\eta^1|^2 T. \tag{5.10}$$

Assuming that the couplings are of the same order, i.e. $\mathcal{O}(\lambda_\alpha) = \mathcal{O}(\lambda_{\alpha'})$, we find that the Fano factor for MBSs is small

$$|F| = \mathcal{O}\left(\Delta n_g \frac{T}{V}\right) \ll 1. \tag{5.11}$$

In fact, it is parametrically suppressed in temperature $T/V \ll 1$ and the small detuning $\Delta n_g \ll 1$. Experimental variation of the back gate parameter can, therefore, tune the strength of the thermal anticorrelations.

In stark contrast to the result (5.11), in the ABS case there are generically strong cross-correlations characterized by a Fano factor $|F| = \mathcal{O}(1)$. To demonstrate this point it is sufficient to discuss the case $N_{\mathrm{R}} = 2$, $N_{\mathrm{L}} = 1$. Physically, this situation may be realized when only one of the MBSs localized at the left wire end couples effectively to the nearby lead, a situation that has been discussed e.g. in Ref. [50]. By solving the corresponding master equation augmented with counting parameters (see Appendix F), we obtain the cross-correlation amplitude

$$\begin{aligned} S_{12} \; &= \; 8\pi\nu^2 V \left[\frac{\sum_{j=1}^{2} \left(\left[\mathrm{Im}(t^{11}_{10}(t^{12}_{10})^*)\right]^2 |t^{1j}_{20}|^2 + \left[\mathrm{Im}(t^{11}_{20}(t^{12}_{20})^*)\right]^2 |t^{1j}_{10}|^2 \right)}{\left(\sum_{\alpha=1}^{2}\sum_{j=1}^{2} |t^{1j}_{\alpha 0}|^2\right)^2} \right. \\ & \left. - \frac{4\mathrm{Im}(t^{11}_{10}(t^{12}_{10})^*)\mathrm{Im}(t^{11}_{20}(t^{12}_{20})^*)\left[\mathrm{Im}(t^{11}_{10}(t^{12}_{10})^*) + \mathrm{Im}(t^{11}_{20}(t^{12}_{20})^*)\right]^2}{\left(\sum_{\alpha=1}^{2}\sum_{j=1}^{2} |t^{1j}_{\alpha 0}|^2\right)^3} \right] . \qquad (5.12) \end{aligned}$$

Hence, assuming again that the couplings are of the same order, i.e. $\mathcal{O}(\lambda^{j}_{\alpha}) = \mathcal{O}(\lambda^{j'}_{\alpha'})$, we predict a generic Fano factor of order unity,

$$|F| = \mathcal{O}(1). \qquad (5.13)$$

We point out that $|F| = \mathcal{O}(1)$ is generally the case whenever $N_{\mathrm{R}} > 1$ and $N_{\mathrm{L}} \geq 1$ is satisfied. The situation may also be realized in a topological Majorana wire, where the genuine MBSs coexist with ABSs. Thus, the cross-correlations in this setting provide another scheme to distinguish single MBSs, which are characterized by the strong suppression $F \sim \Delta n_g T/V$, from ABSs. This is summarized in Table 5.1.

	Cross-correlation Fano factor
Majorana states	$\lvert F\rvert = \mathcal{O}\left(\Delta n_g T/V\right) \ll 1$
Andreev bound states	$\lvert F\rvert = \mathcal{O}(1)$

Table 5.1: Qualitative behavior of the Fano factor, $|F|$, characterizing the cross-correlations for single vs multiple MBSs localized at the ends of the nanowire. The key observable distinguishing between the two cases is the large value $|F| = \mathcal{O}(1)$ for Andreev bound states, which is to be contrasted with the strong suppression $|F| \sim \Delta n_g T/V$ for MBSs. Observing the first line is a result consistent with MBSs and the experimentalist can conclude that not more than single MBSs are coupled to the respective terminals.

The main advantage of the protocol is its ability to rule out ABSs based on the distinctive large cross-correlations that are present in this case. However, observing $F \ll 1$ (first line of Table 5.1) does not contain a direct signature of the MBSs. This can be seen by replacing $\gamma^1_{\mathrm{R/L}}$ by complex numbers in the Hamiltonian (5.2) in which case F is suppressed as well. Thus, observation of $F \ll 1$ is consistent with single MBSs and one learns from it that not more than single MBSs are coupled to the respective leads.

5.2 MBS detection via number of projective current outcomes

In this section, we consider projective current measurements on a Majorana qubit as studied in Ref. [11]. As in this reference, we consider a floating Majorana qubit with two normal-conducting leads coupled to two different Majorana states in the presence of an applied bias, see Fig. 5.2. The idea is to investigate the extent to which MBSs and ABSs can be distinguished based on the number of distinct projective current outcomes.

The charging Hamiltonian of the Majorana box qubit is again given by $H_C = E_c \left(N - n_g\right)^2$. In order to practically identify different current outcomes (stationary currents), one has to measure the current multiple times projectively. To this end, we propose the option to run two currents simultaneously to reset the qubit by temporarily coupling the box qubit to a third lead as well. Let N_α be the number of MBSs coupled

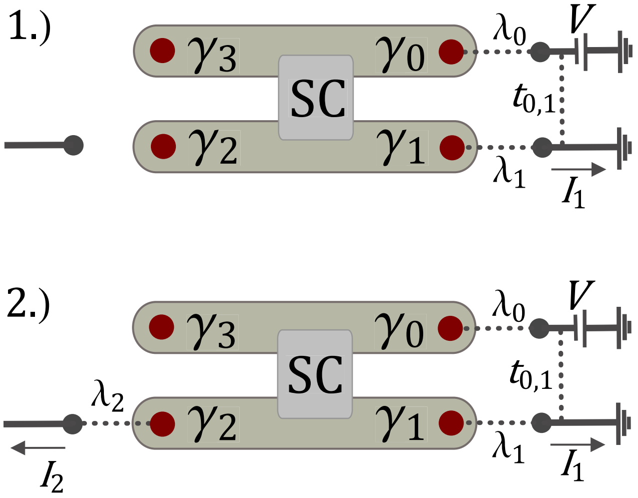

Figure 5.2: The two alternating stages of the protocol are displayed. Top: Stage of projective measurement of the current $\langle I_1 \rangle$ [11] in the box qubit geometry. Only the source lead 0 and a single drain lead 1 (thick black lines on the right) are being coupled to the island, a bias is applied and an interference link $t_{0,1}$ serves as direct tunneling link. Bottom: Resetting stage of the box qubit, which prepares for the next projective measurement iteration. Three leads are being coupled such that due to the biasing on average the two currents I_1 and I_2 flow simultaneously. The dynamics during this stage brings the qubit density matrix in the maximally mixed state as discussed in Subsection 4.4.2. After a certain time lead 2 is detached again and step 1.) is repeated.

to lead α. According to the discussion of Section 4.2, the effective Hamiltonian during the projective measurement stage (upper half of Fig. 5.2) is given by

$$\tilde{H}_T = (t_{0,1} + \mathcal{O}_{10}) \sum_{k,k'} c^{\dagger}_{1,k} c_{0,k'} + \text{H.c.}, \tag{5.14}$$

with $\mathcal{O}_{10} = \sum_{i=1}^{N_0} \sum_{j=1}^{N_1} t_1^{ij}(i\gamma_1^i\gamma_0^j)$ and an interference link $t_{0,1}$ between lead 1 and 0. For a Majorana qubit ($N_0 = N_1 = 1$) with interference links t_0 the current can take on two values [11]

$$\langle I_1 \rangle = 2\pi\nu^2 V(|t_{0,1}|^2 + |t_1^{11}|^2 + 2\mathrm{Re}(t_0^* t_1^{11})(i\gamma_1^1\gamma_0^1)) \tag{5.15}$$

defined by the eigenvalue of $i\gamma_1^1\gamma_0^1$ that can take on the values ±1. Note that the bias V needs to be finite in order to have a Pauli dependent current average. In the absence of the interference link, i.e. $t_{0,1} = 0$, the same current average $\langle I_1 \rangle = 2\pi\nu^2 |t_1^{11}|^2 V$ is measured in each iteration, irrespective of the state of the Majorana qubit. Now we have to address the fact that during the measurement the qubit has been projected to the corresponding eigenstate of $i\gamma_1^1\gamma_0^1$. Thus, a reset has to be carried out by changing the qubit state such that the subsequent projective measurement has a finite chance to yield all possible outcomes again. We achieve this by coupling lead 2 to one of the TSC ends on the other side of the box qubit (see Fig. 5.2), which is far separated. We assume lead 2 to be at the same potential as lead 1, such that a simultaneous average flow of the two currents I_1 and I_2 sets in. For genuine MBSs, the central island constitutes a Majorana qubit and the coupling of lead 2 implies that the evolution equation $\partial_t \rho_t = \mathit{\Gamma}\left[(i\gamma_1^1\gamma_0^1)\rho_t(i\gamma_1^1\gamma_0^1) - \rho_t\right] + \ldots$ for the reduced qubit density matrix ρ_t gets modified according to

$$\mathit{\Gamma}\left[(i\gamma_1^1\gamma_0^1)\rho_t(i\gamma_1^1\gamma_0^1) - \rho_t\right] \rightarrow \sum_{\alpha=1}^{2} \mathit{\Gamma}\left[(i\gamma_\alpha^1\gamma_0^1)\rho_t(i\gamma_\alpha^1\gamma_0^1) - \rho_t\right] \tag{5.16}$$

with $\mathit{\Gamma} \equiv 4\pi\nu^2|t_1|^2 V$. The additional decoherence term in Eq. (5.16) ensures that the state of the qubit cannot remain in an eigenstate of $\sigma_1 = i\gamma_1^1\gamma_0^1$. In fact, after a timescale $\tau_{\text{reset}} \equiv \mathit{\Gamma}^{-1}$ the qubit density matrix has approached the maximally mixed state $\rho_0 = \frac{1}{2}\sigma_0$, as discussed in Subsection 4.4.2. This means that after both currents have been flowing for some time, the observed average current is given by $\langle I_1 \rangle = 2\pi\nu^2 V(|t_{0,1}|^2 + |t_1^{11}|^2)$, as discussed in Subsection 4.4.2. Moreover, the shot noise S_{11} is increased according to Eq. (4.79), when both currents flow simultaneously. After some time, lead 2 gets decoupled and the projective measurement of I_1 has a finite chance of either of the two possible outcomes (5.15) again. In summary, we propose the following two-step protocol:

1. Measurement: The tunnel coupling λ_2 connecting drain 2 and the MBS γ_2 is turned off (e.g. controlled via a gate) and $\langle I_1 \rangle$ gets measured projectively resulting in a well defined (projective) average current (upper half of Fig. 5.2).
2. Reset of qubit state: To enable a next measurement which has again a finite probability to yield all the possible current outcomes, the drain 2 gets coupled such that the currents I_1 and I_2 flow simultaneously on average for a sufficient time $\tau > \Gamma^{-1}$ (bottom half of Fig. 5.2).

Hence, multiple repetitions of the two-step protocol for $t_{0,1} \neq 0$ allow to identify two different stable current averages for a genuine Majorana qubit, which do not change because the protocol leaves the relevant tunnel couplings unaffected.

On the other hand, in the case of ABSs the dimension of the Hilbert space spanned by the MBSs coupled to the two leads 0 and 1 is bigger. The projective current measurement can then result in more possible outcomes. Let us illustrate this for the case $N_0 = N_1 = 2$ where we simplify the discussion by assuming $t_{0,1}, t_1^{ij} \in \mathbb{R}$. In this case the current operator is given by

$$\langle I_1 \rangle = 2\pi\nu^2 V \left(t_{0,1}^2 + \sum_{i,j=1}^{2} \left[(t_1^{ij})^2 + 2t_{0,1} t_1^{ij} (i\gamma_0^i \gamma_1^j) \right] + 2(t_1^{21} t_1^{12} - t_1^{11} t_1^{22}) \gamma_0^1 \gamma_0^2 \gamma_1^1 \gamma_1^2 \right). \tag{5.17}$$

This current operator generically gives rise to four different current outcomes. If the interference link is switched off, $t_{0,1} = 0$, we have

$$\langle I_1 \rangle = V(g_1 + g_2 \gamma_0^1 \gamma_0^2 \gamma_1^1 \gamma_1^2), \tag{5.18}$$

where we define the dimensionless tunnel conductances $g_1 = 2\pi\nu^2 \sum_{i,j=1}^{2} (t_1^{ij})^2$ and $g_2 = 4\pi\nu^2 (t_1^{21} t_1^{12} - t_1^{11} t_1^{22})$. Since the quartic product of Majorana operators $\gamma_0^1 \gamma_0^2 \gamma_1^1 \gamma_1^2$ has the two possible eigenvalues ± 1 there are still two different outcomes, $\langle I_1 \rangle = V(g_1 \pm g_2)$. Hence, we can conclude that for ABSs we can have four outcomes in the presence of the interference path and two outcomes in its absence. Now we look at the cases $N_0 = 1, N_1 = 2$ and $N_0 = 2, N_1 = 1$, i.e. we ask whether a single additionally coupled

MBS can be detetced. We find that there is a single outcome for $t_{0,1} = 0$ and two outcomes for $t_{0,1} \neq 0$, just as in the case $N_\alpha = 1$ (see Appendix F). Thus, summarizing this discussion we arrive at the Table 5.2.

Number of MBSs coupled to lead $\boldsymbol{\alpha}$	$\boldsymbol{t_{0,1} \neq 0}$	$\boldsymbol{t_{0,1} = 0}$
$N_0 = N_1 = 1$	2 current outcomes	1 current outcome
$N_0 = 1, N_1 = 2$ or $N_0 = 2, N_1 = 1$	2 current outcomes	1 current outcome
$N_0 = N_1 = 2$	> 2 outcomes	> 1 outcome

Table 5.2: Projective current measurement of I_1 as a way to distinguish genuine MBSs from ABSs: By repeating the steps 1.) and 2.) outlined in the main text and Fig. 5.2, the number of outcomes can be obtained. There are qualitative differences in this number, which enable the distinction. The first row shows the result consistent with single MBSs coupled to the leads 0 and 1. If more different outcomes are observed, the presence of ABS can be inferred (third row) and the device is not a Majorana box qubit. However, the number of outcomes is blind to a single additional MBS, see second row.

The number of current outcomes differs qualitatively, when step 1.) and 2.) are iterated many times, depending on whether the source lead 0 and the drain lead 1 are each coupled to single MBSs or ABSs. In particular, one should repeat the two stages multiple times for a single device with and without the interference link connecting leads 0 and 1. When more different current outcomes than predicted for MBSs can be identified, the presence of ABSs can be inferred (see Table 5.2). Importantly, the couplings λ_0^j and λ_1^j (see Fig. 5.2) stay unchanged throughout the protocol since only the amplitudes λ_2^j get tuned e.g. via gating, which means that the value of the current average for a given state is indeed unaffected.

The time scale for which the projective measurement has to be conducted to identify an outcome can be estimated by the time

$$\tau_{\text{proj}} \simeq \frac{\langle I_1 \rangle}{(\Delta I)^2} \tag{5.19}$$

it takes to reach a signal to noise ratio of order unity. Here we made use of the fact that the noise S_{11} is given by the Schottky formula, $S_{11} = \langle I_1 \rangle$. The quantity ΔI represents the difference in the current outcomes, which can be nearly degenerate in highly fine tuned situations. For the example given in Eq. (5.18), we have $\Delta I = 2g_2 V$. For a Majorana qubit, $N_0 = N_1 = 1$, the difference in currents is $\Delta I = 8\pi\nu^2 V \text{Re}(t_{0,1}^* t_1)$ leading to the timescale $\tau_{\text{proj}} \simeq (|t_{0,1}|^2 + |t_1|^2)/(32\pi \left[\text{Re}(t_{0,1}^* t_1)\right]^2 V)$.

5.3 Conclusions and outlook

In this chapter, we introduced two further protocols geared to identify genuine MBSs in topological SC wires. The first is a current cross-correlation measurement protocol for a Coulomb blockaded Majorana quantum wire with three tunnel coupled terminals. The second is a projective conductance measurement protocol based on the number of distinct current outcomes. In the following, we discuss these two experimental protocols and compare them with each other, as well as with the weak simultaneous measurement protocol of noncommuting Pauli operators presented in Chapter 4. We argue that the latter is more desirable to be executed, because it yields more information related to the fundamental nature of MBSs.

The first detection protocol of Majorana qubits presented in Section 5.1 leads to strong observable differences distinguishing genuine MBSs and ABSs that are coupled to the respective leads. The main advantage of the protocol is its ability to rule out ABSs based on the observation of $|F| = \mathcal{O}(1)$. However, observing the signature $F \ll 1$ is merely consistent with MBSs but does not contain a direct signature of the Majorana states. This is because for a setting of non-interacting electrons, F is suppressed as well. Thus, observation of $F \ll 1$ has to be interpreted as a result that is consistent with MBSs, which implies that not more than single MBSs are coupled to the respective leads. In this sense, the information gained is not comparable to the protocol presented in Chapter 4. Nevertheless, it is useful to rule out multiple MBSs coupled to the drain leads.

A new feature of the second protocol discussed in Section 5.2 is the alternation of two stages as displayed in Fig. 5.2. This addresses the fact that after a projective measurement of a single current a reset of the qubit state is necessary. We achieve this reset by temporarily coupling a second drain lead to another MBS on the box, resulting in the simultaneous flow of the two currents I_1 and I_2. We emphasize that the experimental demonstration of this reset procedure reveals evidence of noncommuting degrees of freedom on the box. This is because of the way that the average of the current I_1 and its noise level is affected depending on whether I_2 is flowing or not. The main shortcoming of the protocol is that the number of outcomes for the cases $N_0 = 1, N_1 = 2$ and $N_0 = 2, N_1 = 1$ is the same as for $N_0 = N_1 = 1$. In contrast, the protocol outlined in Chapter 4 can clearly identify single MBSs. We also emphasize that the current outcomes are obtained under the same conditions (density of states, shape of the contacts, etc.) and that constant contributions to the current due to quasiparticles are always present in each measurement iteration. For the protocol of Section 5.2, the timescale τ_{proj} (see Eq. (5.19)), on which the current measurement can be considered to be projective, must be shorter than the typical time scale after which a quasiparticle poisoning event takes place. Those events could either occur due to thermal excitation or due to a tunneling event from outside the island. Quasiparticle poisoning events would cause a flip of the Pauli operator and hence a jump in the average of the noisy current signal. Therefore, the applied bias must be large enough such that τ_{proj} is shorter than the characteristic timescale of both of these quasiparticle poisoning processes.

Finally, we can draw the following conclusion regarding the MBS detection: When the three detection protocols presented in this dissertation are compared, the simultaneous weak measurement approach of noncommuting operators described in Chapter 4 yields the most information about the fundamental nature of MBSs. Hence, it is the most desirable approach when it comes to practical implementation.

Chapter 6

Overall conclusion and outlook

Improvements in the ability to more accurately manufacture and control quantum devices are likely to lead to disruptive technological developments. The Majorana bound state has been pursued in topological SCs for a number of years now, but its unambiguous confirmation has proven to be a particularly challenging task up to this day. An attractive application of the Majorana state is the Majorana qubit, but, so far, no functional device of this kind has been realized in the laboratory. In this thesis, we have addressed this situation and studied the Majorana qubit in a two-fold way: Firstly, by a thorough investigation of new TI nanoribbon architectures of Majorana qubits as alternatives to the qubit architectures based on semiconductors in Chapter 3. And secondly, by proposing new experimental methods and corresponding observable predictions to perform the identification of Majorana qubits in Chapters 4 and 5.

As shown in Chapter 3, Majorana qubit architectures building on proximitized TI nanowire segments of differing width promise to represent a suitable and flexible platform with robust Majorana states. The manipulation of local electrochemical potentials in these systems allows to control the coupling of pairs of MBSs. In Chapters 4 and 5, three methods have been put forward and studied theoretically in detail. The protocol of simultaneous weak measurement of noncommuting operators presented in Section 4.6 enables to identify the Majorana qubit devices with single MBSs and allows to extract a clear signature of the nonlocal Pauli algebra. This is a clear advantage and makes this protocol more efficacious than the two methods put forward in Chapter 5. In that chapter, we found that measuring the shot noise in a setting with three leads and a single Majorana quantum wire can be used to rule out more than a single MBS at the wire ends. However, for a genuine Majorana wire no direct signature of the MBSs is accessed in this way. In contrast, the protocol of simultaneous weak measurement of noncommuting operators presented in Section 4.6 clearly allows to extract a direct signature of genuine MBSs. Hence, the latter represents the more desirable goal that would clearly constitute experimental progress in the pursuit of the Majorana state. Due to the accessibility of the necessary hardware, the milestone of establishing that a given quantum device is a genuine Majorana qubit is realistically achievable in the near term future. This quantum device could be engineered using TI nanoribbons as outlined in Chapter 3, it could be made of the semiconducting wires that are studied in several laboratories around the world, or it could be based on any other physical platform in which zero-dimensional Majorana states are predicted. The experiments have to be carried out in the Coulomb blockade regime at low temperatures and in the tunneling limit. Here, one must not underestimate the task of shot noise measurement in nanoscale systems where electrons pass the tunneling barriers individually. Nevertheless, one could argue that the protocol of Section 4.6 represents the most viable option to identify Majorana states and the nonlocal Pauli algebra of the Majorana qubit from the operational and practical standpoint. Successful observation of the predicted Majorana signature would provide further impetus to move on to realize full braiding protocols, whose completion would constitute a remarkable breakthrough for fundamental science.

Once under full control, the Majorana qubit becomes a building block for higher-level applications and further experiments. For instance, it would be noteworthy to realize a Majorana surface code [86, 87, 88], which is a two-dimensional network structure as briefly discussed in Section 3.4. In conclusion, we anticipate that this work will stimulate much needed experimental and theoretical progress in the field and bring us closer to Majorana based quantum computation.

Appendices

Appendix A: Analysis of spinor wave functions

This part of the appendix provides additional details on the derivation of the results presented in Chapter 3. To keep the formulas compact, we work in units with $\hbar v_1 = 1$. We start by providing the explicit form of the eigenstates of the BdG Hamiltonian (3.12),

$$\Psi(z) = \begin{cases} \Psi_L(z)\ ,\ z \leq -W/2, \\ \Psi_C(z)\ , |z| \leq W/2, \\ \Psi_R(z)\ ,\ z \geq +W/2, \end{cases} \tag{6.1}$$

for the Majorana qubit platform shown in Fig. 3.3. Since we are interested in constructing Majorana bound states, we only consider energies below the superconducting gap, $|E| < \Delta$. We shall first write down general solutions of the BdG equation in each of the three regions defined by the constriction length W. Using parameters $A_{1,2}^{(\pm)}$, the solution for $|z| > W/2$ vanishing exponentially at $|z| \to \infty$ reads

$$\Psi_L(z) = e^{-\sqrt{\Delta^2 - E^2}|z|} \left[A_1^{(-)} \begin{pmatrix} E \\ \sqrt{\Delta^2 - E^2} \\ 0 \\ \Delta e^{-i\phi/2} \end{pmatrix} + A_2^{(-)} \begin{pmatrix} \sqrt{\Delta^2 - E^2} \\ -E \\ \Delta e^{-i\phi/2} \\ 0 \end{pmatrix} \right], \tag{6.2}$$

$$\Psi_R(z) = e^{-\sqrt{\Delta^2 - E^2}|z|} \left[A_1^{(+)} \begin{pmatrix} E \\ -\sqrt{\Delta^2 - E^2} \\ 0 \\ \Delta e^{i\phi/2} \end{pmatrix} + A_2^{(+)} \begin{pmatrix} -\sqrt{\Delta^2 - E^2} \\ -E \\ \Delta e^{i\phi/2} \\ 0 \end{pmatrix} \right], \tag{6.3}$$

where the first and second (third and fourth) component refers to the spin structure of the particle (hole) part of the Nambu spinor. In the central region $|z| < W/2$ and with coefficients $B_{1,2}^{(\pm)}$, the solution is given by

$$\begin{aligned}\Psi_C(z) &= e^{\sqrt{M_0^2-(E+\mu)^2}z} B_1^{(+)} \boldsymbol{u}_+(E) + e^{-\sqrt{M_0^2-(E+\mu)^2}z} B_1^{(-)} \boldsymbol{u}_-(E) \\ &\quad + e^{\sqrt{M_0^2-(E-\mu)^2}z} B_2^{(+)} \boldsymbol{v}_+(E) + e^{-\sqrt{M_0^2-(E-\mu)^2}z} B_2^{(-)} \boldsymbol{v}_-(E), \qquad (6.4)\end{aligned}$$

with

$$\boldsymbol{u}_\pm(E) = \begin{pmatrix} \pm(M_0+E+\mu) \\ \sqrt{M_0^2-(E+\mu)^2} \\ 0 \\ 0 \end{pmatrix}, \qquad \boldsymbol{v}_\pm(E) = \begin{pmatrix} 0 \\ 0 \\ \pm(M_0-E+\mu) \\ \sqrt{M_0^2-(E-\mu)^2} \end{pmatrix}. \qquad (6.5)$$

Now one has to demand continuity of the spinor wave functions at the points $z = \pm W/2$, which translates into the conditions $\Psi_L(-W/2) = \Psi_C(-W/2)$ and $\Psi_C(W/2) = \Psi_R(W/2)$. For eigenenergies with $|E| < \min(\Delta, M_0)$ these conditions can be cast into a zero-determinant condition

$$D(E) = 0. \qquad (6.6)$$

Here the corresponding determinant reads

$$\begin{aligned}D(E) &= \sum_\pm \left[(2E^2-\Delta^2)\left(a_+a_- \pm \mu^2 \mp E^2\right) \pm M_0^2\Delta^2\right] \cosh[(a_- \pm a_+)W] \\ &\quad + 2E\sqrt{\Delta^2-E^2} \sum_\pm \left[(E-\mu)a_+ \pm (E+\mu)a_-\right] \sinh[(a_- \pm a_+)W] \\ &\quad - 2\Delta^2 a_+ a_- \cos\phi, \qquad (6.7)\end{aligned}$$

with

$$a_\pm(E) \equiv \sqrt{M_0^2-(E\pm\mu)^2}. \qquad (6.8)$$

The determinant $D(E)$ is a symmetric function of energy, i.e. $D(E) = D(-E)$, as required by the particle hole symmetry of the superconductor. A robust feature found by solving the Eq. (6.6) is the presence of subgap state solutions at

$$E = \pm\varepsilon. \qquad (6.9)$$

Under the self consistent condition $|\varepsilon| \ll \min(\Delta, M_0)$, we expand $D(E)$ up to second order in E. For this we use the relation

$$a_+(E)a_-(E) = M_0^2 - \mu^2 - \frac{M_0^2 + \mu^2}{M_0^2 - \mu^2}E^2 + \mathcal{O}\left(E^4\right) \tag{6.10}$$

and obtain

$$\begin{aligned} D(E) = &- 4(\hbar v_1/\xi)^2\Delta^2\cos^2(\phi/2) + 2E^2(\hbar v_1/\xi)^{-2}\left[M_0^4 + \Delta^2(\mu^2 + 2W^2\mu^4)\right. \\ &- M_0^2(3 + 2W^2\Delta^2 + 4W\Delta)\mu^2 + 2(1 + 2W\Delta)\mu^4 + \Delta^2(M_0^2 + \mu^2)\cos(\phi) \\ &\left.+ M_0^2(\Delta^2 + (\hbar v_1/\xi)^2)\cosh(2W/\xi) + 2M_0^2\Delta(\hbar v_1/\xi)\sinh(2W/\xi)\right] + \mathcal{O}\left(E^4\right). \end{aligned} \tag{6.11}$$

Assuming $W \gg \xi$ we obtain the following explicit expressions for the energies of the above mentioned subgap states as

$$\begin{aligned} \varepsilon &= \frac{\sqrt{2}(\hbar v_1/\xi)^2\Delta\cos(\phi/2)}{M_0\sqrt{(\Delta^2 + (\hbar v_1/\xi)^2)\cosh(2W/\xi) + 2\Delta(\hbar v_1/\xi)\sinh(2W/\xi)}} \\ &\simeq \cos\left(\frac{\phi}{2}\right)\frac{2\Delta}{M_0}\frac{(\hbar v_1/\xi)^2}{\Delta + \hbar v_1/\xi}e^{-W/\xi}. \end{aligned} \tag{6.12}$$

This concludes the derivation of the hybridization formula Eq. (3.28).

Appendix B: Effective tunnel Hamiltonian of three-terminal device

This part of the appendix provides details on the derivation of the effective Hamiltonian (4.14) presented in Section 4.2. The series expansion for the effective tunneling Hamiltonian is given by [96]

$$H_{\text{eff}} \equiv \sum_{n=1}^{\infty} H_{\text{eff}}^{(n)} = \sum_{n=1}^{\infty} P_0 H_{\text{T}} \left(\frac{1}{-H_C} H_{\text{T}} \right)^{n-1} P_0, \tag{6.13}$$

where H_C is the charging Hamiltonian and P_0 is the projection operator onto the definite charge ground state $|N_0\rangle$ (see below). Furthermore, the microscopic tunneling is described by

$$H_{\text{T}} = \sum_{\alpha=0}^{2} \sum_{k} \sum_{j=1}^{N_\alpha} \lambda_\alpha^j c_{\alpha,k}^\dagger \gamma_\alpha^j e^{-i\phi/2} + \text{H.c.}. \tag{6.14}$$

This perturbative procedure $H_C + H_{\text{T}} \to H_{\text{eff}}$ is valid in the weak tunneling limit $\lambda_\alpha^i \ll \Delta, E_C$. Similar Hamiltonians have been previously derived, see Refs. [29, 30, 87, 88]. The Hamiltonian H_C has the eigenvalues $E(N) = E_c(N - n_g)^2$ with N the number of island electrons and we assume to be far away from the charge degeneracy points $n_g \in \left(\mathbb{Z} + \frac{1}{2}\right)$. Then, the ground state has a definite charge which we denote by N_0. We take into account fluctuations to the sectors of higher energy defined by the charge states $N_0 \pm 1$. In the same way as in Ref. [30], we define the energy differences $E_\pm = E(N_0 \pm 1) - E(N_0)$. Since the operator $e^{i\phi/2}$ causes the addition of an electron on the island, it follows that the first order contribution in the series 6.13 vanishes, i.e. $H_{\text{eff}}^{(1)} = P_0 H_{\text{T}} P_0 = 0$. The first non-vanishing contribution is $H_{\text{eff}}^{(2)}$ and gives

$$\begin{aligned} H_{\text{eff}}^{(2)} &= P_0 H_{\text{T}} \left(\frac{1}{-H_C} H_{\text{T}} \right) P_0 \\ &= -\sum_{k,k'} \sum_{\alpha,\alpha'=0}^{2} \sum_{j=1}^{N_\alpha} \sum_{j'=1}^{N_{\alpha'}} \Bigg(P_0 \lambda_\alpha^j c_{\alpha,k}^\dagger \gamma_\alpha^j e^{-i\phi/2} \frac{\lambda_\alpha^j (\lambda_{\alpha'}^{j'})^*}{E_-} e^{i\phi/2} \gamma_{\alpha'}^{j'} c_{\alpha',k'} P_0 \\ &\quad + P_0 e^{i\phi/2} \gamma_{\alpha'}^{j'} c_{\alpha',k'} \frac{(\lambda_{\alpha'}^{j'})^* \lambda_\alpha^j}{E_+} c_{\alpha,k'}^\dagger \gamma_\alpha^j e^{-i\phi/2} P_0 \Bigg) + \text{H.c.}. \end{aligned} \tag{6.15}$$

We may write

$$H_{\text{eff}} = H_{\text{eff}}^{(2)} + \mathcal{O}\left(E_C^{-2}\left|\lambda_\alpha^j\right|^3\right). \tag{6.16}$$

Therefore, the higher order terms are strongly suppressed in the limit of interest. We split the effective Hamiltonian (6.15) into three different types of terms,

$$H_{\text{eff}}^{(2)} \equiv \tilde{H}_{\text{T}} + \tilde{H}_L + \tilde{H}_{ABS}. \tag{6.17}$$

The first type arises from contributions with $\alpha \neq \alpha'$ and leads to tunneling terms connecting the leads α and α'. The corresponding Hamiltonian term reads

$$\tilde{H}_{\text{T}} = \sum_{k,k'}\sum_{\alpha\neq\alpha'}\sum_{j=1}^{N_\alpha}\sum_{j'=1}^{N_{\alpha'}} \frac{i\lambda_\alpha^j(\lambda_{\alpha'}^{j'})^*(E_+ + E_-)}{E_+E_-}(i\gamma_\alpha^j\gamma_{\alpha'}^{j'})c_{\alpha,k}^\dagger c_{\alpha',k'} + \text{H.c.}. \tag{6.18}$$

The effective amplitude for the single electron tunneling processes from α' to α is given by

$$\begin{aligned} t_{1,\alpha\alpha'}^{jj'} &= i\lambda_\alpha^j(\lambda_{\alpha'}^{j'})^*\frac{E_+ + E_-}{E_+E_-} \\ &= \frac{2i\lambda_\alpha^j(\lambda_{\alpha'}^{j'})^*}{E_C(1-4\Delta n_g)} \\ &\simeq 2i\frac{\lambda_\alpha^j(\lambda_{\alpha'}^{j'})^*}{E_C}, \end{aligned} \tag{6.19}$$

where we have used the assumption $|N_0 - n_g| \ll 1$ and thus arrive at the Hamiltonian stated in Eq. (4.14). These second order cotunneling processes, where electrons tunnel in and out at different terminals, are the most relevant for our purposes. For completeness, we mention the two other types of processes: First, for $\alpha = \alpha'$ and $j = j'$ the term $\tilde{H}_L$ up to a constant reads

$$\tilde{H}_L = \sum_{k,k'}\sum_{\alpha=0}^{2}\sum_{i=1}^{N_\alpha} \frac{\left|\lambda_\alpha^i\right|^2(E_- - E_+)}{E_+E_-}c_{\alpha,k}^\dagger c_{\alpha,k'} + \text{H.c.} \tag{6.20}$$

and renormalizes the lead potentials. This renormalization of the leads vanishes for $n_g \in \mathbb{Z}$. Physically, this term originates in the process in which an electron tunnels from the lead into γ_α^i and subsequently from the same MBS back into the same lead. Second, there is a type of term that is only present for Andreev bound states. It originates in processes where an electron tunneling into an island MBS is accompanied by an electron tunneling back into the same lead from a different MBS, i.e. contributions with $\alpha = \alpha'$ and $j \neq j'$:

$$\tilde{H}_{ABS} = \sum_{k,k'} \sum_{\alpha=0}^{2} \sum_{j \neq j'} \lambda_{\alpha}^{j} (\lambda_{\alpha}^{j'})^{*} \gamma_{\alpha}^{j} \gamma_{\alpha}^{j'} \left[E_{+}^{-1} c_{\alpha,k'} c_{\alpha,k}^{\dagger} - E_{-}^{-1} c_{\alpha,k}^{\dagger} c_{\alpha,k'} \right] + \text{H.c.}. \tag{6.21}$$

After tracing out the leads, these terms weakly renormalize the energy of the ABSs, which does not affect the qualitative conclusions drawn in the counting statistics calculations as shown in Appendix E.

Appendix C: Further details on the derivation of the master equation

In this part of the appendix, we provide further details on the derivation of the Bloch Redfield equation supplementing the Subsections (4.3.3) and (4.3.4). In the procedure of integrating out the lead degrees of freedom, one is confronted with expressions like

$$\int\limits_0^\infty ds \mathrm{Tr}\left(\rho_{\mathrm{L}} Q_{\alpha 0}(t-s) Q^\dagger_{\alpha 0}(t)\right) = \nu^2 \iint d\varepsilon d\omega n_F(\varepsilon)\left[1-n_F(\varepsilon+\omega-V)\right] \int\limits_0^\infty ds e^{i\omega s}, \tag{6.22}$$

with $Q_{\alpha\beta} = \sum_{k,k'} c^\dagger_{\alpha,k} c_{\beta,k'}$. To make progress, we use the relation

$$\int\limits_0^\infty ds e^{i\omega s} = \pi\delta(\omega) + \mathrm{p.v.}(\frac{i}{\omega}), \tag{6.23}$$

where "p.v." refers to the Cauchy principal value. The finite temperature integrals

$$\int d\varepsilon n_F(\varepsilon)\left[1-n_F(\varepsilon+\omega)\right] = \omega\theta(\omega) + |\omega|\, n_B(|\omega|) \tag{6.24}$$

and

$$\int d\varepsilon \left[n_F(\varepsilon) - n_F(\varepsilon+\omega)\right] = \omega \tag{6.25}$$

are useful as well for dealing with expressions like the one stated in Eq. (6.22). This results in the exemplary relations (4.52), (4.53) and (4.54) stated in the main text. Moreover, one obtains the following term which contributes to the "Lamb shift" (4.59) in the Bloch Redfield Eq. (4.58):

$$\int ds \mathrm{Tr}\left(\rho_{\mathrm{Leads}}(Q^\dagger_{\alpha 0}(t-s) Q_{\alpha 0}(t) - Q_{\alpha 0}(t) Q^\dagger_{\alpha 0}(t-s))\right) = \nu^2(i\Lambda + \pi V). \tag{6.26}$$

The terms proportional to the bias in the Bloch Redfield Eq. (4.58) arise from

$$\int ds \mathrm{Tr}\left(\rho_{\mathrm{Leads}}(Q^\dagger_{\alpha 0}(t) Q_{\alpha 0}(t-s) + Q^\dagger_{\alpha 0}(t-s) Q_{\alpha 0}(t))\right) = 2\pi\nu^2 V(1+n_B(V)), \tag{6.27}$$

where $n_B(V)$ is the Bose function which is negligible in the limit $T \ll V$. Terms proportional to temperature in the Bloch Redfield equation arise from

$$\int ds \mathrm{Tr}\left(\rho_{\mathrm{Leads}}(Q^\dagger_{12}(t)Q_{12}(t-s)+Q^\dagger_{12}(t-s)Q_{12}(t))\right) = 2\pi\nu^2 T. \tag{6.28}$$

The Hamiltonian H_q generating the unitary evolution term in the Markovian Master Eq. (4.58) in the limit $T \ll V \ll \Lambda$ is derived by noting that we can neglect the expression

$$\begin{aligned} \text{p.v.}\int d\omega \frac{|\omega - V|}{\omega} n_B(|\omega - V|) &\simeq \text{p.v.}\int_0^\infty d\omega \left(\frac{\omega}{V+\omega} + \frac{\omega}{V-\omega}\right) n_B(\omega) \\ &\simeq \frac{2T^2}{V}\int_0^\infty dx \frac{x}{e^x - 1} \simeq 3.29\frac{T^2}{V}. \end{aligned} \tag{6.29}$$

Therefore, the contributions to the Hamiltonian evolution term in the Bloch Redfield equation for $t_0 = 0$ arise from terms such as

$$\begin{aligned} \frac{\partial}{\partial t}\rho &= i\nu^2 \iint d\varepsilon d\omega \left([\mathcal{O}_{\alpha0}\mathcal{O}^\dagger_{\alpha0}, \rho]\frac{n_F(\varepsilon)\left[1 - n_F(\varepsilon+\omega-V)\right]}{\omega} \right. \\ &\quad \left. -[\mathcal{O}^\dagger_{\alpha0}\mathcal{O}_{\alpha0}, \rho]\frac{n_F(\varepsilon+\omega-V)\left[1-n_F(\varepsilon)\right]}{\omega}\right) + \ldots \\ &= i\nu^2 \int d\omega \left([\mathcal{O}_{\alpha0}\mathcal{O}^\dagger_{\alpha0}, \rho]\frac{\omega - V}{\omega}\theta(\omega - V) \right. \\ &\quad \left. +[\mathcal{O}^\dagger_{\alpha0}\mathcal{O}_{\alpha0}, \rho]\frac{\omega - V}{\omega}\theta(-\omega + V)\right) + \ldots \\ &= i\frac{\nu^2\Lambda}{2}[\{\mathcal{O}^\dagger_{\alpha0}, \mathcal{O}_{\alpha0}\}, \rho] - i\nu^2 V(1+\ln(\Lambda/2V))\sum_{\alpha=1}^{2}[[\mathcal{O}_{\alpha0}, \mathcal{O}^\dagger_{\alpha0}], \rho] + \ldots \end{aligned} \tag{6.30}$$

Thus, the Hamiltonian evolution in the master equation is generated by

$$\begin{aligned} H_q &= -\nu^2\sum_{\alpha=1}^{2}((\Lambda - i\pi V)t_0^*\mathcal{O}_{\alpha0} + \mathrm{H.c.}) - \frac{\nu^2\Lambda}{2}\sum_{\alpha<\beta}\{\mathcal{O}^\dagger_{\alpha\beta}, \mathcal{O}_{\alpha\beta}\} \\ &\quad +\nu^2 V(1+\ln(\Lambda/2V))\sum_{\alpha=1}^{2}[\mathcal{O}_{\alpha0}, \mathcal{O}^\dagger_{\alpha0}], \end{aligned} \tag{6.31}$$

which in the limit $V \ll \Lambda$ leads to the Hamiltonian (4.58) stated in the main text.

Appendix D: Counting statistics for Majorana box qubit

Appendix D provides additional details on the derivation of Eq. (4.64) from the evolution Eq. (4.60) stated in Section 4.4. Starting from the parametrization $\rho = \sum_{\mu=0}^{3} \rho_\mu \sigma_\mu$, we rewrite the right hand side of Eq. (4.60). The decoherence term can be cast in the form

$$\begin{aligned} \sum_{\alpha>\alpha'} \frac{\tilde{\mathit{\Gamma}}_{\alpha\alpha'}}{2} \left((i\gamma_\alpha\gamma_{\alpha'})\tilde{\rho}_t(i\gamma_\alpha\gamma_{\alpha'}) - \tilde{\rho}_t\right) &= -(\tilde{\mathit{\Gamma}}_{20} + \tilde{\mathit{\Gamma}}_{21})\rho_1\sigma_1 - (\tilde{\mathit{\Gamma}}_{10} + \tilde{\mathit{\Gamma}}_{21})\rho_2\sigma_2 \\ &\quad -(\tilde{\mathit{\Gamma}}_{10} + \tilde{\mathit{\Gamma}}_{20})\rho_3\sigma_3. \end{aligned} \tag{6.32}$$

Using

$$t_0^* t_1 \sigma_\alpha \tilde{\rho}_t + t_0 t_1^* \tilde{\rho}_t \sigma_\alpha = \mathrm{Re}(t_0^* t_1)\left\{\sigma_\alpha, \tilde{\rho}_t\right\} + i\mathrm{Im}(t_0^* t_1)\left[\sigma_\alpha, \tilde{\rho}_t\right], \tag{6.33}$$

we see that the remaining terms are commutator and anticommutator terms. The former can be written as

$$-i\sum_{k=1}^{3}[h_k\sigma_k, \rho] = 2\sum_{k,l,m=1}^{3} \epsilon_{klm} h_k \rho_l \sigma_m, \tag{6.34}$$

while the latter obey

$$\sum_k \frac{\Omega_k}{2}\{\sigma_k, \rho\} = \rho_0 \sum_k \Omega_k \sigma_k + \sum_k \Omega_k \rho_k \sigma_0. \tag{6.35}$$

By combining these relations, we obtain the matrix elements $\Omega_{\mu\nu}$ as given by Eq. (4.65). We now derive the Eqs. (4.90) and (4.91) showing the effect of the inclusion of a finite hybridization

$$\tilde{H}_q \rightarrow \tilde{H}_q + \varepsilon_3\sigma_3 \tag{6.36}$$

on the current cross-correlations. The inclusion of this term leads to the modification $\mathit{\Omega} \rightarrow \tilde{\mathit{\Omega}}$ of the matrix given in Eq. (4.65) with

$$\tilde{\Omega} = \begin{pmatrix} 0 & a_1 & a_2 & 0 \\ a_1 & -\tilde{\mathit{\Gamma}}_{20} - \tilde{\mathit{\Gamma}}_{21} & 2\varepsilon_3 & h_2 \\ a_2 & -2\varepsilon_3 & -\tilde{\mathit{\Gamma}}_{10} - \tilde{\mathit{\Gamma}}_{21} & -h_1 \\ 0 & -h_2 & h_1 & -\tilde{\mathit{\Gamma}}_{10} - \tilde{\mathit{\Gamma}}_{20} \end{pmatrix}. \tag{6.37}$$

Here, ε_3 is defined as in Eq. (6.36) and $a_\alpha = 4\pi V \nu^2 \mathrm{Re}(t_0^* t_1)(z_\alpha - 1)$, $h_\alpha = -4\nu^2 \Lambda \mathrm{Re}(t_0^* t_1) - 4\pi\nu^2 V \mathrm{Im}(t_0^* t_1) e^{i\chi_\alpha}$. The Fano factor derived from the corresponding evolution equation defined by $\tilde{\Omega}$ is given by

$$F' = \frac{2\Lambda^2 \nu^4 \left[\mathrm{Re}(t_0^* t_1)\right]^4}{\left(\Lambda^2 \left[\nu^2 \mathrm{Re}(t_0^* t_1)\right]^2 + \varepsilon_3^2\right) |t_1|^2 \left(|t_0|^2 + |t_1|^2\right)}, \tag{6.38}$$

which coincides with the result stated in Eq. (4.90) in Subsection 4.4.5.

Appendix E: Counting statistics for ABSs

This part of the appendix is focused on giving additional details on the derivation of the results presented in Section 4.5. To solve the Bloch Redfield Eq. (4.93), we use Pauli matrices to parametrize the density matrix as

$$\rho = \sum_{\mu=0}^{3} \sum_{\nu=0}^{3} \sum_{\lambda=0}^{3} \rho_{\mu\nu\lambda} \sigma_\mu \otimes \sigma_\nu \otimes \sigma_\lambda. \tag{6.39}$$

The density matrix is defined in the eight-dimensional Hilbert space corresponding to three fermions. There are two MBSs γ_α^1 and γ_α^2 coupled to each lead α. We choose the following matrix representation of the resulting Majorana bilinears:

$$\begin{aligned}
&i\gamma_1^1\gamma_0^1 = \sigma_0 \otimes \sigma_1 \otimes \sigma_0, && i\gamma_2^1\gamma_0^1 = \sigma_2 \otimes \sigma_2 \otimes \sigma_0, && i\gamma_1^2\gamma_1^1 = \sigma_0 \otimes \sigma_2 \otimes \sigma_2,\\
&i\gamma_0^1\gamma_1^2 = \sigma_0 \otimes \sigma_3 \otimes \sigma_2, && i\gamma_0^1\gamma_2^2 = \sigma_1 \otimes \sigma_2 \otimes \sigma_0, && i\gamma_0^1\gamma_0^2 = \sigma_3 \otimes \sigma_2 \otimes \sigma_0,\\
&i\gamma_1^1\gamma_0^2 = \sigma_3 \otimes \sigma_3 \otimes \sigma_0, && i\gamma_2^1\gamma_0^2 = \sigma_1 \otimes \sigma_0 \otimes \sigma_0, && i\gamma_2^2\gamma_2^1 = \sigma_3 \otimes \sigma_0 \otimes \sigma_0,\\
&i\gamma_1^2\gamma_0^2 = \sigma_3 \otimes \sigma_1 \otimes \sigma_2, && i\gamma_2^2\gamma_0^2 = \sigma_2 \otimes \sigma_0 \otimes \sigma_0.
\end{aligned} \tag{6.40}$$

The products of four and six Majorana operators are then expressed by the matrices

$$\begin{aligned}
\gamma_1^1\gamma_1^2\gamma_0^1\gamma_0^2 &= \sigma_3 \otimes \sigma_0 \otimes \sigma_2,\\
\gamma_2^1\gamma_2^2\gamma_0^1\gamma_0^2 &= \sigma_0 \otimes \sigma_2 \otimes \sigma_0,\\
\gamma_1^1\gamma_1^2\gamma_2^1\gamma_2^2 &= -\sigma_3 \otimes \sigma_2 \otimes \sigma_2.
\end{aligned} \tag{6.41}$$

For the product of all six Majorana operators we have

$$i\gamma_0^1\gamma_0^2\gamma_1^1\gamma_1^2\gamma_2^1\gamma_2^2 = -\sigma_0 \otimes \sigma_0 \otimes \sigma_2. \tag{6.42}$$

The counting statistics follows from the trace of the generalized density matrix, which is given by $\mathrm{Tr}_q\left(\rho_\tau(\chi_1, \chi_2)\right) = 8\rho_{000,\tau}(\chi_1, \chi_2)$. This implies that soley the element $\rho_{000,t}$ is important, which as we will see couples only to some of the other elements $\rho_{\mu\nu\lambda,t}$. To express the Bloch Redfield equation in this parametrization of the density matrix, we use relations of the following type (omitting the $\otimes$-symbols for brevity) for the anticommutators,

$$\begin{aligned}\{\gamma_1^1\gamma_1^2,\rho\} &= 2(-\rho_{000}\sigma_0\sigma_2\sigma_2-\rho_{022}\sigma_0\sigma_0\sigma_0-\rho_{300}\sigma_3\sigma_2\sigma_2-\rho_{322}\sigma_3\sigma_0\sigma_0-\rho_{020}\sigma_0\sigma_0\sigma_2\\ &\quad -\rho_{002}\sigma_0\sigma_2\sigma_0-\rho_{302}\sigma_3\sigma_2\sigma_0-\rho_{320}\sigma_3\sigma_0\sigma_2+\dots\,, \qquad (6.43)\end{aligned}$$

$$\begin{aligned}\{\gamma_2^1\gamma_2^2\gamma_0^1\gamma_0^2,\rho\} &= 2(\rho_{000}\sigma_0\sigma_2\sigma_0+\rho_{020}\sigma_0\sigma_0\sigma_0+\rho_{300}\sigma_3\sigma_2\sigma_0+\rho_{320}\sigma_3\sigma_0\sigma_0+\rho_{322}\sigma_3\sigma_0\sigma_2\\ &\quad +\rho_{302}\sigma_3\sigma_2\sigma_2+\rho_{022}\sigma_0\sigma_0\sigma_2+\rho_{002}\sigma_0\sigma_2\sigma_2+\dots\,. \qquad (6.44)\end{aligned}$$

Furthermore, we make use of relations like

$$\begin{aligned}(i\gamma_2^1\gamma_0^1)\tilde{\rho}(i\gamma_2^1\gamma_0^2)-(i\gamma_2^1\gamma_0^2)\tilde{\rho}(i\gamma_2^1\gamma_0^1) &= 2i(-\rho_{000}\sigma_3\sigma_2\sigma_0+\rho_{320}\sigma_0\sigma_0\sigma_0+\rho_{300}\sigma_0\sigma_2\sigma_0\\ &\quad -\rho_{020}\sigma_3\sigma_0\sigma_0+\rho_{322}\sigma_0\sigma_0\sigma_2-\rho_{002}\sigma_3\sigma_2\sigma_2\\ &\quad -\rho_{022}\sigma_3\sigma_0\sigma_2+\rho_{302}\sigma_0\sigma_2\sigma_2+\dots\,. \qquad (6.45)\end{aligned}$$

In analogy to our analytical treatment of the Majorana box qubit, it is convenient to reparametrize the time variable according to $\rho_t = e^{\theta t}\tilde{\rho}_t$ with

$$\theta = 2\pi\nu^2 V\sum_{\alpha=1}^{2}\sum_{i,j=1}^{2}|t_{\alpha0}^{ij}|^2(e^{i\chi_\alpha}-1). \qquad (6.46)$$

For $N_\alpha = 2$ without interference links, $t_0 = 0$, we find that the element $\rho_{000,t}$ is coupled only to seven of the other elements $\rho_{\mu\nu\lambda,t}$. The differential equation is given by

$$\frac{\partial}{\partial t}\xi(t) = (\theta\mathbb{I}+M)\xi(t), \qquad (6.47)$$

where we have defined the quantity

$$\xi(t) = \left(\rho_{000,t},\rho_{022,t},\rho_{300,t},\rho_{320,t},\rho_{302,t},\rho_{020,t},\rho_{322,t},\rho_{002,t}\right)^T. \qquad (6.48)$$

Furthermore, we have defined

$$\theta = 2\pi\nu^2 V\sum_{\alpha=1}^{2}\sum_{i,j=1}^{2}|t_{\alpha0}^{ij}|^2(e^{i\chi_\alpha}-1). \qquad (6.49)$$

Furthermore, we obtain $M/2 =$

$$\begin{pmatrix}
0 & c_{1,-} & c_{2,-} & -b_{1,-}-b_{2,-} & a_{1,-} & a_{2,-} & 0 & 0 \\
-c_{1,+} & -d_1 & 0 & -a_{1,+} & b_{1,+}-b_{2,-} & 0 & c_{2,-} & a_{2,-} \\
-c_{2,+} & 0 & -d_2 & -a_{2,+} & 0 & -b_{1,-}+b_{2,+} & c_{1,-} & a_{1,-} \\
b_{1,+}+b_{2,+} & -a_{1,+} & -a_{2,+} & -d_1-d_2 & -c_{1,+} & -c_{2,+} & 0 & 0 \\
a_{1,-} & -b_{1,-}+b_{2,+} & 0 & c_{1,-} & -d_2 & 0 & -a_{2,+} & -c_{2,+} \\
a_{2,-} & 0 & b_{1,+}-b_{2,-} & c_{2,-} & 0 & -d_1 & -a_{1,+} & -c_{1,+} \\
0 & -c_{2,+} & -c_{1,+} & 0 & -a_{2,+} & -a_{1,+} & -d_1-d_2 & b_{1,+}+b_{2,+} \\
0 & a_{2,-} & a_{1,-} & 0 & c_{2,-} & c_{1,-} & -b_{1,-}-b_{1,-} & 0
\end{pmatrix} \tag{6.50}$$

for the matrix defined in Eq. (6.47). Here, we have defined the following two quantities for $\alpha = 1, 2$

$$a_{\alpha,\pm} = 2\pi\nu^2 V \mathrm{Re}\left(t^{11}_{1,\alpha 0}(t^{22}_{1,\alpha 0})^* - t^{21}_{1,\alpha 0}(t^{12}_{1,\alpha 0})^*\right)(e^{i\chi_\alpha} \pm 1), \tag{6.51}$$

$$b_{\alpha,\pm} = 2\pi\nu^2 V \sum_{j=1}^{2} \mathrm{Im}(t^{j1}_{1,\alpha 0}(t^{j2}_{1,\alpha 0})^*)(e^{i\chi_\alpha} \pm 1). \tag{6.52}$$

Furthermore, we have defined

$$c_{\alpha,\pm} = 2\pi\nu^2 V \sum_{j=1}^{2} \mathrm{Im}(t^{1j}_{1,\alpha 0}(t^{2j}_{1,\alpha 0})^*)(e^{i\chi_\alpha} \pm 1), \tag{6.53}$$

$$d_\alpha = 2\pi\nu^2 V \sum_{i,j=1}^{2} |t^{ij}_{1,\alpha 0}|^2 e^{i\chi_\alpha}. \tag{6.54}$$

Taking derivatives of the resulting generating function $\mathrm{Tr}_q\left(\rho_\tau(\chi_1, \chi_2)\right)$ generically yields a Fano factor of order one as claimed in the main text.

In the special case $N_0 = 2$ and $N_{1,2} = 1$ discussed in the main text, we find that the Bloch Redfield equation couples the element $\rho_{000,t}$ only to $\rho_{320,t}$. Concretely, this is expressed by the relation $\partial_t \tilde{\xi}(t) = (\tilde{\theta}\mathbb{I} + \tilde{M})\tilde{\xi}(t)$, where we have defined $\tilde{\xi}(t) = \left(\rho_{000,t}, \rho_{320,t}\right)^T$ and the matrix $\tilde{\theta}\mathbb{I} + \tilde{M}$ is stated in the main text in Eqs. (4.95) and (4.96). The eigenvalue of $\tilde{\theta}\mathbb{I} + \tilde{M}$ which vanishes at zero counting parameters yields the cumulant generating function. In the case $N_0 = 1$ and $N_{1,2} = 2$ discussed in the main text, we find $\partial_t \xi'(t) = (\theta' I + M')\xi'(t)$, where we have defined the quantity $\xi'(t) = \left(\rho_{000,t}, \rho_{022,t}, \rho_{300,t}, \rho_{322,t}\right)^T$. The matrix $\theta'\mathbb{I} + M'$ is the one stated in Eqs. (4.101) and (4.102) in the main text and its eigenvalue vanishing at zero counting parameters once again yields the cumulant generating function.

Appendix F: Further new approaches to MBS detection

In this part of the appendix, we provide details on derivations supplementing Chapter 5. First, we derive the effective tunnel Hamiltonians stated in Eqs. (5.2) and (5.4) for the device shown in Fig. 5.1 in Section 5.1. We start from the microscopic tunneling Hamiltonian

$$\begin{aligned} H_{\mathrm{T}} &= \sum_{j=1}^{N_{\mathrm{L}}}\sum_{k}\left[\lambda_0^j c_{0,k}^\dagger \gamma_{\mathrm{L}}^j e^{-i\phi/2} + \mathrm{H.c.}\right] \\ &\quad + \sum_{j=1}^{N_{\mathrm{R}}}\sum_{k}\left[(\lambda_1^j c_{1,k}^\dagger + \lambda_2^j c_{2,k}^\dagger)\gamma_{\mathrm{R}}^j e^{-i\phi/2} + \mathrm{H.c.}\right] \end{aligned} \tag{6.55}$$

to derive the effective Hamiltonian along the lines of Appendix B. We again assume the integer N_0 in units of the elementary charge to be the equilibrium charge. The tunable backgate parameter is given by $n_g = N_0 + \Delta n_g$ with a small detuning, $\Delta n_g \ll 1$. Furthermore, we again define $E_\pm = E_C(N_0 \pm 1 - \Delta n_g)^2 - E_C(N_0 - \Delta n_g)^2$. Compared to the derivation of Appendix B, a qualitatively different term arises due to the fact that a single wire end is being coupled to two different leads. The new type of term is denoted η^j (see below) and describes processes where an electron tunneling from lead 2 into γ_{R}^i is accompanied by an electron tunneling out of γ_{R}^i into lead 1. For the effective tunneling Hamiltonian we obtain

$$\begin{aligned} H_{\mathrm{eff}} &= P_0 H_{\mathrm{T}} P_0 + P_0 H_{\mathrm{T}}\left(\frac{1}{-H_C}H_{\mathrm{T}}\right)P_0 + \dots \\ &= \sum_{k,k'}\left[\left(\eta^1 + \eta^2 + t_{12}^{12}(i\gamma_{\mathrm{R}}^1\gamma_{\mathrm{R}}^2)\right)c_{1,k}^\dagger c_{2,k'} + \mathrm{H.c.}\right] \\ &\quad + \sum_{\alpha=1}^{2}\sum_{j=1}^{N_{\mathrm{L}}}\sum_{j'=1}^{N_{\mathrm{R}}}\sum_{k,k'}\left[t_{\alpha 0}^{jj'}(i\gamma_{\mathrm{R}}^j\gamma_{\mathrm{L}}^{j'})c_{\alpha,k}^\dagger c_{0,k'} + \mathrm{H.c.}\right] + \dots \end{aligned} \tag{6.56}$$

with

$$\begin{aligned}\eta^j &= \lambda_1^j(\lambda_2^j)^* \frac{E_- - E_+}{E_+ E_-} \\ &= -\frac{\lambda_1^j(\lambda_2^j)^*}{E_C}\frac{4\Delta n_g}{1-4\Delta n_g} \\ &\simeq -\frac{4\Delta n_g \lambda_1^j(\lambda_2^j)^*}{E_C} \end{aligned} \tag{6.57}$$

and $t_{\alpha\alpha'}^{ij} \simeq 2i\lambda_\alpha^i(\lambda_{\alpha'}^j)^*/E_C$. Thus, we arrive at the effective tunneling Hamiltonians (5.2) and (5.4).

We now go on to derive the counting statistics. The equation governing the time evolution of the reduced generalized density matrix $\rho_t(\chi_1,\chi_2)$ in the Hilbert space corresponding to the Majorana operators $\gamma_{L/R}^j$ has been stated in the main text in Eq. (5.5). In the case of the genuine topological Majorana wire, we have $N_{\mathrm{L/R}} = 1$ and the evolution equation takes on the form

$$\begin{aligned}\frac{\partial}{\partial t}\rho_t &= 2\pi\nu^2 V \sum_{\alpha=1}^{2} \left|t_{\alpha 0}^{11}\right|^2 \left[e^{i\chi_\alpha}(i\gamma_{\mathrm{R}}^1\gamma_{\mathrm{L}}^1)\rho_t(i\gamma_{\mathrm{R}}^1\gamma_{\mathrm{L}}^1) - \rho_t\right] \\ &\quad +4\pi\nu^2 T\left|\eta^1\right|^2 \left(\cos\left(\chi_1-\chi_2\right)-1\right)\rho_t. \end{aligned} \tag{6.58}$$

The corresponding cumulant generating function reads

$$\begin{aligned}\tau^{-1}\ln \mathrm{Tr}_q \rho_\tau(\chi_1,\chi_2) &= 2\pi\nu^2 V \sum_{\alpha=1}^{2} |t_{\alpha 0}^{11}|^2 (e^{i\chi_\alpha}-1) \\ &\quad +4\pi\nu^2 T\left|\eta^1\right|^2\left(\cos\left(\chi_1-\chi_2\right)-1\right) \end{aligned} \tag{6.59}$$

and results in Eq. (5.10) as well as the Fano factor $|F| = \mathcal{O}\left(\Delta n_g \frac{T}{V}\right)$.

Now, we turn to Andreev bound states in which case there are generically strong cross-correlations with the Fano factor $|F| = \mathcal{O}(1)$. To demonstrate this, we consider $N_{\mathrm{R}} = 2$, $N_{\mathrm{L}} = 1$, as discussed in the main text. Then, the zero temperature evolution equation takes on the form

$$\begin{aligned}\frac{\partial}{\partial t}\rho_t \;=\;& -i[H_q,\rho_t] + 2\pi\nu^2 V\left(\sum_{\alpha=1}^{2}\sum_{j=1}^{2}|t^{j1}_{\alpha0}|^2\left[e^{i\chi_\alpha}(i\gamma^j_{\mathrm{R}}\gamma^1_{\mathrm{L}})\rho_t(i\gamma^j_{\mathrm{R}}\gamma^1_{\mathrm{L}})-\rho_t\right]\right.\\ &+\sum_{\alpha=1}^{2}e^{i\chi_\alpha}[t^{11}_{\alpha0}(t^{21}_{\alpha0})^*(i\gamma^1_{\mathrm{R}}\gamma^1_{\mathrm{L}})\rho_t(i\gamma^2_{\mathrm{R}}\gamma^1_{\mathrm{L}})+(t^{11}_{\alpha0})^*t^{21}_{\alpha0}(i\gamma^2_{\mathrm{R}}\gamma^1_{\mathrm{L}})\rho_t(i\gamma^1_{\mathrm{R}}\gamma^1_{\mathrm{L}})]\\ &\left.+\sum_{\alpha=1}^{2}\mathrm{Im}(t^{11}_{\alpha0}(t^{21}_{\alpha0})^*)\{i\gamma^1_{\mathrm{R}}\gamma^2_{\mathrm{R}},\rho_t\}\right). \qquad (6.60)\end{aligned}$$

The unitary part of the dynamics is generated by an effective Hamiltonian $H_q \sim i\gamma^1_{\mathrm{R}}\gamma^2_{\mathrm{R}}$. We represent the Majorana bilinears using the Pauli matrices, $\sigma_1 = i\gamma^1_{\mathrm{R}}\gamma^1_{\mathrm{L}}$, $\sigma_2 = i\gamma^2_{\mathrm{R}}\gamma^1_{\mathrm{L}}$ and $\sigma_3 = i\gamma^2_{\mathrm{R}}\gamma^1_{\mathrm{R}}$, and parametrize the density matrix via $\rho_t = \sum_{\mu=0}^{3}\rho_{\mu,t}\sigma_\mu$. Here, the element $\rho_{0,t}$, which determines the trace, is coupled only to $\rho_{3,t}$ according to

$$\frac{\partial}{\partial t}\widehat{\xi}(t) = \left(\widehat{\theta}\,\mathbb{I} + \widehat{M}\right)\widehat{\xi}(t) \qquad (6.61)$$

with $\widehat{\xi}(t) = (\rho_{0,t},\rho_{3,t})^T$. The matrix $\widehat{M}$ is given by

$$\widehat{M} = 4\pi\nu^2 V\sum_{\alpha=1}^{2}\begin{pmatrix} 0 & (e^{i\chi_\alpha}-1)\,\mathrm{Im}(t^{11}_{\alpha0}(t^{21}_{\alpha0})^*) \\ -\left(e^{i\chi_\alpha}+1\right)\mathrm{Im}(t^{11}_{\alpha0}(t^{21}_{\alpha0})^*) & -e^{i\chi_\alpha}\sum_{j=1}^{2}|t^{j1}_{\alpha0}|^2\end{pmatrix} \qquad (6.62)$$

and we have defined $\widehat{\theta} = 2\pi\nu^2 V\sum_{\alpha=1}^{2}\sum_{j=1}^{2}|t^{j1}_{\alpha0}|^2(e^{i\chi_\alpha}-1)$. We can find the generating function, $\mathcal{Z} \equiv \ln\mathrm{Tr}_q\left(\rho_\tau(\boldsymbol{\chi})\right)$, by solving the linear system of differential equations defined by (6.61). The resulting cumulant generating function in the long time limit is given by

$$\begin{aligned}\tau^{-1}\ln\mathrm{Tr}_q\left(\rho_\tau(\boldsymbol{\chi})\right) \;=\;& 2\pi\nu^2 V\left(-\sum_{\alpha=1}^{2}\sum_{j=1}^{2}|t^{j1}_{\alpha0}|^2\right.\\ &\left.+\sqrt{\left(\sum_{\alpha=1}^{2}\sum_{j=1}^{2}e^{i\chi_\alpha}|t^{j1}_{\alpha0}|^2\right)^2 - 4\prod_{\pm}\left[\sum_{\alpha=1}^{2}\left(e^{i\chi_\alpha}\pm 1\right)\eta_\alpha\right]}\right) \qquad (6.63)\end{aligned}$$

where we have defined the interference parameter $\eta_\alpha = \mathrm{Im}(t^{11}_{\alpha0}(t^{21}_{\alpha0})^*)$. By performing derivatives with respect to the counting parameters, we arrive at the cross-correlation formula (5.12).

Finally, we provide details on the derivation of the number of possible stationary current values for $N_0 = 2$, $N_1 = 1$ for general parameters $t_{\alpha\alpha'}^{jj'}$. To this end, we set $t_{20}^{j1} = \chi_2 = 0$ in Eq. (6.63). Calculating the stationary current $\langle I_1 \rangle = -i\tau^{-1}\,\partial_{\chi_1} \ln \mathrm{Tr}_q\left(\rho_\tau\right)\big|_{\boldsymbol{\chi}=(0,0)}$, shows that in the absence of an interference link there is a single current outcome as claimed in Section 5.2. The same statement can be shown analogously for $N_0 = 2$, $N_1 = 1$. When a reference arm is present, $t_0 \neq 0$, there are two distinct current outcomes.

Bibliography

[1] P. A. M. Dirac, "The Quantum Theory of the Electron", Proc. Roy. Soc. A**117**: 610-624 (1928).

[2] E. Majorana, L. Maiani, “A symmetric theory of electrons and positrons”, In: Bassani G.F., Council of the Italian Physical Society (eds) Ettore Majorana Scientific Papers. Springer, Berlin, Heidelberg (2006).

[3] S. R. Elliott and M. Franz, “Colloquium: Majorana fermions in nuclear, particle, and solid-state physics”, Rev. Mod. Phys. **87**, 137 (2015).

[4] J. Alicea, “New directions in the pursuit of Majorana fermions in solid state systems”, Rep. Prog. Phys. **75** 076501 (2012).

[5] M. Sato and Y. Ando, “Topological superconductors: a review”, Rep. Prog. Phys. **80**, 076501 (2017).

[6] A. Yu. Kitaev, “Unpaired Majorana fermions in quantum wires”, Usp. Fiz. Nauk (Suppl) **171**, 131 (2001).

[7] L. Fu and C. L. Kane, “Superconducting Proximity Effect and Majorana Fermions at the Surface of a Topological Insulator”, Phys. Rev. Lett. **100**, 096407 (2008).

[8] Y. Oreg, G. Refael, and F. von Oppen, “Helical Liquids and Majorana Bound States in Quantum Wires”, Phys. Rev. Lett. **105**, 177002 (2010).

[9] R. M. Lutchyn, J. D. Sau, and S. Das Sarma, “Majorana Fermions and a Topological Phase Transition in Semiconductor-Superconductor Heterostructures”, Phys. Rev. Lett. **105**, 077001 (2010).

[10] C. Nayak, S. H. Simon, A. Stern, M. Freedman, and S. Das Sarma, “Non-Abelian anyons and topological quantum computation”, Rev. Mod. Phys. **80**, 1083 (2008).

[11] S. Plugge, A. Rasmussen, R. Egger and K. Flensberg, “Majorana box qubit”, New J. Phys **12**, 012002 (2017).

[12] T. Karzig et. al., “Scalable designs for quasiparticle-poisoning-protected topological quantum computation with Majorana zero modes”, Phys. Rev. B **95**, 235305 (2017).

[13] A. Cook and M. Franz, “Majorana Fermions in Proximity-coupled Topological Insulator Nanowires”, Phys. Rev. B **84**, 201105(R) (2011).

[14] A. M. Cook, M. M. Vazifeh, and M. Franz, “Stability of Majorana Fermions in Proximity-Coupled Topological Insulator Nanowires”, Phys. Rev. B **86**, 155431 (2012).

[15] R. M. Lutchyn et. al., ”Majorana zero modes in superconductor–semiconductor heterostructures”, Nature Reviews Materials **3**, 52–68 (2018).

[16] X.-L. Qi and S.-C. Zhang, “Topological insulators and superconductors”, Rev. Mod. Phys. **83**, 1057 (2011).

[17] M. Z. Hasan and C. L. Kane, “Colloquium: Topological insulators”, Rev. Mod. Phys. **82**, 3045 (2010).

[18] C. W. J. Beenakker, “Search for Majorana fermions in superconductors”, Annu. Rev. Con. Mat. Phys. **4**, 113 (2013).

[19] M. Leijnse and K. Flensberg, “Introduction to topological superconductivity and Majorana fermions”, Semicond. Sci. Technol. **27**, 124003 (2012).

[20] R. Aguado, “Majorana quasiparticles in condensed matter”, Riv. Nuovo Cim, **40**, 523 (2017).

[21] S. Ryu, A. P. Schnyder, A. Furusaki, and A. W. W. Ludwig, “Topological insulators and superconductors: tenfold way and dimensional hierarchy”, New J. Phys **12**, 065010 (2010).

[22] A. Altland and M. R. Zirnbauer, “Nonstandard symmetry classes in mesoscopic normal-superconducting hybrid structures”, Phys. Rev. B **55**, 1142 (1997).

[23] A. Kitaev, “Periodic table for topological insulators and superconductors”, AIP Conf. Proc. **1134**, 22–30 (2009).

[24] A. Altland and B. D. Simons, “Condensed Matter Field Theory”, Cambridge University Press, second edition (2010).

[25] B. Béri and N. R. Cooper, “Topological Kondo Effect with Majorana Fermions”, Phys. Rev. Lett. **109**, 156803 (2012).

[26] A. Altland, B. Béri, R. Egger, and A. M. Tsvelik, “Multichannel Kondo Impurity Dynamics in a Majorana Device”, Phys. Rev. Lett. **113**, 076401 (2014).

[27] Y. V. Nazarov and Y. M. Blanter, “Quantum transport”, Cambridge University Press (2009).

[28] B. Béri, “Majorana-Klein Hybridization in Topological Superconductor Junctions”, Phys. Rev. Lett. **110**, 216803 (2013).

[29] L. Fu, “Electron Teleportation via Majorana Bound States in a Mesoscopic Superconductor”, Phys. Rev. Lett. **104**, 056402 (2010).

[30] S. Vijay and L. Fu, “Teleportation-based quantum information processing with Majorana zero modes”, Phys. Rev. B **94**, 235446 (2016).

[31] S. M. Albrecht, E. B. Hansen, A. P. Higginbotham, F. Kuemmeth, T. S. Jespersen, J. Nygård, P. Krogstrup, J. Danon, K. Flensberg, and C. M. Marcus, “Transport Signatures of Quasiparticle Poisoning in a Majorana Island”, Phys. Rev. Lett. **118**, 137701 (2017).

[32] D. Pekker, C.-Y. Hou, V. E. Manucharyan, and E. Demler, "Proposal for Coherent Coupling of Majorana Zero Modes and Superconducting Qubits Using the 4π Josephson Effect”, Phys. Rev. Lett. **111**, 107007 (2013).

[33] D. V. Averin and Yu. V. Nazarov, “Virtual electron diffusion during quantum tunneling of the electric charge”, Phys. Rev. Lett. **65**, 2446 (1990).

[34] A. M. Whiticar, A. Fornieri, E. C. T. O’Farrell, A. C. C. Drachmann, T. Wang, C. Thomas, S. Gronin, R. Kalla-her, G. C. Gardner, M. J. Manfra, C. M. Marcus, and F. Nichele, “Interferometry and coherent single-electron transport through hybrid superconductor-semiconductor Coulomb islands”, arXiv:1902.07085 (2019).

[35] D. A. Ivanov, “Non-Abelian Statistics of Half-Quantum Vortices in p-Wave Superconductors”, Phys. Rev. Lett. **86**, 268 (2001).

[36] C. W. J. Beenakker, “Search for non-Abelian Majorana braiding statistics in superconductors”, arXiv:1907.06497.

[37] J. Alicea, Y. Oreg, G. Refael, F. von Oppen, and M. P. A. Fisher , “Non-Abelian statistics and topological quantum information processing in 1D wire networks”, Nature Physics volume **7**, pages 412–417 (2011).

[38] F. Hassler, “Majorana Qubits”, In "Quantum Information Processing. Lecture Notes of the 44th IFF Spring School 2013", edited by D. P. DiVincenzo, Verlag des Forschungszentrums Jülich (2013).

[39] D. Aasen, M. Hell, R. V. Mishmash, A. Higginbotham, J. Danon, M. Leijnse, T. S. Jespersen, J. A. Folk, C. M. Marcus, K. Flensberg, and J. Alicea, “Milestones Toward Majorana-Based Quantum Computing”, Phys. Rev. X **6**, 031016 (2016).

[40] T. D. Stanescu, “Introduction to Topological Quantum Matter & Quantum Computation,” CRC Press, Taylor & Francis Group (2016).

[41] S. Das Sarma, M. Freedman, C. Nayak, “Majorana Zero Modes and Topological Quantum Computation”, npj Quantum Information **1**, 15001 (2015).

[42] C. Knapp, M. Zaletel, D. E. Liu, M. Cheng, P. Bonderson, and C. Nayak, “The nature and correction of adiabatic errors in anyon braiding”, Phys. Rev. X **6**, 041003 (2016).

[43] K. T. Law, P. A. Lee, and T. K. Ng, “Majorana fermion induced resonant Andreev reflection”, Phys. Rev. Lett. **103**, 237001 (2009).

[44] V. Mourik, K. Zuo, S. M. Frolov, S. R. Plissard, E. P. A.Bakkers, and L. P. Kouwenhoven, “Signatures of Majorana Fermions in Hybrid Superconductor-Semiconductor Nanowire Devices”, Science **336**, Issue 6084, pp. 1003-1007 (2012).

[45] F. Nichele, A. C. C. Drachmann, A. M. Whiticar, E. C.T. O’Farrell, H. J. Suominen, A. Fornieri, T. Wang, G. C.Gardner, C. Thomas, A. T. Hatke, P. Krogstrup, M. J. Manfra, K. Flensberg, and C. M. Marcus, “Scaling of Majorana Zero-Bias Conductance Peaks”, Phys. Rev. Lett. **119**, 136803 (2017).

[46] H. Zhang, C. X. Liu, S. Gazibegovic, D. Xu, J. A. Lo-gan, G. Wang, N. van Loo, J. D. S. Bommer, M. W. A. deMoor, D. Car, R. L. M. Op het Veld, P. J. van Veldhoven, S. Koelling, M. A. Verheijen, M. Pendharkar, D. J. Penna-chio, B. Shojaei, J. S. Lee, C. J. Palmstrom, E. P. A. M.Bakkers, S. Das Sarma, and L. P. Kouwenhoven, "Quantized Majorana conductance", Nature **556**, 74 (2018).

[47] D. Bagrets and A. Altland, "Class D Spectral Peak in Majorana Quantum Wires", Phys. Rev. Lett. **109**, 227005 (2012).

[48] J. Liu, A. C. Potter, K. T. Law, and P. A. Lee, "Zero-Bias Peaks in the Tunneling Conductance of Spin-Orbit-Coupled Superconducting Wires with and without Majorana End-States", Phys. Rev. Lett. **109**, 267002 (2012).

[49] C.-X. Liu, J. D. Sau, Tudor D. Stanescu, and S. Das Sarma, "Andreev bound states versus Majorana bound states in quantum dot-nanowire-superconductor hybrid structures: Trivial versus topological zero-bias conductance peaks", Phys. Rev. B **96**, 075161 (2017).

[50] C. Moore, T. D. Stanescu, and S. Tewari, "Two-terminal charge tunneling: Disentangling Majorana zero modes from partially separated Andreev bound states in semiconductor-superconductor heterostructures", Phys. Rev. B **97**, 165302 (2018).

[51] Y.-H. Lai, J. D. Sau, and S. Das Sarma, "Presence versus absence of end-to-end nonlocal conductance correlations in Majorana nanowires: Majorana bound states versus Andreev bound states", Phys. Rev. B **100**, 045302 (2019).

[52] A. Vuik, B. Nijholt, A.R. Akhmerov, M. Wimmer, "Reproducing topological properties with quasi-Majorana states ", SciPost Phys. **7**, 061 (2019).

[53] S. M. Albrecht, A. P. Higginbotham, M. Madsen, F. Kuemmeth, T. S. Jespersen, J. Nygård, P. Krogstrup, and C. M. Marcus, "Exponential protection of zero modes in Majorana islands", Nature volume **531**, 206-209 (2016).

[54] R. Egger, Unpublished notes.

[55] A. Zazunov, A. Altland, and R. Egger, "Transport properties of the Coulomb–Majorana junction", New J. Phys. **16**, 015010 (2014).

[56] M. Gau, S. Plugge and R. Egger, “Quantum transport in coupled Majorana box systems”, PRB **97**, 184506 (2018).

[57] T. Jonckheere, J. Rech, A. Zazunov, R. Egger, A. Levy Yeyati, and T. Martin, “Giant Shot Noise from Majorana Zero Modes in Topological Trijunctions”, Phys. Rev. Lett. **122**, 097003 (2019).

[58] M. Hell, K. Flensberg and M. Leijnse, “Distinguishing Majorana bound states from localized Andreev bound states by interferometry”, Phys. Rev. B **97**, 161401(R) (2018).

[59] S. Rubbert and A. R. Akhmerov, “Detecting Majorana nonlocality using strongly coupled Majorana bound states”, Phys. Rev. B **94**, 115430 (2016).

[60] C. Schrade and L. Fu, “Andreev or Majorana, Cooper finds out”, arXiv:1809.06370 (2018).

[61] R. Tuovinen, E. Perfetto, R. van Leeuwen, G. Stefanucci, and M. A. Sentef, “Distinguishing Majorana zero modes from impurity states through time-resolved transport”, New J. Phys. **21** 103038 (2019).

[62] S. Smirnov, “Universal Majorana thermoelectric noise”, Phys. Rev. B **97**, 165434 (2018).

[63] K. Yavilberg, E. Ginossar and E. Grosfeld, “Differentiating Majorana from Andreev Bound States in a Superconducting Circuit”, Phys. Rev. B **100**, 241408(R) (2019).

[64] J. Manousakis, A. Altland, D. Bagrets, R. Egger, and Y. Ando, “Majorana qubits in a topological insulator nanoribbon architecture”, Phys. Rev. B **95**, 165424 (2017).

[65] P. M. Ostrovsky, I. V. Gornyi, and A. D. Mirlin, “Interaction-Induced Criticality in $\mathbb{Z}_2$ Topological Insulators”, Phys. Rev. Lett. **105**, 036803 (2010).

[66] Y. Zhang and A. Vishwanath, “Anomalous Aharonov-Bohm Conductance Oscillations from Topological Insulator Surface States”, Phys. Rev. Lett. **105**, 206601 (2010).

[67] J. H. Bardarson and P. W. Brouwer, and J. E. Moore, "Aharonov-Bohm Oscillations in Disordered Topological Insulator Nanowires", Phys. Rev. Lett. **105**, 156803 (2010).

[68] R. Egger, A. Zazunov, and A. L. Yeyati, "Helical Luttinger Liquid in Topological Insulator Nanowires", Phys. Rev. Lett. **105**, 136403 (2010).

[69] A. Kundu, A. Zazunov, A. L. Yeyati, T. Martin, and R. Egger, "Energy spectrum and broken spin-surface locking in topological insulator quantum dots," Phys. Rev. B **83**, 125429 (2011).

[70] J. H. Bardarson and J. E. Moore, "Quantum interference and Aharonov–Bohm oscillations in topological insulators", Rep. Prog. Phys. **76**, 056501 (2013).

[71] H. B. Nielsen and M. Ninomiya, "The Adler-Bell-Jackiw anomaly and Weyl fermions in a crystal", Physics Letters B, Volume **130**, Issue 6, p. 389-396.

[72] S. Cho, B. Dellabetta, R. Zhong, J. Schneeloch, T. Liu, G. Gu, M. J. Gilbert, and N. Mason, "Aharonov–Bohm oscillations in a quasi-ballistic three-dimensional topological insulator nanowire", Nature Comm. **6**, 7634 (2015).

[73] L. A. Jauregui, M.T. Pettes, L. P. Rokhinson, L. Shi, and Y. P. Chen, "Magnetic field-induced helical mode and topological transitions in a topological insulator nanoribbon", Nature Nanotech. **11**, 345 (2016).

[74] V. A. Volkov and V. V. Enaldiev, "Surface states of a system of dirac fermions: A minimal model", JETP **149** 702-716 (2016).

[75] J. H. Bardarson and R. Ilan, "Transport in Topological Insulator Nanowires" (2018). In: D. Bercioux, J. Cayssol, M. Vergniory, M. Reyes Calvo (eds) Topological Matter. Springer Series in Solid-State Sciences, vol **190**. Springer, Cham.

[76] F. de Juan, J. H. Bardarson, and R. Ilan, "Conditions for fully gapped topological superconductivity in topological insulator nanowires", SciPost Phys. **6**, 060 (2019).

[77] P. Sitthison and T. D. Stanescu, "Robustness of topological superconductivity in proximity-coupled topological insulator nanoribbons", Phys. Rev. B **90**, 035313 (2014).

[78] F. de Juan, R. Ilan, and J. H. Bardarson, "Robust Transport Signatures of Topological Superconductivity in Topological Insulator Nanowires", Phys. Rev. Lett. **113**, 107003 (2014).

[79] R. Ilan, J. H. Bardarson, H.-S. Sim, and J. E. Moore, "Detecting perfect transmission in Josephson junctions on the surface of three dimensional topological insulators", New J. Phys. **16**, 053007 (2014).

[80] G.-Y. Huang and H. Q. Xu, "Majorana fermions in topological-insulator nanowires: From single superconducting nanowires to Josephson junctions", Phys. Rev. B **95**, 155420 (2017).

[81] S. Das Sarma, J. D. Sau, and T. D. Stanescu, "Splitting of the zero-bias conductance peak as smoking gun evidence for the existence of the Majorana mode in a superconductor-semiconductor nanowire", Phys. Rev. B **86**, 220506(R) (2012).

[82] H. J. Suominen, M. Kjaergaard, A. R. Hamilton, J. Shabani, C. J. Palmstrøm, C. M. Marcus, and F. Nichele, "Zero-Energy Modes from Coalescing Andreev States in a Two-Dimensional Semiconductor-Superconductor Hybrid Platform", Phys. Rev. Lett. **119**, 176805 (2017).

[83] L. A. Jauregui, M. Kayyalha, A. Kazakov, I. Miotkowski, L. P. Rokhinson, and Y. P. Chen, "Gate-tunable supercurrent and multiple andreev reflections in a superconductor-topological insulator nanoribbon-superconductor hybrid device", Appl. Phys. Lett. **112** (9), 093105 (2018).

[84] M. Kayyalha, M. Kargarian, A. Kazakov, I. Miotkowski, V. M. Galitski, V. M. Yakovenko, L. P. Rokhinson, and Y. P. Chen, "Anomalous low-temperature enhancement of supercurrent in topological-insulator nanoribbon josephson junctions: Evidence for low-energy andreev bound states", Phys. Rev. Lett. **122**, 047003 (2019).

[85] B. M. Terhal, F. Hassler, and D. P. DiVincenzo, "From Majorana fermions to topological order", Phys. Rev. Lett. **108**, 260504 (2012).

[86] S. Vijay, T. H. Hsieh, and L. Fu, "Majorana Fermion Surface Code for Universal Quantum Computation", Phys. Rev. X **5**, 041038 (2015).

[87] L. A. Landau, S. Plugge, E. Sela, A. Altland, S. M. Albrecht, and R. Egger, "Towards Realistic Implementations of a Majorana Surface Code", Phys. Rev. Lett. **116**, 050501 (2016).

[88] S. Plugge, L. A. Landau, E. Sela, A. Altland, K. Flensberg, and R. Egger, "Roadmap to Majorana surface codes", Phys. Rev. B **94**, 174514 (2016).

[89] J. Manousakis, C. Wille, A. Altland, R. Egger, K. Flensberg, and F. Hassler, "Weak measurement protocols for Majorana bound state identification", Phys. Rev. Lett. **124**, 096801 (2020).

[90] A. N. Jordan and M. Büttiker, "Continuous Quantum Measurement with Independent Detector Cross Correlations", Phys. Rev. Lett. **95**, 220401 (2005).

[91] A. A. Clerk, M. H. Devoret, S. M. Girvin, Florian Marquardt, and R. J. Schoelkopf, "Introduction to quantum noise, measurement, and amplification", Rev. Mod. Phys. **82**, 1155 (2010).

[92] K. Jacobs and D. A. Steck, "A straightforward introduction to continuous quantum measurement", Contemporary Physics, **47**:5, 279-303, (2007).

[93] H. M. Wiseman and G. J. Milburn, "Quantum Measurement and Control", Cambridge University Press (2010).

[94] H. Wei and Y. V. Nazarov, "Statistics of measurement of noncommuting quantum variables: Monitoring and purification of a qubit", Phys. Rev. B **78**, 045308 (2008).

[95] R. Ruskov, A. N. Korotkov, and K. Mølmer, "Qubit State Monitoring by Measurement of Three Complementary Observables", Phys. Rev. Lett. **105**, 100506 (2010).

[96] A. Kitaev, "Anyons in an exactly solved model and beyond", Ann. Phys. **321**, 2 (2006).

[97] W. Belzig, "Full Counting Statistics in Quantum Contacts", arXiv:cond-mat/0312180 (2003).

[98] T. Brandes, “Quantensysteme im Nichtgleichgewicht: Einführung”, Vorlesungsskript TU Berlin, WS 2016/2017, viewed 24th of March 2020, <http://www1.itp.tu-berlin.de/brandes/NG2016.pdf >

[99] M. Kindermann, Yu. V. Nazarov, “Full counting statistics in electric circuits”, In: Yu. V. Nazarov (eds) Quantum Noise in Mesoscopic Physics. NATO Science Series (Series II: Mathematics, Physics and Chemistry), vol 97. Springer, Dordrecht (2003).

[100] H.-P. Breuer and F. Petruccione, “The Theory of Open Quantum Systems”, Oxford University Press (2002).

[101] H. Bruus and K. Flensberg, “Many Body Quantum Theory in Condensed Matter Physics: An Introduction”, Oxford University Press (2004).

[102] A. Franquet and Y. V. Nazarov, “Probability distributions of continuous measurement results for two non-commuting variables and conditioned quantum evolution”, Phys. Rev. A **100**, 062109 (2019).

[103] A. Franquet, Y. V. Nazarov, H. Wei, “Statistics of continuous weak quantum measurement of an arbitrary quantum system with multiple detectors”, arXiv:1804.07639 (2018).

[104] T. Martin and R. Landauer, “Wave-packet approach to noise in multichannel mesoscopic systems”, Phys. Rev. B **45**, 1742 (1992).

Acknowledgements

Now the time has come to thank everyone who supported me during my doctoral studies at the University of Cologne. First and foremost I wish to articulate my deepest gratitude to my supervisor Alexander Altland. Being a part of his research group was a truly great experience which taught me a lot. I would also like to pay my special regards to the Collaborative Research Center 183 “Entangled states of matter” and the Bonn-Cologne Graduate School of Physics and Astronomy (BCGS), both of which supported me in many ways.

I gratefully acknowledge the opportunity of an eight months research stay at the center for quantum devices of the Niels Bohr institute at the University of Copenhagen, which was enabled and supported by the Collaborative Research Center 183 “Entangled states of matter”. I wish to express my great thankfulness to Karsten Flensberg. During my time in Copenhagen he was an amazing host and I enjoyed the collaboration with him very much.

I am very indebted to Dmitry Bagrets, who has a vast knowledge and understanding of theoretical physics, and from whom I have learned a lot. Furthermore I want to thank my other collaborators Reinhold Egger, Carolin Wille, Fabian Hassler and Yoichi Ando. Last but not least I wish to thank my family, my girlfriend and friends for their amazing support.

Erklärung

Ich versichere, dass ich die von mir vorgelegte Dissertation selbständig angefertigt, die benutzten Quellen und Hilfsmittel vollständig angegeben und die Stellen der Arbeit – einschließlich Tabellen, Karten und Abbildungen –, die anderen Werken im Wortlaut oder dem Sinn nach entnommen sind, in jedem Einzelfall als Entlehnung kenntlich gemacht habe; dass diese Dissertation noch keiner anderen Fakultät oder Universität zur Prüfung vorgelegen hat; dass sie – abgesehen von unten angegebenen Teilpublikationen – noch nicht veröffentlicht worden ist, sowie, dass ich eine solche Veröffentlichung vor Abschluss des Promotionsverfahrens nicht vornehmen werde. Die Bestimmungen der Promotionsordnung sind mir bekannt. Die von mir vorgelegte Dissertation ist von Prof. Dr. Alexander Altland betreut worden.

Datum, Ort

Unterschrift

Teilpublikationen:

- J. Manousakis, A. Altland, D. Bagrets, R. Egger, and Y. Ando, “Majorana qubits in a topological insulator nanoribbon architecture”, Phys. Rev. B **95**, 165424 (2017).
- J. Manousakis, C. Wille, A. Altland, R. Egger, K. Flensberg, and F. Hassler, “Weak measurement protocols for Majorana bound state identification”, Phys. Rev. Lett. **124**, 096801 (2020), [Selected as editors’ suggestion and featured as a viewpoint in Physics].